Atomistic Simulations of Synthetic Antiferromagnetic MRAM

Lucy Elliot

Master of Science by Research

University of York
School of Physics, Engineering and Technology
December 2025

Abstract

Increasing demand for high quality, low power, and non-volatile memory in modern computing has positioned Spin-Transfer Torque Magnetic Random Access Memory (STT MRAM) as a promising replacement for conventional RAM in the future. STT-MRAM is composed of two ferromagnetic layers separated by a non-magnetic spacer layer that acts as a Magnetic Tunnel Junction (MTJ). This MRAM faces scalability limitations with high-density configurations suffering from magnetic "cross talk" where the stray magnetic fields from one MRAM cell influence magnetic moments in a nearby MRAM cell. Replacing the typical ferromagnetic free layer with a synthetic antiferromagnetic SAF free layer coupled through the Ruderman–Kittel–Kasuya–Yosida (RKKY) interaction. This mitigates cross talk through dipole field cancellation and accelerates switching.

This thesis investigates the SAF MRAM performance using the atomistic simulation package VAMPIRE which allows the investigation of interfacial effects such as the RKKY exchange and non-uniform thermal nucleation in nanoscale MRAM discs. The simulations conducted in this thesis establish a parameter space for the minimum requirements for reliable operation. These requirements are found by employing a parameter sweep with the Minimal Working Example (MWE), a $1 \times 1 \times 6$ nm cell, on RKKY exchange strength, critical switching field, and the polarisation that reaches the second free layer. Different physical parameters such as anisotropy, and thermal stability are also investigated to evaluate the theoretical functionality of the SAF MRAM as an effective device. When scaling to 40 nm-diameter discs the switching moves from coherent rotation to a non-uniform nucleation-driven process, as seen for standard STT-MRAM.

In conclusion, this thesis provides the necessary atomistic framework and parameter regimes for engineering high-quality, low-power, and non-volatile STT-SAF MRAM, and demonstrates the need for non-continuum modelling methods for accurate device simulation.

Acknowledgements

Thank you to my supervisors Dr. Richard Evans and Prof. Roy Chantrell for your incredible insight and guidance throughout my master's programme.

Thank you also to my dad, Phil, who took many opportunities throughout the year to tell me how to structure a sentence "properly".

Lucy Elliot,
York,
2025.

Declaration

I declare that this thesis is a presentation of original work and I am the sole author. This work has not previously been presented for a degree or other qualification at this University or elsewhere. All sources are acknowledged as references. None of contents of this thesis have been submitted for publication.

Contents

Declaration **v**

List of tables **x**

List of figures **xii**

Nomenclature **1**
List of Abbreviations 1

1 Motivation **5**
1.1 Motivation 5
1.2 Magnetic Random Access Memory (MRAM) 7

2 Introduction **9**
2.1 Atomic Origins of Magnetism 9
2.1.1 Magnetic States and Ordering 13
Ferromagnetism 13
Antiferromagnetism 15
2.2 Ruderman–Kittel–Kasuya–Yosida (RKKY) Interaction 16

3 Introduction to Spintronics **19**
3.1 Spin Transport and Magnetisation Switching 20
3.1.1 Spin Polarisation 20
3.1.2 Spin Accumulation 21

3.1.3 Spin Diffusion . . . 22
3.1.4 Magnetic Tunnel Junction (MTJ) and Tunnel Magnetoresistance (TMR) . . . 27
3.1.5 Spin Transfer Torque . . . 30

4 Atomistic Modelling 35
4.1 Introduction to Spin Models . . . 35
4.2 Heisenberg Hamiltonian . . . 36
Exchange Energy . . . 37
Anisotropic and Tensor Exchange . . . 39
4.2.1 Magnetic Anisotropy . . . 40
Uniaxial Anisotropy . . . 40
Crystal Anisotropy (Cubic) . . . 41
Shape and Interfacial Anisotropy . . . 41
4.2.2 Applied Fields ($\mathscr{H}_{app}$) . . . 42
4.2.3 Dipolar Energy ($\mathscr{H}_{dip}$) . . . 43
Continuum Formulation . . . 43
Atomistic Formulation . . . 43
Computational Note . . . 44
4.3 Monte Carlo Methods . . . 46
Ergodicity and Reversibility . . . 47
4.3.1 Markov Chain Monte Carlo (MCMC) . . . 48
4.3.2 Hinzke and Nowak (HN) Method . . . 49
The Combined Acceptance Scheme . . . 51
Spin Flip Trial Move . . . 51
Gaussian Trial Move . . . 51
Random Trial Move . . . 52
Curie Temperature . . . 53
4.4 Spin Dynamics . . . 53
4.4.1 Stochastic LLG Equation (sLLG) . . . 54
4.4.2 sLLG Equation Midpoint Integration Scheme . . . 56

5 MRAM Stack Characterization 59
5.1 Material Choice . . . 60
5.1.1 CoFeB . . . 61
5.1.2 Ruthenium . . . 62
5.2 CoFeB/MgO/CoFeB MTJ . . . 63
Coherent Tunnelling and TMR . . . 63
Thermal Stability Factor (Δ) . . . 63
5.3 CoFeB/Ru/CoFeB Synthetic Antiferromagnet . . . 65
5.3.1 Ruthenium structure . . . 67

5.3.2 RKKY in CoFeB/Ru/CoFeB . . . 68
5.4 Generation in code . . . 69
5.4.1 Parameter Mapping and Nearest Neighbours . . . 70
5.4.2 RKKY Interlayer Exchange Coupling . . . 71
5.5 Curie Temperature . . . 72
5.5.1 Finite Size Scaling (FSS) . . . 72
5.5.2 Curie Temperature Results . . . 73
5.6 Hysteresis . . . 75
Dynamic Effects and Simulation Protocol . . . 77
5.6.1 RKKY Effects . . . 78

6 Parameter Sweep for Small System 81
6.1 Incubation and Switching Time . . . 82
6.2 Benchmark . . . 83
6.3 Parameter Sweep . . . 85
6.3.1 Effect of STT Field Magnitude . . . 86
6.3.2 RKKY effects . . . 89
Effect on Switching Dynamics . . . 90
6.3.3 STT polarisation in Free layer 2 . . . 93
Effect on Switching Dynamics . . . 96

7 Device scale Synthetic Antiferromagnetic MRAM Simulations 101
7.1 Nucleation and Switching . . . 101
7.2 Top Layer Anisotropy . . . 104
7.3 Thermal effects . . . 106
7.3.1 Thermal Nucleation and Stochastic Limits . . . 107
7.3.2 Simulation Results . . . 108

8 Conclusion 111
8.1 Development of Code . . . 111
8.2 Dynamics of MWE MRAM . . . 112
8.3 Dynamics of Disc MRAM . . . 113
8.4 Summary of Conclusions and Future Work . . . 113

Appendices 114

A Appendix 117
A.1 Python Script: stack_generator.py . . . 117

References 145

List of Tables

1.1 Table of versions of common RAM types, their switching times, and their volatility. 7

5.1 The properties of bulk and interfacial CoFeB and MgO, taken from Sampan-A-Pai *et al.* (1) 65
5.2 Properties of interfacial CoFeB and bulk Ru. 67
5.3 Curie temperature by layer, with critical exponent, showing the lower exchange in RKKY coupling (-1×10^{-23} J/link) compared to bulk and interfacial MgO layers creates a finite size effect and, therefore, a lower Curie Temperature. 76

6.1 Table of RKKY strengths, the time taken to switch in nanoseconds, the percentage increase or decrease from the benchmark calculation, and the type of dynamic. The parameters used are the same as the benchmark simulation (STT in FL1 is 1.0 T , STT in FL2 is 0.0 T) with varying RKKY. 91
6.2 Table of polarisation strength deposited into FL2, the switching time, the deviation from the benchmark simulation, and the qualitative dynamic. 96

List of Figures

1.1 Conflicting STT MRAM requirements. High thermal stability, low writing current, high signal, low resistance, and good integration with CMOS computer architecture is required for viable memory storage. Adapted from figure 3 in Sbiaa *et al.*(2) 6

1.2 Comparison of the basic MRAM structure consisting of layers CoFeB/MgO/CoFeB where the two ferromagnets are aligned antiparallel, and the SAF MRAM structure with a CoFeB/MgO/CoFeB/Ru/CoFeB structure. The non-magnetic layers are shown in grey. 8

2.1 Examples of orbital magnetic moment (a) and intrinsic magnetic moment (b). The arrows in z-direction are shown as perpendicular to the plane of rotation in the anticlockwise direction. 10

2.2 Diagram illustrating magnetic ordering, where (a) is a ferromagnetic state, (b) is an antiferromagnetic state, and (c) is a ferrimagnetic state. 14

2.3 Graph of the RKKY exchange energy plotted against $2k_F R$, where R is the interatomic distance. This shows the first minimum having the strongest antiferromagnetic coupling with negative J_{ij}. The arrows indicate that when J_{RKKY} is positive, the magnetic moments align in parallel, and when J_{RKKY} is negative the magnetic moments align in antiparallel. 17

3.1 Graph of spin dependent tunnelling adapted from Phanwadee (3) . The graph shows down-spin tunnelling through the MTJ barrier to down-spin states, and up-spin tunnelling to up-spin states. 28

3.2 Schematic of electron tunnelling through an amorphous AlO (a) barrier versus the coherent tunnelling that occurs in Fe(001), MgO(001) (b). Adapted from Shinji Yuasa(4) 30

3.3 Diagram of STT in magnetic multilayers composed of a pinned bottom layer, the non-magnetic MgO layer, and the free layer 2, where ferromagnets in (a) are antiparallel, and (b) are parallel. 32

4.1 Recoloured schematic representation by Andrea Meo (5) of the division of a large magnetic system into discrete macrocells (left) where each macrocell has uniform magnetisation (right). 45

4.2 Monte Carlo trial steps (a) is the spin flip, (b) is random, (c) is the small step, (d) is Gaussian. 50

4.3 Recoloured schematic diagram, adapted from J. Fernandez-Roldan's thesis (6), illustrating the LLG dynamics. The local magnetic moment ($\boldsymbol{M}$) precesses around the effective magnetic field ($\boldsymbol{H}_{eff}$). The precession term is shown in purple, and the damping term is shown in pink. 55

5.1 Diagram of the minimum working example (MWE) SAF MRAM with dimensions of $1 \times 1 \times 6$nm, and the dot SAF MRAM where the dot has dimensions $40 \times 40 \times 6$ nm. 60

5.2 Slater-Pauling curve showing the atomic moment (μ/μ_B) against the material alloys number of valence electrons for various transition metal alloys. The Fe-Co alloy being highlighted in blue shows higher saturation magnetisation compared to other magnetic alloys, supporting its use in MRAM free layer for high density memory (7). 61

5.3 Example of hexagonal close-packed HCP and face-centred cubic FCC crystal structure, demonstrating the similarities in structure and packing fraction. 68

5.4 Diagram of the MWE MRAM in VESTA highlighting the interfaces in green, CoFeB in gold, oxygen in red, Mg in orange, and Ruthenium in white. The labelled layers correspond to those in Table 5.3. 70

5.5 Magnetisation ($\boldsymbol{M}$) versus Temperature (T) curve of a simple MRAM stack: CoFeB/MgO/CoFeB. Showing the layer-resolved magnetisation that have different critical exponents (β) from different environments, such as CoFeB interface layer 5, on the surface, exposed to the vacuum. 73

5.6 Snapshots of Magnetisation at various Temperatures in Kelvin for the MRAM stack of CoFeB/MgO/CoFeB. The colour scheme is shown where the (m/m_S) is from pink at -1, to blue at +1. These show the temperature dependence of (m/m_S). 74

5.7 Magnetisation ($\boldsymbol{M}$) versus Temperature (T) curve of the full MRAM stack with CoFeB/MgO/CoFeB/Ru/CoFeB, showing the layer-resolved magnetisation and finite size effects of the top layer where due to weak RKKY interaction the interface layers have a lower critical exponent. 76

5.8 Sweep rate (T/s) dependence of CoFeB/MgO/CoFeB/Ru/CoFeB where the blue line has a sweep rate of 1×10^{13} T/s and the purple line has a sweep rate of 1×10^{11} T/s. The diagrams show the orientation of the pin and SAF free layers at each step. The highly variable sweep rate shows a dynamic hysteresis needing many loop steps to equilibrate (8). 77

5.9 Comparison of hysteresis loops with varying RKKY interaction strength. Seen in the right graph the RKKY interaction reaches the saturation magnetisation ($\pm$ 1) when the applied magnetiic field is less than 5 T. The pink line (-1$\times 10^{-20}$ J/link) and the purple line (-1$\times 10^{-21}$ J/link) in Figure 5.9 (a) show the systems not reaching saturation magnetisation under 10 Tesla. In contrast, the dark blue (-1$\times 10^{-22}$ J/link) and the light blue line (-1$\times 10^{-23}$ J/link) reach saturation magnetisation in less than 5 Tesla. 79

6.1 Diagram of the small system MRAM cell, $1 \times 1 \times 6$ nm 82

6.2 Magnetisation reversal showing three distinct regions, the incubation time in light blue, the reversal time in yellow, and full switching in pink. 83

6.3 Magnetisation switching of MRAM device with zero polarisation injected into FL2. Key parameters: FL2 anisotropy 5×10^{-24} J/link, RKKY exchange coupling -1×10^{-21} J/link, (a) the z components of the bulk SAF layers, (b) and (c) the x, y, and z components of FL1 and FL2. 84

6.4 Simulation of switching occurring with top layer of anisotropy of 5×10^{-24} J/link, RKKY of -1×10^{-21} J/link, and zero polarisation being injected into the top layer. 85

6.5 Non-switching dynamics of MRAM with the STT deposited in FL1 = 0.8 Tesla, demonstrating failure to switch or deflect from initial magnetisation direction. This scheme is typical for low current with a high PMA. 87

6.6 Switching of (a) with STT field in FL1 of 0.95 Tesla, the minimal switching field found when increasing the STT field in 0.05 T increments. (b) STT in FL1 of 1.2 Tesla, (c) STT in FL1 of 1.6 Tesla, where the incubation time is minimal. 88
6.7 Switching dynamics of FL1 plotted in 3D with axis representing the magnetisation direction of $\boldsymbol{m}_x$, $\boldsymbol{m}_y$, and $\boldsymbol{m}_z$. Where (a) has the STT in FL1 of 0.95 Tesla, (b) STT in FL1 of 1.2 Tesla, and (c) STT in FL1 of 1.6 Tesla. 88
6.8 STT in FL1 is 1.9 Tesla, creating dynamic instability which creates a precession that prevents switching. The parameters used are outlined in "Effect of STT Field Magnitude". (a) is the z components of FL1 and FL2, (b) are the xyz components of FL1, (c) are the xyz components of FL2, and (d) is the 3D plot of magnetisation direction in FL1. 90
6.9 STT in FL1 is $1.0T$, STT in FL2 is $0.0T$, the RKKY coupling is -1×10^{-20}, stronger than the benchmark simulation by a factor of 10. This has the effect of increasing the energy barrier such that 1 T is insufficient to switch the system. 92
6.10 Switching where STT in FL1 is $1.0T$, STT in FL2 is $0.0T$, the RKKY coupling is -5×10^{-22} J/link, weaker than the benchmark simulation by half. 93
6.11 Non-Switching where the STT in FL1 is $1.0T$, STT in FL2 is $0.0T$, the RKKY coupling is -1×10^{-22} J/link. This RKKY coupling is weaker than the benchmark simulation (-1×10^{-21} J/link). 94
6.12 Diagram of how the bulk CoFeB layer coming from the current direction acts as a polariser which deposits a percentage of the polarisation onto the interface layer above the non-magnetic spacer layer. This occurs in the MRAM device around both MgO and Ru non-magnetic layers. 94
6.13 Graph of (a) average spin current against layer height, and (b) average spin accumulation against layer height. The parameters of this MRAM have been determined by spin transport 95
6.14 Switching of middle and top layer with top layer of anisotropy of 5×10^{-24}, RKKY of 1×10^{-21} J/link, and 20% polarisation being injected into the top layer. (a) is the z components of the bulk SAF layers, (b) has the x, y and z components of Free layer 1 and (c) has the x, y, and z components of Free layer 2. This leads to the switching being driven by both the polarisation current from bulk middle layer, and the rotation of the middle layer with the antiparallel coupling. 97

6.15 Switching of middle and top layer with top layer of anisotropy of 5×10^{-24}, RKKY of 1×10^{-21} J/link, and 50% polarisation being injected into the top layer. (a) is the z components of the bulk SAF layers, (b) has the x, y and z components of Free layer 1 and (c) has the x, y, and z components of Free layer 2. Compared to Figure 6.14 the switching time is faster, with only the polarisation being changed. 98

6.16 Switching of middle and top layer with top layer of anisotropy of 5×10^{-24}, RKKY of 1×10^{-21} J/link, and 50% polarisation being injected into the top layer. (a) is the z components of the bulk SAF layers, (b) has the x, y and z components of Free layer 1 and (c) has the x, y, and z components of Free layer 2. 98

6.17 Spin torque oscillator scheme where the STT deposited in FL2 is 100% of the STT FL1, leading to no switching occurring and out-of plane rotation ($\neq \boldsymbol{m}_x, \boldsymbol{m}_y$), such that both layers have a slight positive m_z component. 99

7.1 Diagram of a SAF MRAM stack from bottom to top CoFeB/MgO/CoFeB/Ru/CoFeB, where the free layer 1 is in pink, the pinned layer and free layer 2 is in blue, and the non-magnetic MgO and Ruthenium is in grey. The dimensions are 40 x 40 x 6 nm disc. 102

7.2 Lowest three normal modes of MRAM switching in a cylinder, labelled by winding number. From Visscher *et al.* (9) 102

7.3 Example of nucleation on a disc shaped MRAM at 0 K, where the local change occurs on the edge of FL1 before reaching a size where it can propagate in a vortex in the x-y plane around the MRAM device and inducing switching in FL2 under weak RKKY. 103

7.4 MRAM relaxing with 1 T applied STT field, 0 top layer anisotropy, RKKY coupling strength of -1×10^{-22} J/link where the z magnetisation component of FL2 relaxes towards zero, while the x and y component oscillates. 105

7.5 Diagram of the movement of the magnetic moment of the SAF MRAM relaxing with 1 T applied STT field, 0 top layer anisotropy, RKKY coupling strength of -1×10^{-22} J/link where the m_z of FL2 relaxes towards $m_z = 0$, while the x and y component of FL2 oscillates. This shows (a) the FL1 magnetic moment movement and (b) the FL2 magnetic moment oscillating in the x and y plane. 106

7.6 A simulated easy-axis hysteresis loop by Andrea Meo (10) for 1 nm thick 50 nm diameter nanodot at temperatures 5 K and 300 K, showing a reduction in coercivity at 300 K compared to 5 K 107

7.7 SAF MRAM dot switching with FL2 anisotropy of 5×10^{-24}, RKKY coupling strength of -1×10^{-22} J/link, 1 T of applied STT field, and 0% of the polarised field deposited in FL2. (a) has the z components of FL1 and FL2, (b) and (c) has the x, y,and z components of FL1 and FL2 respectively. 109
7.8 SAF MRAM in the Spin Torque Oscillation scheme at 300 K, with FL2 anisotropy of 5×10^{-24} J/link, RKKY coupling strength of -1×10^{-22}, 1 T of applied STT field, and 0% of the polarised field deposited in FL2. (a) has the z components of FL1 and FL2, (b) and (c) has the x, y,and z components of FL1 and FL2 respectively. The top layer oscillates with a frequency of ≈ 17 GHz 110

Nomenclature

List of Abbreviations

Abbreviation	Description
AF	Antiferromagnet
AI	Artificial Intelligence SAF
Synthetic Antiferromagnet	
bcc	Body-Centred Cubic
fcc	Face-Centered Cubic
hcp	Hexagonal Clos-Packed
CEF	Crystal Electric Field
DFT	Density Functional Theory
DMI	Dzyaloshinskii-Moriya Interaction
DRAM	Dynamic Random Access Memory
SRAM	Static Random Access Memory
SSD	Solid State Drive

Abbreviation	Description
HDD	Hard Disk Drive
HPC	High Performance Computing
Δ	Thermal Stability Factor
$\boldsymbol{H}_d$	Demagnetization Field
CPU	Central Processing Unit
EY	Elliott-Yafet (mechanism)
DP	D'yakonov-Perel (mechanism)
FL	Free Layer
TMR	Tunnel Magnetoresistance
MC	Monte-Carlo
MCMC	Markov Chain Monte Carlo
ZLF	Zhang-Levy Fert
IEC	Interlayer Exchange Coupling
LLG	Landau-Lifshitz-Gilbert equation
MRAM	Magnetic Random Access Memory
MTJ	Magnetic Tunnel Junction
MWE	Minimal Working Example
PMA	Perpendicular Magnetic Anisotropy
RKKY	Ruderman-Kittel-Kasuya-Yosida interaction
sLLG	Stochastic Landau-Lifshitz-Gilbert equation
SOT	Spin-Orbit Torque
STT	Spin Transfer Torque
TSFD	Thermal Switching Field Distribution

Abbreviation	Description
VAMPIRE	Vector Atomic Magnetism Program for Investigations of Reversal and Exchange
VESTA	Visualisation for Electronic and Structural Analysis
CMOS	Complimentary Metal-Oxide-Semiconductor

1 Motivation

1.1 Motivation

Demand for high-performance memory is surging in the "data age" due to computer applications like autonomous cars, smart home devices, high-performance computing and artificial intelligence (AI). These applications require memory storage which overcomes the competing requirements illustrated in the "pentalemma" shown in Figure 1.1 (2). High-powered computing and AI training need large data sets, parallel processing, and constant parameter rewriting, placing immense strain on traditional memory systems. This strain has led to worldwide shortages of SSDs, HDDs, and DRAM, which are predicted to last into 2027. Some projections push the RAM shortage into 2028 (11).

Modern computers primarily use Dynamic Random Access Memory (DRAM) or Static Random Access Memory (SRAM), both of which are volatile systems that require constant power for data retention. This high power consumption occurs even when read/write functions are not taking place (12). In high-performance computing (HPC) and data centres, the power consumed by data movement between GPUs and CPUs can surpass the power required for computation itself (13). Spin Transfer Torque Magnetic-RAM (STT-MRAM) has emerged as a promising

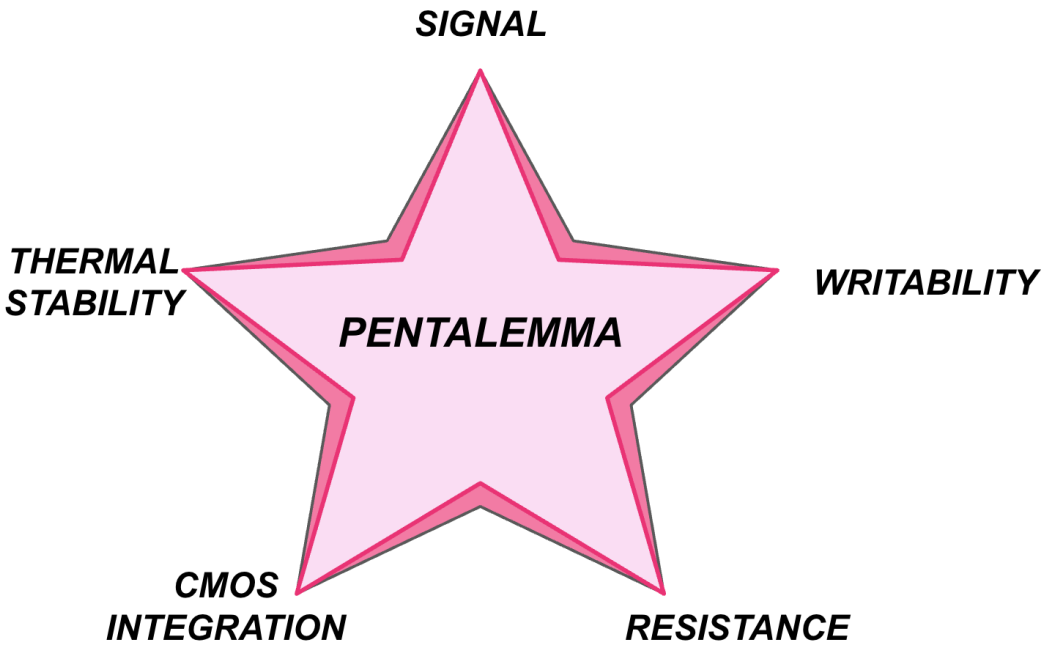


Figure 1.1: Conflicting STT MRAM requirements. High thermal stability, low writing current, high signal, low resistance, and good integration with CMOS computer architecture is required for viable memory storage. Adapted from figure 3 in Sbiaa *et al.*(2)
.

candidate to overcome these issues (14). Despite developments since its initial production, advancements in critical current switching, speed, and scalability are still required before Spin Transfer Torque (STT) MRAM can compete effectively with conventional RAM designs. The critical current in particular is one of the main barriers between STT-MRAM and commercial viability.

Magnetic RAM (MRAM) that utilises a synthetic antiferromagnetic free layer is a promising candidate. The SAF free layer increases the thermal stability, while only slightly increasing the critical current (15), which helps mitigate the conflicting requirements of the pentalemma. The SAF free layer also reduces stray magnetic fields allowing for a higher density of memory by minimising magnetic

"crosstalk" between MRAM cells. While SAF MRAM has great potential, its development is in the early stages. Its parameter space is not fully understood, requiring an atomistic approach to model its underlying physics. This approach is required to develop a wider understanding of its switching dynamics and magnetic properties, and to determine how varying parameters affect the MRAM's behaviour, allowing the development of faster, denser, and more reliable MRAM devices.

1.2 Magnetic Random Access Memory (MRAM)

RAM serves as a computer's working memory because its data can be read or written in the same amount of time regardless of its physical location on the RAM device. This contrasts with other memory devices such as SSDs and HDDs where access time is highly dependent on the data's physical location. The differences between volatile and non-volatile memory and is shown in Table 1.1, where SRAM memory is faster than all non-volatile memory.

Table 1.1: Table of versions of common RAM types, their switching times, and their volatility.

RAM version	**Primary use**	**Switching time**	**Volatility**
SRAM	CPU Cache	$<$ 1ns	volatile
DRAM	Main memory	10 - 100 ns	volatile
STT-MRAM	Embedded	1 - 10 ns	non-volatile
NAND flash	Storage	$>$ 1 ms	non-volatile

A Magnetic RAM cell in its most basic state is a magnetic tunnel junction (MTJ) consisting of two ferromagnetic layers separated by a non-magnetic spacer layer. One ferromagnet is pinned, creating a difference in resistance depending on whether the ferromagnets are aligned in parallel or antiparallel (16).

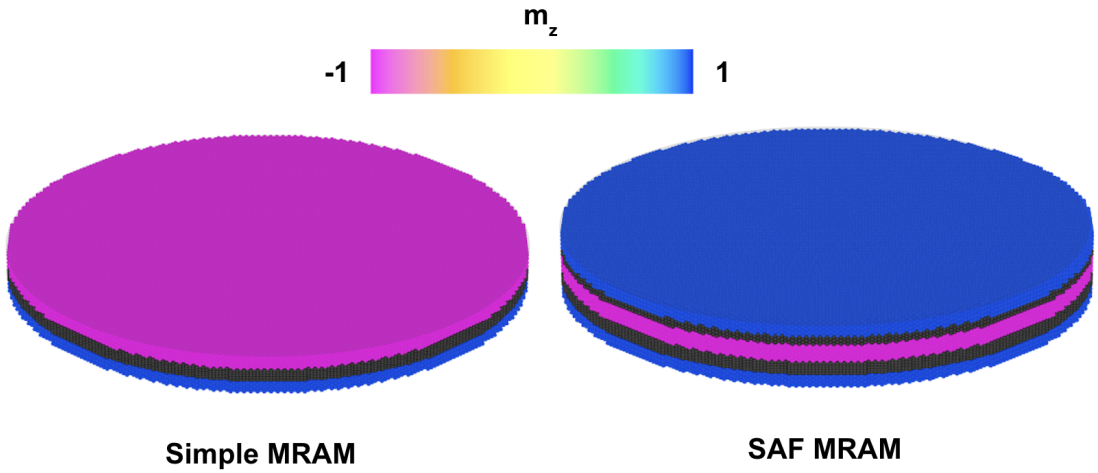


Figure 1.2: Comparison of the basic MRAM structure consisting of layers CoFeB/MgO/CoFeB where the two ferromagnets are aligned antiparallel, and the SAF MRAM structure with a CoFeB/MgO/CoFeB/Ru/CoFeB structure. The non-magnetic layers are shown in grey.

The synthetic antiferromagnetic (SAF) MRAM device used in this thesis has a pinned bottom layer, a non-magnetic, crystalline, MgO layer, and an SAF free layer consisting of two CoFeB layers coupled antiferromagnetically by a Ruthenium spacer layer. The magnetic tunnel junction (MTJ) is composed of a bottom layer pinned by the exchange bias, a non-magnetic crystalline layer, and a middle layer (Free Layer 1). The Free Layer 1 is also part of the synthetic antiferromagnet, seen in Figure 1.2 (a) and (b), where the structure in (a) makes up the bottom three layers of the SAF MRAM in (b).

2 Origins of Magnetism

The fundamental magnetic properties, such as magnetic ordering, as well as the behaviours critical to making a functioning device, for instance thermal stability, and magnetic switching, arise from the interactions between atomic sites and govern the dynamic and structural properties of the material. Therefore, for a comprehensive understanding of the device this chapter reviews the fundamental quantum origins of magnetic moments and the exchange interaction, which leads to the bulk magnetic order and physical basis for later simulations.

2.1 Atomic Origins of Magnetism

The early history of magnetism is marked by the invention of the south-pointing spoon (sīnán) (17), a compass carved from a lodestone which dates back to China during the Han dynasty (c. 202 BC – 220 CE).

Atomistic magnetic moments originate both from the intrinsic spin of electrons and their orbital motion around the nucleus. The intrinsic spin can be visualised as an electron spinning on its axis as seen in Figure 2.1 (b). The intrinsic spin provides each electron with an inherent magnetic moment, characterized by a spin quantum number of 1/2. Nevertheless, since an electron cannot classically "rotate", this analogy has limitations. Additionally, the orbital motion of an

electron around the nucleus generates an orbital magnetic moment, which can be modelled as a current loop around the nucleus.

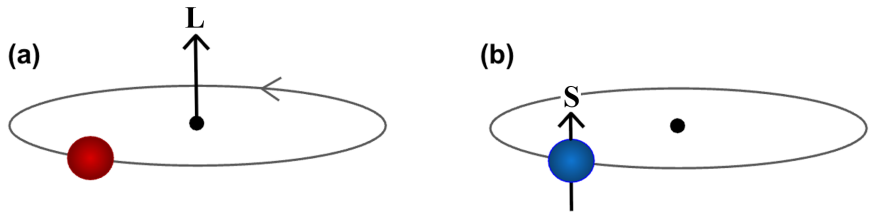


Figure 2.1: Examples of orbital magnetic moment (a) and intrinsic magnetic moment (b). The arrows in z-direction are shown as perpendicular to the plane of rotation in the anticlockwise direction.

The orbital magnetic moment shown in Figure 2.1 (a) is the result of the angular motion of the electron (charge e) around a central potential such as an atomic nucleus. Classically, this is equivalent to a circular current loop. The current (I) generated from an electron moving around this current loop with angular frequency (ω) is: $I = -\frac{e\omega}{2\pi}$. The magnetic moment ($\mu_L$) is derived from the product of $I \cdot A$ where the area $A = \pi r^2$ of a singular electron orbiting a nucleus, resulting in equation 2.1:

$$\mu_L = I \cdot A = (-\frac{e\omega}{2\pi}) \cdot (\pi r^2) = -\frac{e\omega r^2}{2} \tag{2.1}$$

However, this classical description is insufficient because it does not take into account quantization of orbital angular momentum. The quantum orbital angular momentum is quantized in units of $\hbar$ so that $L_z = m_l\hbar$, where m_l is the magnetic quantum number (m_l = -l, ..., 0, ..., +l) (18). Therefore, the z-component of the orbital magnetic moment is:

$$\mu_{L,z} = -\frac{e}{2m_e}L_z = -\frac{e}{2m_e}(m_l\hbar) \tag{2.2}$$

$$\mu_{L,z} = -m_l(\frac{e\hbar}{2m_e}) = -m_l\mu_B \tag{2.3}$$

where m_l is a positive integer associated to one of the electron orbitals, i.e.: s, p, d, f.

In a bulk ferromagnetic transition metal crystal lattice, the crystal electric field (CEF) effectively pins the 3d partially-filled electron orbitals motion. This contrasts with the lanthanides where the partially filled outer 3d shell shields the 4f electrons so that they do not experience the same level of orbital quenching. This pinning action breaks the rotational symmetry that is present in an isolated atom. As a result of this phenomenon, known as orbital moment quenching (19), the primary source of magnetic moments in these materials is from the intrinsic spin of the electrons as seen in Figure 2.1 (b).

An electron's intrinsic spin can be represented by an angular momentum operator $\hat{\boldsymbol{S}}$ and has components $(\hat{S}_x, \hat{S}_y, \hat{S}_z)$, where the components do not commute, meaning no two components can be known simultaneously:

$$[\hat{S}_i, \hat{S}_j] = i\hbar\epsilon_{ijk}\hat{S}_k \tag{2.4}$$

where $\hat{S}_i$ and $\hat{S}_j$ are spin angular momentum operators of $\hat{\boldsymbol{S}}$, ϵ_{ijk} is the completely antisymmetric tensor, the Levi-Civita symbol, , $\hat{S}_k$ is the remaining component of the spin angular momentum operator, i is the imaginary unit, and $\hbar$ is the reduced Planck constant.

The equation that relates the electron's spin magnetic moment operator $(\boldsymbol{\mu}_s)$

to its spin angular momentum operator ($\hat{\boldsymbol{S}}$) is:

$$\boldsymbol{\mu}_s = -g_e \mu_B \frac{\hat{\boldsymbol{S}}}{\hbar} \tag{2.5}$$

where $\hat{\boldsymbol{S}}$ is the spin angular momentum of the electron, $\boldsymbol{\mu}_s$ is the spin magnetic dipole moment, μ_B is the Bohr magneton, which is a fundamental physical constant defined as $\mu_B = e\hbar/2m_e$, and g_e is its g-factor.

The negative sign is due to the electron's negative charge resulting in an antiparallel alignment between its magnetic moment and spin angular momentum vector. The maximum measurable component for $\boldsymbol{\mu}_s$ along a specific axis (z) is:

$$\mu_{s,z} = g_e m_s \mu_B \tag{2.6}$$

where an electron is a spin $\frac{1}{2}$ particle, the possible spin projection is $m_s = \pm\frac{1}{2}$. The maximum measurable component is equal to $+\frac{1}{2}$, and therefore:

$$\mu_{s,z} = (2.0023) \cdot \left(\frac{1}{2}\right) \cdot \mu_B \tag{2.7}$$

$$\mu_{s,z} \approx 1.00115 \mu_B \tag{2.8}$$

The g-factor is $g_e = 2$ when derived from the Dirac equation (20). However, in early experiments (21) there was an observed small deviation from prediction known as the anomalous magnetic moment ($a_e = (g-2)/2$) and, with modifications from QED, the g-factor agrees with observed experimental results and is equal to ≈ 2.0023 (22).

2.1.1 Magnetic States and Ordering

Macroscopic magnetic ordering is a form of cooperative (ordered) magnetism where the bulk magnetic state is governed by the interaction between microscopic magnetic moments. The ordering is primarily determined by the exchange interaction, a quantum mechanical phenomenon that originates from the Pauli exclusion principle (23). This ordering gives rise to magnetic states such as the ferromagnetic, antiferromagnetic, and ferrimagnetic state as seen in Figure 2.2.

The Pauli principle says that the total wavefunction of two electrons (fermions) must be antisymmetric upon exchange. This restriction leads to an energy difference based on spin orientation. Therefore, electrons with parallel spins ($\uparrow\uparrow$) must have an antisymmetric spatial wavefunction, causing them to avoid each other, creating an "exchange hole". This lowers their mutual Coulomb repulsion energy. Conversely, electrons with anti-parallel spins ($\uparrow\downarrow$) can occupy the same spatial region, leading to higher Coulomb repulsion energy. The difference in the system's total energy, which is dependent on the relative spin orientation, is the effective exchange energy. The collective interaction between adjacent atoms then gives rise to distinct types of highly ordered magnetic states: ferromagnetism, antiferromagnetism, and ferrimagnetism (24).

In comparison, the independent (unordered) magnetic states, diamagnetism and paramagnetism, are characterised by the uncoupled, independent response of their magnetic moment to an external field and lack any internal long-range order.

Ferromagnetism

Ferromagnetism is characterised by spontaneous parallel magnetic ordering of adjacent magnetic moments, as seen in Figure 2.2 (a), resulting in a large macroscopic

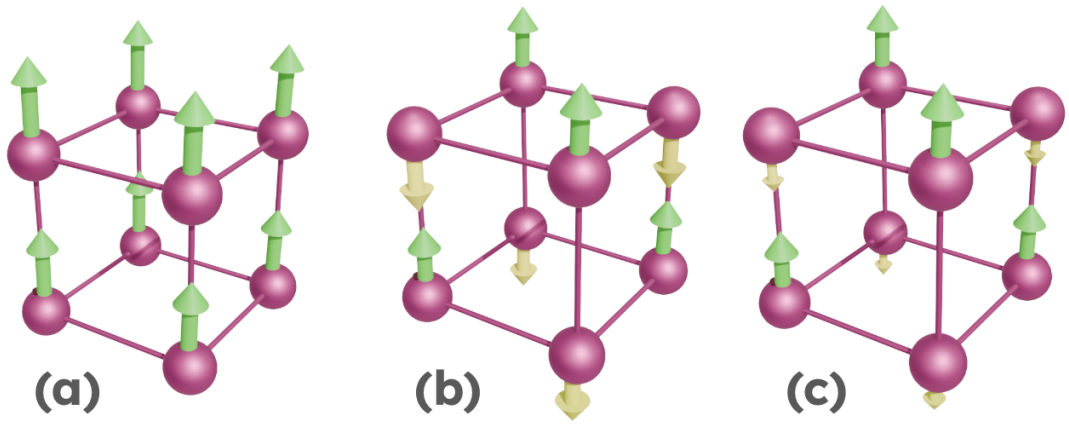


Figure 2.2: Diagram illustrating magnetic ordering, where (a) is a ferromagnetic state, (b) is an antiferromagnetic state, and (c) is a ferrimagnetic state.

net magnetization (M). This phenomenon leads to spontaneous magnetisation, even when there is no applied field. When an external field is applied, the magnetisation aligns with the field and corresponds to a large, non-linear positive magnetic susceptibility. While the ferromagnet remains below the Curie temperature (T_C) the ferromagnet maintains long-range order.

Early models of magnetism such as the Weiss field described an internal effective "Weiss field" that aligns neighbouring spins. While the Weiss field successfully describes the macroscopic consequences, like the Curie temperature, it is a classical construct and does not consider the exchange's origin. The exchange interaction is the origin of ferromagnetism and emerges from the Pauli exclusion principle, which requires that the total wave function of identical electrons must be antisymmetric (25). This exchange is why ferromagnets have long-range order.

$$\boldsymbol{\Psi}_{total} = \psi(\boldsymbol{r}_1, \boldsymbol{r}_2)\chi(\boldsymbol{s}_1\boldsymbol{s}_2) \tag{2.9}$$

In the ferromagnetic state (↑↑), where the spin part χ is symmetric, the spatial component of their wave function $\psi(\boldsymbol{r}_1, \boldsymbol{r}_2)$ must be antisymmetric. This antisymmetric spatial function forces electrons to keep greater distances from each other compared to the symmetric spatial function, leading to reduced inter-electron Coulomb repulsion energy. This reduced Coulomb repulsion energy is larger than the increase in kinetic energy, lowering the system's total energy. This energetic preference for parallel alignment of spins is the driver for ferromagnetism.

Antiferromagnetism

Antiferromagnetism is a magnetic ordering seen in Figure 2.2 (b) where neighbouring atoms spontaneously align their moments in an antiparallel pattern of equal magnitude, leading to no net macroscopic magnetic moment. This is governed by the exchange integral (J), a parameter that arises from the Pauli exclusion principle and coulomb repulsion. The energy is minimised when the exchange integral is negative $J < 0$ through having an antiparallel alignment. A related ordering is ferrimagnetism, seen in Figure 2.2 (c), which exhibits similar antiparallel microscopic alignment; however, the moments are unequal in magnitude and result in a net magnetic moment behaving macroscopically comparably to a ferromagnet.

At the Néel temperature magnetic susceptibility of the solid reaches a peak, below the Néel temperature antiferromagnets tend to have a low, but positive magnetic susceptibility from the spins aligning slightly to an external magnetic field. The maximum χ is far less than a ferromagnet or ferrimagnet.

While direct exchange is responsible for the strong parallel ordering in single ferromagnetic layers, more advanced structures such as magnetic multilayers rely on indirect exchange coupling to manipulate alignment across multiple layers, such

as the Ruderman–Kittel–Kasuya–Yosida (RKKY) interaction (26; 27; 28). A synthetic antiferromagnet is a structure used in spintronic devices consisting of two thin ferromagnets separated with a metallic non-magnetic spacer layer like Ruthenium (29). The RKKY interaction within a SAF MRAM mediates the interlayer coupling and, within the context of this thesis, the SAF is critical for switching the top free layer.

In MRAM, SAFs are used to improve thermal stability, where the exchange coupling between layers prevents unintentional switching, and to reduce stray fields, ensuring the magnetisation of the MRAM cell does not influence neighbouring cells.

2.2 Ruderman–Kittel–Kasuya–Yosida (RKKY) Interaction

The RKKY interaction describes a long-range coupling between two localised magnetic moments, S_i and S_j separated by distance R, and mediated by the conduction electron gas. Physically, the first moment (S_i) locally polarises the surrounding electrons via the $s-d$ exchange interaction, generating an oscillatory spin density known as a Friedel oscillation. The second magnetic moment (S_j) then interacts with the Friedel oscillation, generating a long-range coupling between S_i and S_j.

The sign of the coupling, ferromagnetic or antiferromagnetic, is dependent on distance R and the Fermi wave vector (k_F) of the conduction medium, the sea of itinerant electrons in the metal (30). In multilayer structures like MRAM, this long-range interaction is termed an indirect exchange coupling (IEC). The strength of the coupling of the ferromagnets is determined by the thickness of the non-magnetic spacer, with the oscillatory nature of the coupling strength across

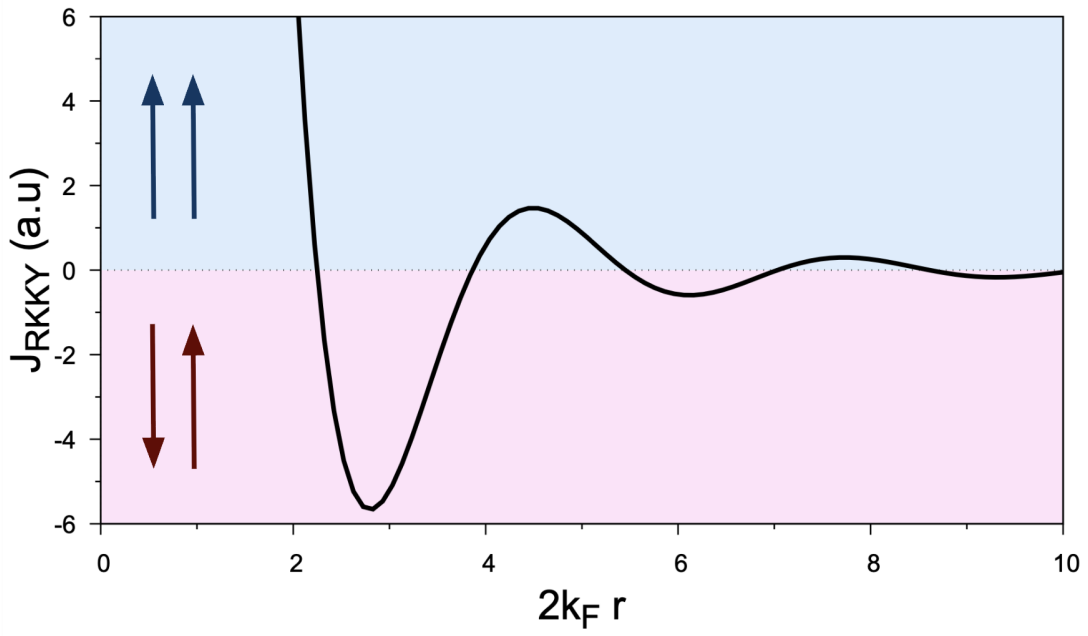


Figure 2.3: Graph of the RKKY exchange energy plotted against $2k_FR$, where R is the interatomic distance. This shows the first minimum having the strongest antiferromagnetic coupling with negative J_{ij}. The arrows indicate that when J_{RKKY} is positive, the magnetic moments align in parallel, and when J_{RKKY} is negative the magnetic moments align in antiparallel.

the spacer thickness between the ferromagnets being shown in Figure 2.3 and described in the Equation 2.10. The full equation is found through calculating the change in total energy in the case of spin $\boldsymbol{S_i}$ interacting with spin $\boldsymbol{S_j}$. This results in a second-order perturbation where the RKKY that forms is between $\boldsymbol{S_i}$ and $\boldsymbol{S_j}$ separated by distance R:

$$J_{RKKY} \propto \frac{sin(2k_FR) - 2k_FRcos(2k_FR)}{(2k_FR)^4} \tag{2.10}$$

where the sign of J_{RKKY} determines parallel or antiparallel alignment, k_F is the Fermi wave vector of the spacer layer, and R is the distance separating $\boldsymbol{S_i}$ and $\boldsymbol{S_j}$, in multilayer is equivalent to r_{spacer}.

The functional form of the coupling is the result of integrating the perturbation over the spherical Fermi surface of the conduction electrons. This process generates the Ruderman-Kittel function, which contains the $sin(2k_FR)$ and $-2k_FRcos(2k_FR)$ terms that dictate the oscillatory behaviour and the $1/R^4$ term which determines the strength of damping.

When R becomes large ($R \gg 1/k_F$), the terms inside the brackets, $sin(2k_FR)$ and $-2k_FRcos(2k_FR)$, can be analysed to find which term becomes dominant for oscillation and decay. While the whole term is damped by $1/(2k_FR)^4$, the $-2k_FRcos(2k_FR)$ dominates as R becomes large, creating the simplified form:

$$J_{RKKY}(R) \propto \frac{-cos(2k_FR)}{(2k_FR)^3} \tag{2.11}$$

where the sign of J_{RKKY} determines parallel or antiparallel alignment, and r_{spacer} is the thickness of the spacer layer between the two ferromagnetic layers. When $J_{RKKY} > 0$, the RKKY interaction favours parallel alignment and when $J_{RKKY} < 0$, it favours antiparallel alignment.

3

Introduction to Spintronics

Spintronics, a portmanteau of spin electronics, is a field that utilises the intrinsic spin of the electron, in addition to its charge, for information processing and storage. An application of this is Spin Transfer Torque Magnetic Random Access Memory (STT-MRAM). A key part of the STT-MRAM is the magnetic tunnel junction (MTJ), which is used to store binary bits, aligned in antiparallel for "0" and parallel for "1".

This chapter details the theoretical framework of the spintronics investigated in this thesis. It transitions from a microscopic description of spin transport, which underpins effects such as spin accumulation and Tunnel Magnetoresistance (TMR), into the macroscopic magnetisation dynamics such as STT. These theoretical frameworks provide the basis for simulations outlined later in this thesis.

A comprehensive understanding of spin transport is essential as it is the backbone of modern spintronics technologies such as TMR, GMR, and STT (31; 32). It is also important to recognise the difference between a charge current, which is the net transport of electric charge through a material, and a spin current, which is the net transport of spin angular momentum.

3.1 Spin Transport and Magnetisation Switching

In 1936, the Mott two-channel model described electron conduction by treating spin-up and spin-down electrons as separate, independent transport channels (33). In the two channel model, a pure spin current results from two spin currents of opposite spin propagating in antiparallel alignment. This leads to a net spin current despite having zero net charge current. Pure spin currents are sought after in spintronics because, unlike charge currents, they do not produce Joule heating, resulting in improved energy efficiency, device density and thermal stability. This movement of spin angular momentum, when absorbed or reflected by a magnetic layer, generates a torque (STT) which switches the magnetisation direction.

3.1.1 Spin Polarisation

Ferromagnetic materials are intrinsically spin-polarised due to the exchange interaction. Spin polarisation in a non-magnetic material is typically achieved by optical spin injection or the injection of charge carriers from a ferromagnet into a non-magnet (a spin injector) (34). While the ideal spin injector would inject a single spin type with 100% efficiency, ferromagnets tend to transmit spin up and spin down unequally. Spin polarisation is the imbalance in population between spin-up ($n_\uparrow$) and spin-down ($n_\downarrow$) conduction electrons, typically described by equation 3.1 which can be used to describe the amount of spin accumulation (Ξ) in a non-magnet (35).

$$\Xi = \frac{n_\uparrow - n_\downarrow}{n_\uparrow + n_\downarrow} \tag{3.1}$$

Where Ξ is the net spin concentration polarisation, or spin accumulation, and $n_\uparrow$ and $n_\downarrow$ is the concentration of spin up and spin down electrons respectively.

Equation 3.2 describes the intrinsic material property, the density of states polarisation (P_D) at the Fermi level, and quantifies the degree of intrinsic spin polarization.

$$P_D = \frac{N_i^{\uparrow}(E_F) - N_i^{\downarrow}(E_F)}{N_i^{\uparrow}(E_F) + N_i^{\downarrow}(E_F)} \tag{3.2}$$

where $N_i^{\uparrow}$ is the density of states for spin-up ($\uparrow$) at the Fermi energy (E_F), and $N_i^{\downarrow}$ is the density of states for spin-down ($\downarrow$) at the Fermi energy (E_F), at site i. $N_i^{\uparrow}(E_F)$ and $N_i^{\downarrow}(E_F)$ dictate the availability of spin-up and spin-down electrons for current flow. This difference in available spin-up and spin-down states at E_F leads to the band splitting seen in ferromagnets like Nickel or Cobalt, where the minority spin states may be larger. This imbalance creates the spin-polarised current, which is one of the mechanisms used to switch the magnetisation of the free layer in MRAM through spin transfer torque (STT).

3.1.2 Spin Accumulation

Spin accumulation ($\Delta\mu$) is described as the non-equilibrium difference in electrochemical potentials between the spin-up ($\uparrow$) and spin-down ($\downarrow$) electron populations (36).

$$\Delta\mu = \mu_{\uparrow} - \mu_{\downarrow} \tag{3.3}$$

where $\Delta\mu$ is the spin accumulation, defined as the difference between the electrochemical potentials ($\mu_{\uparrow}$ and $\mu_{\downarrow}$) of the spin-up and spin-down electron populations. In equilibrium $\mu_{\uparrow} = \mu_{\downarrow}$, resulting in a net spin accumulation of zero. This state, where there is no spin accumulation, can be driven out of equilibrium by injecting a spin-polarised current, creating a non-zero potential that relaxes through spin-flip scattering.

This imbalance typically arises when spin current flows across an interface, such

as from a ferromagnet to a non-magnetic material (37). Due to the conservation of angular momentum, the spin current, driven by $\Delta\mu$, transfers angular torque to an adjacent free layer. This process, known as Spin Transfer Torque, enables the magnetisation direction of the adjacent free layer to be switched in devices like MRAM.

The spin accumulation decays away from the interface into the bulk of the materials (38). This decay occurs primarily through mechanisms such as spin-flip scattering and spin dephasing over what is known as the spin diffusion length (λ_{sdl}). λ_{sdl} is the distance required for the spin imbalance to decay to $1/e$ of its maximum magnitude at the interface and is defined as:

$$\lambda_{\text{sdl}} = \sqrt{D\tau_{\text{sf}}} \tag{3.4}$$

where D is the diffusion constant, and τ_{sf} is the spin-flip relaxation time. This relationship is from the spin-diffusion equation and is derived in the following section.

3.1.3 Spin Diffusion

Spin diffusion is the transport of non-equilibrium spin polarisation away from a local imbalance, such as an interface, via a diffusive spin current, allowing spin polarisation to propagate beyond the ballistic range of the electron (39). This distance, defined as the spin diffusion length λ_{sdl}, is the average distance an electron can travel before its spin direction is randomised due to spin-flip relaxation which is the process of an electron changing its spin state, such as from spin-up to spin-down (40).

Spin diffusion is modelled using transport theories such as the Drift-Diffusion

Model (DDM) in equation 3.5 or the Two-Channel Model. The time-dependant DDM for spin accumulation $\boldsymbol{s}$ is (41; 42):

$$\frac{\partial \boldsymbol{s}}{\partial t} = D\nabla^2 \boldsymbol{s} + \mu(\boldsymbol{E} \cdot \nabla)\boldsymbol{s} - \frac{\boldsymbol{s}}{\tau_{\text{sf}}} + \frac{P}{e}\nabla \cdot \boldsymbol{J}_c \hat{\boldsymbol{m}} \tag{3.5}$$

where $\frac{\partial \boldsymbol{s}}{\partial t}$ is the rate of change of spin accumulation $\boldsymbol{s}$, $D\nabla^2 \boldsymbol{s}$ is the diffusion term, representing the spatial spreading of $\boldsymbol{s}$, $\mu(\boldsymbol{E} \cdot \nabla)\boldsymbol{s}$ is the spin-drift term, where $\boldsymbol{s}$ is driven by the electric field $\boldsymbol{E}$, $-\frac{\boldsymbol{s}}{\tau_{\text{sf}}}$ is the spin relaxation term representing exponential decay from spin-flip events over the spin-flip time τ_{sf}, and $\frac{P}{e}\nabla \cdot \boldsymbol{J}_c \hat{\boldsymbol{m}}$ is the source term representing the generation of $\boldsymbol{s}$ from a polarised charge current ($\boldsymbol{J}_c$) with polarisation P along unit vector $\hat{m}$.

The spin diffusion length λ_{sdl} is derived by solving the DDM under the steady state, diffusion-only conditions where the time derivative is zero ($\frac{\partial \boldsymbol{s}}{\partial t} = 0$) and drift effects are negligible ($\boldsymbol{E} = 0$).

The general expression for the diffusive component of spin current density (j_m) is given by Fick's Law of Diffusion (43), in relation to the diffusive charge current, $j_{diff} \propto -\nabla n$):

$$j_m \propto -D_{eff}\frac{\partial \delta m}{\partial x} \tag{3.6}$$

where j_m is the spin current density, D_{eff} is the effective spin diffusion constant, and δm is the non-equilibrium spin accumulation.

Under the steady state, diffusion-only conditions, the simplified DDM becomes a diffusion-relaxation equation (setting $\nabla \cdot j_m = -\delta m/\tau_{\text{sf}}$):

$$-\frac{eD_{eff}}{2}\nabla^2 \delta m = -\frac{\delta m}{\tau_{\text{sf}}} \tag{3.7}$$

which simplifies to the characteristic differential equation for spin accumulation m

along axis x, and by setting $D_{eff} \rightarrow D$ for generality:

$$\frac{d^2m}{dx^2} = \frac{m}{D\tau_{\text{sf}}} \tag{3.8}$$

where the characteristic length, L_s is found by comparing:

$$\frac{1}{L_s^2} = \frac{1}{D\tau_{\text{sf}}} \tag{3.9}$$

which results in the fundamental relationship between spin diffusion length :

$$\lambda_{\text{sdl}} = \sqrt{D\tau_{\text{sf}}} \tag{3.10}$$

Spin-flip relaxation randomises the electron's spin and is primarily governed by the Elliott-Yafet mechanism (EY) (44) and the D'yakonov–Perel (DP) (45)mechanisms, both arising from spin-orbit coupling (SOC).

The Elliott-Yafet (EY) is a dominant spin-relaxation model in metals and some semiconductors. A weak relativistic SOC slightly cants the electron's spin state mixing spin-up and spin-down components. Spin-flipping occurs spontaneously during momentum scatter events, such as impact with impurities. This results in the EY spin relaxation time is inversely proportional to the momentum relaxation time - $\tau_{EY} \propto 1/\tau_m$.

The D'yakonov–Perel (DP) mechanism occurs in materials lacking inversion symmetry (non-centrosymmetric materials), such as semiconductors, or at interfaces with strong structural inversion asymmetry. These spin orbit interactions originate from the lack of inversion symmetry: the Dresselhaus interaction, which arises from the bulk crystal structure, and the Rashba interaction, which arises from structural inversion asymmetry at the interface.

An example of the Rashba effect is the interface in MRAM between CoFeB/MgO and CoFeB/Ru (46). When an electron is in this environment it will experience a strong spin orbit interaction. The Rashba and Dresselhaus interactions lift the degeneracy of electronic bands for non-zero wave-vectors ($k \neq 0$) between the spin-up and spin-down electrons. This band splitting causes an effective magnetic field (B_{eff}), that the electron precesses around (47; 48).

$$\boldsymbol{B}_{eff} \propto \boldsymbol{E} \times \boldsymbol{k} \tag{3.11}$$

where $\boldsymbol{B}_{\text{eff}}$ is the effective magnetic field vector, $\boldsymbol{E}$ is the electric field vector, at the normal to an interface, and $\boldsymbol{k}$ is the electron's wave vector.

The precession around the B_{eff} is coherent between scattering events. Spin relaxation (τ_{sf}) occurs because scattering randomly changes the electron's momentum ($\boldsymbol{k}$), which randomises the axis of precession leading to rapid dephasing and the decay of the net spin accumulation. The relaxation time is directly proportional to the momentum relaxation time $\tau_{DP} \propto \tau_m$. Therefore, in frequent scattering events, short τ_m, relaxation is suppressed. This is known as the motional narrowing regime. Models that use a single time constant for discrete spin-flip transitions, such as the drift-diffusion model and the two-channel model, lack accuracy when DP, which is based on continuous spin dephasing, becomes the dominant mechanism.

To accurately model spin transport across multilayers, the DDM must be solved independently for each bulk multilayer and coupled across interfaces using boundary conditions that account for spin-dependent scattering, reflection, and transmission, and ensure two conservation laws:

The continuity of spin chemical potential ($\Delta\mu$):

$$\Delta\mu_N = \Delta\mu_F \tag{3.12}$$

where, μ_N and μ_F are the non-equilibrium chemical spin potentials in the non-magnet (N), and ferromagnet (F).

And the conservation of spin current ($\boldsymbol{J}_s$):

$$\boldsymbol{J}_{s,N} - \boldsymbol{J}_{s,F} = \boldsymbol{J}_s^{interface} \tag{3.13}$$

where $\boldsymbol{J}_s^{interface}$ is the spin current density absorbed or lost at the interface due to scattering perpendicular to the boundary, and $\boldsymbol{J}_{s,N}$ and $\boldsymbol{J}_{s,F}$ are the spin current densities just outside interface layers N and F.

While the DDM is effective for bulk materials, it fails to capture the complex, non-equilibrium spin dynamics occurring within a few atomic layers of the interface of strong ferromagnets. The spin mixing conductance ($G^{\uparrow\downarrow}$) is the parameter used to link the DDM to these complex interfacial dynamics, relating the boundary's spin current density loss to the difference in spin accumulation ($\Delta\mu$) across it (49; 50):

$$\boldsymbol{J}_S^{interface} \propto Re[G^{\uparrow\downarrow}](\Delta\mu_F - \Delta\mu_N) \tag{3.14}$$

where $Re[G^{\uparrow\downarrow}]$ is the real part of the SMC associated with the transfer of spin angular momentum. The results for the spin current profile $\boldsymbol{J}_s$ are the inputs for the Slonczewski-Berger formalism used to calculate the spin transfer torque.

3.1.4 Magnetic Tunnel Junction (MTJ) and Tunnel Magnetoresistance (TMR)

Tunnel magnetic resistance (TMR) was first discovered by Michel Jullière in 1975 in Fe/Ge-O/Co junctions at very low temperatures (4.2 K) (35) but, the effect was small, difficult to easily reproduce, and non-existent at room temperature. In 1995 independent groups led by Moodera and Miyazaki used an Al_2O_3 amorphous tunnel barrier to create reproducible TMR ratios at room temperature. This achievement added to interest in Giant Magnetoresistance (GMR) and led to Magnetic Tunnel Junctions (MTJs) which became the superior methodology for applications like MRAM and read-heads.

Tunnel magnetic resistance is a result of spin dependent tunnelling. It results from a structure of magnetic tunnel junction which is two ferromagnets separated by a thin insulating material which electrons can tunnel through. This contrasts with GMR (51) where the spacer layer is a non-magnetic metal such as Ruthenium, leading to spin dependent scattering in the bulk material.

The TMR effect can be expressed as a ratio of resistances between the two magnetic states:

$$TMR = \frac{R_{AP} - R_P}{R_P} \tag{3.15}$$

Where R_{AP} is the high resistance state of the antiparallel alignment between the two ferromagnets, and R_P is the low resistance state of the parallel alignment.

The change in the resistance is governed by the density of states at the Fermi level. In the parallel state, high density of states can easily tunnel as seen in Figure 3.1. In the parallel state the majority of spins in the first ferromagnet find a high density of states in the second ferromagnet, and minority states in the first ferromagnet find available minority states in the second ferromagnet. This leads

to a high tunnelling probability and low resistance. In contrast, in the antiparallel state, the majority of states in the first ferromagnet align with the minority states in the second ferromagnet. This asymmetry at the Fermi level reduces tunnelling probability, resulting in higher resistance.

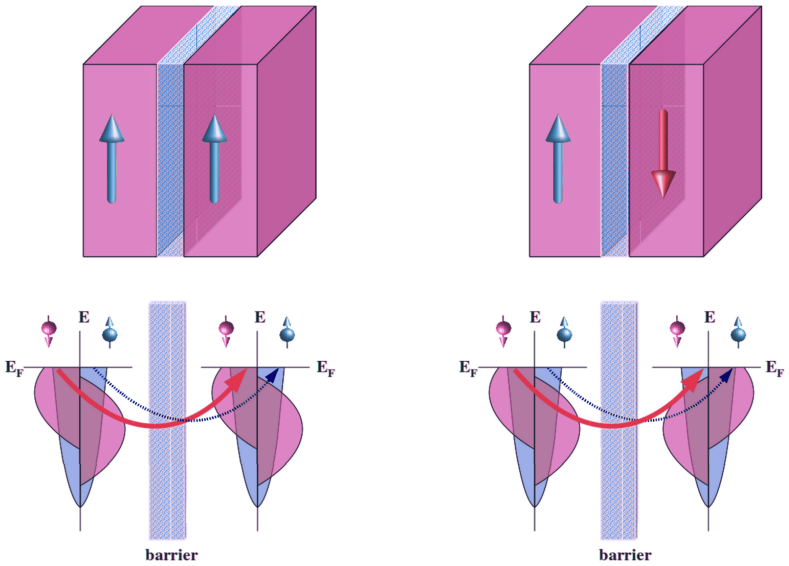


Figure 3.1: Graph of spin dependent tunnelling adapted from Phanwadee (3) . The graph shows down-spin tunnelling through the MTJ barrier to down-spin states, and up-spin tunnelling to up-spin states.

A simple model of TMR is Jullière's model which is based on two assumptions, firstly, that the spin of the electron is conserved in tunnelling, therefore that the spin-up and spin-down particles are two independent processes, based on Mott's two channel model and seen in Figure 3.1. Secondly, the model also includes corrections for spin-flip to account for spin orbit coupling and disorder from thermal spin disorder.

$$TMR_{\text{Jullière}} = \frac{2P_1P_2}{1 - P_1P_2} \tag{3.16}$$

Where P_1 and P_2 are the intrinsic spin polarizations (defined by Equation 3.2) of the two ferromagnetic electrodes. This model assumes elastic, spin-conserving tunnelling, where spin polarisation is directly proportional to the spin polarisation of the density of states at the Fermi level. While useful for describing dependence on electrode properties, this equation does not account for electronic orbital symmetries at boundaries.

Early experiments on TMR used an amorphous Al_2O_3 barrier separating ferromagnetic electrodes, achieving a TMR ratio of 70% at room temperature (52). As the tunnelling barrier is amorphous, the tunnelling is considered incoherent. In incoherent tunnelling as seen on the right in Figure 3.2, the lack of crystal symmetry allows electronic wavefunctions with various orbital symmetries to couple with the decaying electron states in the amorphous barrier. This reduces the efficiency of the spin filtering and lowers the net polarisation of the current. Later experiments used crystalline MgO as the tunnel barrier, dramatically increasing the TMR ratio, and achieving giant TMR.

The highest TMR ratios have been achieved using a crystalline MgO barrier with CoFeB electrodes. There were theoretical predictions in 2001 that an epitaxial Fe/MgO/Fe (001) could reach TMR ratios of 1000% (53). Although 1000% was a theoretical ceiling, a demonstration in 2004 by Yuasa et al. and Parkin et al showed that TMR could exceed 100% at room temperature(54; 55). Modern CoFeB/MgO/CoFeB multilayers have achieved TMR ratios of 600% at RT. This was possible as the crystalline MgO barrier acts as a symmetry filter, ensuring spin dependent tunnelling. Among the decaying electron states in MgO(001) band gap, the Δ_1 state has the slowest decay length. The MgO barrier favours the tunnelling of highly polarised Δ_1 states while damping Δ_2 and Δ_5 states. Therefore, while

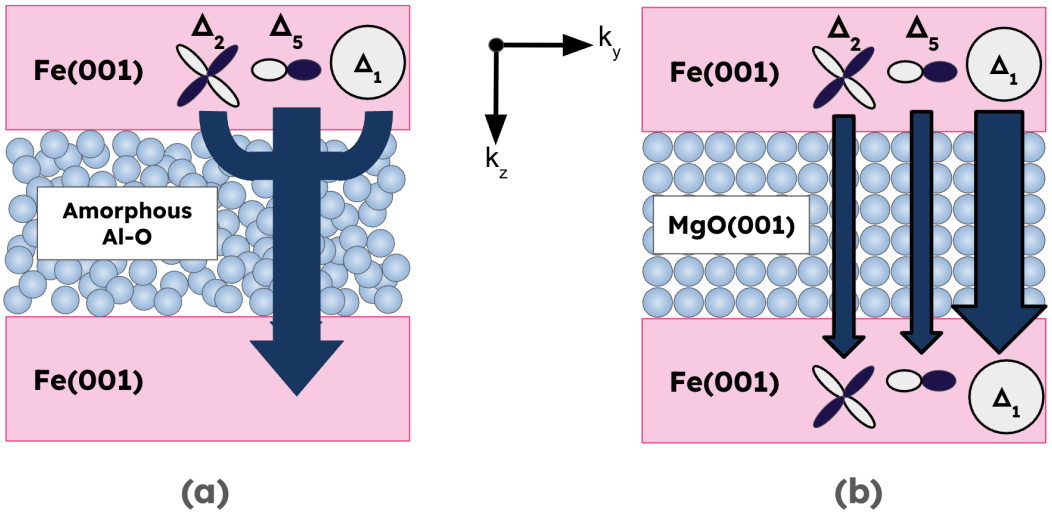


Figure 3.2: Schematic of electron tunnelling through an amorphous AlO (a) barrier versus the coherent tunnelling that occurs in Fe(001), MgO(001) (b). Adapted from Shinji Yuasa(4)

the ferromagnets are in parallel alignment the tunnelling channel Δ_1 is maximised. However, in the antiparallel alignment this tunnelling channel is non-existent.

Free-electron plane wave models fail as they ignore band-structure symmetry matching. They assume a plane wave when tunnelling through the MgO, however, there are some orbital symmetries and the Fe Δ_1 Bloch states couple with MgO Δ_1 tunnelling-states. The MgO has several tunnelling states in the band gap where Δ_1 states are associated with the s, p_z, and d_{z^2} orbitals, Δ_2 is associated with $d_{x^2-y^2}$ orbitals, Δ_2' is associated with d_{xy} orbitals, and Δ_5 is associated with a mixture of p_x, p_y, d_{yz}, and d_{zx} orbitals.

3.1.5 Spin Transfer Torque

Spin transfer torque was formalized in 1996 by two independent authors, Berger and Slonczewski (56; 57). Spin transfer torque is the transfer of spin angular momentum from a spin-polarized current into the local magnetic moments of a

ferromagnet, and occurs as a consequence of the conservation of angular momentum (58).

Berger's model focussed on magnetic instability, suggesting that when the chemical potential splitting, or spin accumulation, of spin-up and spin-down electrons exceeds the energy of the spin-wave gap, spin waves form.

Slonczewski's model was based on the conservation of spin angular momentum. He proposed that when a spin-polarised current flows into a misaligned ferromagnet, the conduction electrons attempt to align with the ferromagnets magnetisation via the s - d interaction. This reorientation of the electron spins transfers spin angular momentum reorientating the ferromagnet.

The combined Berger-Slonczewski model describes that a large current applied to an MRAM stack can either produce spin waves or cause magnetisation rotation. Figure 3.3 (a) shows the evolution of a spin polarised current travelling through the pinned layer, through the MgO and FL1 layers, and switching direction. In Figure 3.3 (b) the electrons visible show the absence of spin precession within the MgO layer due to the FeCoB pinned and FL1 layers being aligned in parallel.

In 1997, Zhang et al. (59) developed the Zhang-Levy-Fert (ZLF) model which describes the Spin Transfer Torque ($\boldsymbol{\tau}_{STT}$) as an interaction between the local magnetisation ($\boldsymbol{M}$) and the non-equilibrium spin accumulation ($\delta\boldsymbol{m}$).

This model describes a spin-polarised current building up through a ferromagnet until the spin accumulation reaches a steady-state in approximately 1×10^{-12}s. This process is governed by the spin diffusion length (λ_{sdl}), typically tens of nanometres in magnetic materials, and the exchange length (λ_J), which relates to the transfer of angular momentum between itinerant electron spins and local magnetic moments via the s - d exchange interaction, typically only a few nanome-

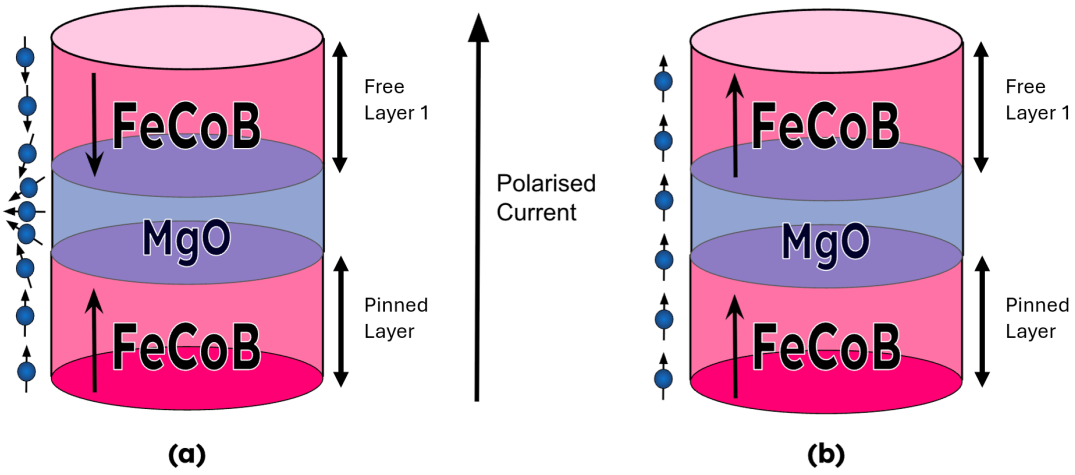


Figure 3.3: Diagram of STT in magnetic multilayers composed of a pinned bottom layer, the non-magnetic MgO layer, and the free layer 2, where ferromagnets in (a) are antiparallel, and (b) are parallel.

tres.

$$\boldsymbol{\tau}_{STT} = \frac{J_{sd}}{\hbar}(\boldsymbol{M} \times \delta\boldsymbol{m}) \tag{3.17}$$

where $\boldsymbol{\tau}_{STT}$ is the external torque density exerted on the local magnetisation unit vector $\boldsymbol{M}$, J_{sd} is the s - d exchange coupling energy, the strength of the interaction between s band and d band interactions, and $\delta\boldsymbol{m}$ is the non-equilibrium spin accumulation vector.

Due to the cross product in equation 3.17, the torque is only dependent on the transverse component of $\delta\boldsymbol{m}$ ($\delta\boldsymbol{m}_{\perp}$). Since the $J_{sd}/\hbar$ is a constant in a homogenous material, the torque is proportional to the cross product of the magnetisation and the transverse spin accumulation:

$$\boldsymbol{\tau}_{STT} \propto \boldsymbol{M} \times \delta\boldsymbol{m}_{\perp} \tag{3.18}$$

Physically, if the spin accumulation is parallel to the magnetisation $\boldsymbol{M}$, the magnetic moments are already aligned and no torque is exerted. If the accumulated spins are misaligned, the s - d interaction induces a precession to align the spins with the local $\boldsymbol{M}$, transferring the angular momentum and generating the torque.

The magnetisation reversal driven by spin transfer relaxation torque can be described by the Landau–Lifshitz–Gilbert (LLG) equation:

$$\frac{d\boldsymbol{M}}{dt} = -\gamma \boldsymbol{M} \times \boldsymbol{H}_{eff} + \frac{\alpha}{|\boldsymbol{M}|}\left(\boldsymbol{M} \times \frac{d\boldsymbol{M}}{dt}\right) + \boldsymbol{\tau}_{STT} \tag{3.19}$$

where $-\gamma \boldsymbol{M} \times \boldsymbol{H}_{eff}$ is the precession term describing the movement of the magnetisation vector $\boldsymbol{M}$ around the effective magnetic field ($\boldsymbol{H}_{eff}$), $\frac{\alpha}{|\boldsymbol{M}|}\left(\boldsymbol{M} \times \frac{d\boldsymbol{M}}{dt}\right)$ is the damping term, where α is the Gilbert damping parameter controlling energy dissipation, and $\boldsymbol{\tau}_{STT}$ is the external torque applied by the spin current which drives magnetisation switching.

The torque term is composed of two terms, the damping-like torque ($\boldsymbol{T}_{\parallel}$) and the field-like torque ($\boldsymbol{T}_{\perp}$) which are derived from the boundary conditions of spin transport.

$$\boldsymbol{\tau}_{STT} = \boldsymbol{T}_{\parallel} + \boldsymbol{T}_{\perp} = a_J(\boldsymbol{M} \times (\boldsymbol{M} \times \boldsymbol{P})) + (b_J(\boldsymbol{M} \times \boldsymbol{P})) \tag{3.20}$$

where $\boldsymbol{T}_{\parallel}$ is the damping-like torque parallel to $\boldsymbol{M} \times (\boldsymbol{M} \times \boldsymbol{P})$, $\boldsymbol{T}_{\perp}$ is the field-like torque parallel to $\boldsymbol{M} \times \boldsymbol{P}$, and a_J and b_J are coefficients of the applied current density (J_e), the spin polarisation ($\boldsymbol{P}$), and spin mixing conductance ($G^{\uparrow\downarrow}$). While both $\boldsymbol{T}_{\parallel}$ and $\boldsymbol{T}_{\perp}$ can be significant, $\boldsymbol{T}_{\parallel}$ is the primary driver for magnetisation reversal when the current exceeds a critical value.

Device performance is determined by the critical current (J_c), the minimum

current needed for deterministic magnetisation reversal is found by (60):

$$J_c \propto \frac{\alpha e |M_s| V}{\hbar P} \left(H_k \pm \frac{1}{2} H_d \right) \tag{3.21}$$

where α is the Gilbert damping parameter, $|M_s|V$ is the total magnetic moment proportional to the energy barrier, e is the elementary charge, P is the effective spin polarisation of the tunnelling current, H_k is the anisotropy field, and H_d is the demagnetisation field.

The $\pm$ sign describes the two switching directions. The plus sign $(+)$ is for switching from parallel to antiparallel alignment ($J_c^{P \to AP}$), which requires a higher critical current. The minus sign $(-)$ is for switching from antiparallel to parallel ($J_c^{AP \to P}$), where the exchange interaction aids the switching process, resulting in a lower critical current.

4 Atomistic Modelling

The development of physical models of the MRAM system is critical to bridging the theory with fundamental mechanics. Following the theory established in Chapter 3, this chapter's goal is to find the specific modelling approach used to simulate the SAF MRAM by adapting the continuous nature of STT equations into an atomistic framework for the atomistic simulation package, VAMPIRE. This chapter starts with outlining the historical development of spin models, starting with the basic Ising model before outlining the development of Heisenberg exchange, and the Landau-Lifshitz-Gilbert equation. The subsequent sections detail the core methods used in this thesis. The Heisenberg Hamiltonian is used to define the total magnetic energy of the system, Monte Carlo methods are used to establish the thermodynamic properties, and the LLG equation is adapted to model the MRAM device under current injection.

4.1 Introduction to Spin Models

In 1925, Ernst Ising first proposed an atomistic model which described magnetic behaviour by assuming a lattice structure where only nearest neighbours interact and all spins are restricted to up or down (61). While the model was later adapted to describing alloys, mixtures and certain magnets, its original one-dimensional form was limited because it could not describe long-range order or a phase transi-

tion at any finite temperature.

The Ising model was developed and built upon by incorporating the Heisenberg exchange, where a vector representation of spins is included. After studying the exchange interaction in Hydrogen molecules in 1926, Heisenberg proposed the his model in 1928, which allowed atomic spins to vary as a continuous vector in 3D space.

The Landau-Lifshitz equation was first proposed in 1935 to explain the precession of magnetisation. However, its original form only worked well in a small damping regime. A more complete model was formulated when Gilbert introduced an equivalent but mathematically superior damping parameter leading to the Landau-Lifshitz-Gilbert (LLG) equation derived in 1955 though a Lagrangian approach.

4.2 Heisenberg Hamiltonian

The Generalised Heisenberg Hamiltonian is a quantum-mechanically derived model that describes the total energy $\mathscr{H}$ of a system of interacting atomic magnetic moments. It forms the basis for many models including atomistic and continuous micromagnetic simulations.

The total Hamiltonian H is typically expressed as a sum of four key energy contributions:

$$\mathscr{H} = \mathscr{H}_{exc} + \mathscr{H}_{ani} + \mathscr{H}_{app} + \mathscr{H}_{dip} \tag{4.1}$$

where $\mathscr{H}_{exc}$ is the exchange energy between spins, $\mathscr{H}_{ani}$ is the magnetic anisotropy per atom, $\mathscr{H}_{app}$ is the externally applied magnetic field and local magnetic moment, and $\mathscr{H}_{dip}$ is the magnetostatic dipolar interactions.

Exchange Energy

The Exchange Interaction is the dominant short-range interaction in magnetic materials, arising from the Pauli exclusion principle and electrostatic interactions (62). It dictates the relative orientation of neighbouring atomic magnetic moments, which is responsible for magnetic ordering such as ferromagnetism, antiferromagnetism and ferrimagnetism as outlined in Chapter 2.

The exchange energy is typically modelled using the Heisenberg Hamiltonian term:

$$\mathscr{H}_{exc} = -\sum_{i<j} J_{ij} \boldsymbol{S}_i \cdot \boldsymbol{S}_j \tag{4.2}$$

Where J_{ij} is the exchange integral between atomic sites i and j, and $\boldsymbol{S_i}$ and $\boldsymbol{S_j}$ are the spin operators at sites i and j respectively. The magnetic moment $\boldsymbol{\mu}_i \propto \boldsymbol{S}_i$. If $J_{ij} > 0$, the interaction is ferromagnetic (spins align parallel, ($\boldsymbol{S}_i \parallel \boldsymbol{S}_j$). If $J_{ij} < 0$, the interaction is antiferromagnetic (spins align antiparallel, ($\boldsymbol{S}_i \parallel -\boldsymbol{S}_j$).

The exchange energy is the dominant energy interaction over short ranges, and its magnitude is several orders larger ($\sim 1 \times 10^{-21}$ J/link) than the anisotropy and dipolar energies ($\sim 1 \times 10^{-23}$ J/link). Due to the very short-range nature of the exchange interaction the J_{ij} can be calculated by only using the nearest neighbours (NN) around the atom while maintaining accuracy for most of the cases. In highly precise calculations, the next nearest neighbour may also be used in simulations, however that is rarely necessary. This approximation decreases the calculation time from $\mathcal{O}(N^2)$ to $\mathcal{O}(N)$ making large-scale simulations feasible (63).

To find the values used in J_{ij}, there are three methods: First principle (ab initio) calculations, experimental fitting, and high precision experimental data. In ab initio calculations, Density Functional Theory (DFT) is viewed as the most fundamental and accurate approach that requires no experimental data except the

crystal structure and chemical composition (64). DFT is used to solve the electron structure of the material to yield the exchange. This is done through calculating the exchange that results between two atomic sites (i and j) when slightly twisting one atom in relation to another, and calculating the total energy of the system for several non-collinear spin arrangements (65). The advantage that DFT provides is that it can calculate the nearest neighbours as well as long-range interactions, where the found exchange is a set of J_{ij} values such as those seen in equation 4.5.

In experimental fitting, the J_{ij} values can be calculated by fitting to experimental data of the known Curie temperature (T_C) using mean field theory:

$$k_B T_C = \frac{2}{3} z J S(S+1) \tag{4.3}$$

where k_B is the Boltzmann constant, z is the number of nearest neighbours, J is the exchange, and S is the spin quantum number. Though this is dependent on the exchange being an isotropic exchange tensor, and is assumed to be only nearest neighbour interactions. This method inherently overestimates the strength of the interaction as it does not take into account the spin-spin correlation and thermal fluctuations. Therefore, the J_{ij} is an effective parameter that must be adjusted in simulations to yield the correct T_C.

In high precision experimental data, the exchange energy is found through experiments such as inelastic neutron scattering, which is used to directly measure the spin wave dispersion relation, a property directly affected by exchange stiffness, which can then be used to find the exchange energy (66). A spin wave is a collective excitation which precesses across a lattice. This can be then used to calculate the exchange stiffness and energy. By fitting the theoretical spin wave to the experimental data, the J_{ij} values for nearest neighbours and next nearest

neighbours can be determined. The measured dispersion relation ($E(\boldsymbol{k})$) this can be approximated in the long-wavelength limit as:

$$E(\boldsymbol{k}) \approx 2JSa^2\boldsymbol{k}^2 \tag{4.4}$$

This method is high-fidelity and rigorous, providing an experimental confirmation to DFT methods.

Anisotropic and Tensor Exchange

The simplest case of equation 4.2 is the isotropic exchange, where the interaction is only based on the relative orientation between sites i and j and, consequently, J_{ij} is a scalar. When dealing with more complicated systems, such as the Dzyaloshinskii–Moriya interaction and two-ion anisotropic exchange interactions, J_{ij} must be expressed as a tensor:

$$J_{ij} = \begin{bmatrix} J_{xx} & J_{xy} & J_{xz} \\ J_{yx} & J_{yy} & J_{yz} \\ J_{zx} & J_{zy} & J_{zz} \end{bmatrix} \tag{4.5}$$

The two-ion anisotropy case, or pseudo-dipolar interaction, is represented by the symmetric component of the exchange tensor, meaning J_{ij} is symmetric, $J_{ij} = J_{ji}$. In the simplest uniaxial case, when aligned with the principal crystal axes, the off-diagonal components of the tensor are zero, while the diagonal components are non-zero but unequal ($J_{xx} = J_{yy} \neq J_{zz}$). This dependence on the crystal axis differentiates it from the isotropic exchange. The Dzyaloshinskii-Moriya interaction is instead represented by the antisymmetric component, which when strong enough, is responsible for non-collinear spin configurations.

Therefore, equation 4.2 in the tensorial case can be rewritten in quadratic form

as:

$$\mathscr{H}_{exc}^{M} = -\sum_{i \neq j} \begin{bmatrix} S_x^i & S_y^i & S_z^i \end{bmatrix} \begin{bmatrix} J_{xx} & J_{xy} & J_{xz} \\ J_{yx} & J_{yy} & J_{yz} \\ J_{zx} & J_{zy} & J_{zz} \end{bmatrix} \begin{bmatrix} S_x^j \\ S_y^j \\ S_z^j \end{bmatrix} \tag{4.6}$$

4.2.1 Magnetic Anisotropy

The second key term in the Heisenberg Hamiltonian seen in Equation 4.1 is the magnetic anisotropy. This energy term is largely responsible for the thermal stability of a magnetic material and describes the magnetic moment's preferred alignment along a specific spatial direction known as the easy axis. The easy axis corresponds to the direction of minimum energy, while the hard axis is the direction requiring maximum energy to magnetise.

The microscopic origin of magnetic anisotropy is the spin-orbit coupling (SOC), which links the electron's spin angular momentum to its orbital angular momentum, allowing the magnetic moment to interact with the local crystal environment; the crystal field. The interaction is the strongest for electrons with high SOC strength, typically 3d or 4f electrons depending on the material.

Uniaxial Anisotropy

The simplest form is uniaxial anisotropy, where magnetic moments prefer to align along a single axis ($\boldsymbol{e}$). The energy term per atom is:

$$\mathscr{H}_{ani}^{uni} = -k_u(\boldsymbol{S_i} \cdot \boldsymbol{e})^2 \tag{4.7}$$

where k_u is the anisotropy per atom, and $\boldsymbol{e}$ is the unit vector of the easy axis.

Crystal Anisotropy (Cubic)

In materials with cubic crystal structure, such as Iron and Nickel, the resulting cubic anisotropy can be written as:

$$\mathcal{H}_{ani}^{cub} = -\frac{k_c}{2}\sum_i (S_x^4 + S_y^4 + S_z^4) \tag{4.8}$$

where k_c is the cubic anisotropy, and S_x, S_y, S_z, are the x, y, and z component of the spin moment.

Shape and Interfacial Anisotropy

Shape anisotropy is a non-intrinsic form arising from long-range dipole interactions within magnetic materials, with an easy axis preference favouring magnetisation along the structure's longest axis. This minimises stray fields, promotes flux closure, and reduces the demagnetising field. In contrast, perpendicular magnetic anisotropy (PMA) which overcomes shape anisotropy in thin films, with an easy axis preference perpendicular to the film surface, results from two key effects: magnetocrystalline anisotropy and interfacial anisotropy.

For macroscopic objects with a homogenous magnetisation the shape anisotropy can be described through the demagnetisation tensor ($\bar{\bar{N}}$) which depends solely on the geometry of the object. The demagnetising factor can be written as:

$$\boldsymbol{H}_d = -\bar{\bar{\boldsymbol{N}}} \cdot \boldsymbol{M} \tag{4.9}$$

where $\boldsymbol{H}_d$ is the demagnetisation field, and $\boldsymbol{M}$ is the magnetisation. In an infinite thin film the demagnetisation tensor can be approximated such that perpendicular to the plane $N_z \approx 1$, and parallel to the plane $N_x = N_y \approx 0$. This leads to

the demagnetisation field preferring in-plane magnetisation in conventional disc-shaped MRAM design, and a cost of $\propto M^2$ when magnetisation attempts to align perpendicularly (67).

Interfacial anisotropy (iPMA) is an intrinsic property, and is the most significant source of PMA in thin films, and required for high-density MRAM. iPMA arises from the broken crystal symmetry at the interface between different materials, like CoFeB/MgO (68), causes strong electron orbital hybridisation, creating a large energy difference between in-plane and out of plane magnetisation. At the interface the crystal field quenches the orbital moment of the electrons. Due to the reduced symmetry the in-plane orbitals are quenched while the out-of-plane orbitals are less affected. This leads to an anisotropy of the orbital moment, where the easy axis is in the direction of the largest orbital moment (69). In the Heisenberg hamiltonian this iPMA manifests as an anisotropic exchange tensor $\bar{\bar{\boldsymbol{A}}}$, where the diagonal elements are unequal, creating an energetic preference perpendicular to the interface.

The interfacial anisotropy constant tends to be large for the interface between CoFeB/MgO, with a significant temperature dependence. The thermal stability of the device depends on a stable iPMA creating a high energy barriers to ensure non-volatile data retention in MRAM devices (70).

4.2.2 Applied Fields ($\mathscr{H}_{app}$)

The third term $\mathcal{H}_{app}$, represents the interactions which result from an external magnetic field interacting with local spins, causing the spins to favour alignment with that field. The energy from this interaction is occasionally called the Zeeman energy and can be written as:

$$\mathscr{H}_{app} = -\sum_i \mu_s \boldsymbol{S}_i \cdot \boldsymbol{H}_{app} \tag{4.10}$$

where μ_s is the atomic magnetic moment, and $\boldsymbol{H}$ is the applied field in Tesla.

4.2.3 Dipolar Energy ($\mathscr{H}_{dip}$)

The dipolar energy, otherwise known as the demagnetisation field or magnetostatic energy, results from the long-range magnetic dipole-dipole interactions between all spins in the material. The macroscopic effect of the dipole field is shape anisotropy, where the geometric dependence leads to an easy axis forming where the bulk material's energy is minimised. The dipolar interaction attempts to minimise stray fields outside the material, leading to the formation of magnetic domains where magnetisation is typically opposite in neighbouring regions.

Continuum Formulation

In the continuum (micromagnetic) approach, the dipolar energy is expressed as the energy density of the magnetisation, $\boldsymbol{M}$, interacting with the demagnetising field, $\boldsymbol{H}_d$:

$$\mathscr{H}_{dip} = -\frac{1}{2}\int \boldsymbol{M} \cdot \boldsymbol{H}_d dV \tag{4.11}$$

Atomistic Formulation

On the atomistic scale, the interaction energy between pairs of magnetic dipoles is summed over all distinct pairs of spins, and its magnitude decays rapidly with distance, $1/r_{ij}^3$:

$$\mathscr{H}_{\text{dip}} = -\frac{\mu_0}{4\pi}\sum_{i\neq j}\frac{1}{r_{ij}^3}\left[3(\boldsymbol{\mu}_i \cdot \hat{\boldsymbol{e}}_{ij})(\hat{\boldsymbol{e}}_{ij} \cdot \boldsymbol{\mu}_j) - (\boldsymbol{\mu}_i \cdot \boldsymbol{\mu}_j)\right] \tag{4.12}$$

where r_{ij} is the distance between magnetic moments $\boldsymbol{\mu}_i$ and $\boldsymbol{\mu}_j$, $\hat{\boldsymbol{e}}_{ij}$ is the unit vector pointing from i to j, and μ_0 is the permeability of free space.

$$\mathscr{H}_{dip} = -\frac{\mu_s \mu_0}{4\pi a^3} \sum_{i \neq j} \frac{3(\boldsymbol{S}_i \cdot \hat{\boldsymbol{e}}_{ij})(\hat{\boldsymbol{e}}_{ij} \cdot \boldsymbol{S}_j) - (\boldsymbol{S}_i \cdot \boldsymbol{S}_j)}{r_{ij}^3} \tag{4.13}$$

where r_{ij} is the distance between spins i and j, $\hat{\boldsymbol{e}}_{ij}$ is the unit vector, and a is the lattice parameter.

Computational Note

While the dipolar interaction is generally much weaker than the exchange interaction, it is long-range and therefore computationally expensive as the computation of N spins requires $\sim N^2$ calculations. This would require a prohibitive computation time and memory to store the full dipolar matrix. Consequently, it is often ignored in atomistic simulation of very short timescales or high temperatures. When necessary, micro-magnetic simulations often approximate this term by dividing the material into macrocells with uniform magnetisation, treating each cell as a point dipole. This division and approximation is shown in Figure 4.1 where the large magnetic system is divided into macrocells of uniform magnetisation.

In the bare macrocell approach employed in the atomistic simulation package VAMPIRE, the system is discretised into smaller cells in a micromagnetic-like approach (63). The bare macrospin approach relies on the assumption that if the macrospin is significantly smaller than the magnetic domain, the magnetisation within the cell can be treated as uniform, and therefore each macrocell can be treated as having a single magnetic dipole at its centre. The macro-moment ($\boldsymbol{m}_{mc}$) can be calculated:

$$\boldsymbol{m}_{mc} = \sum_{i}^{n} \mu_i^s S_i \tag{4.14}$$

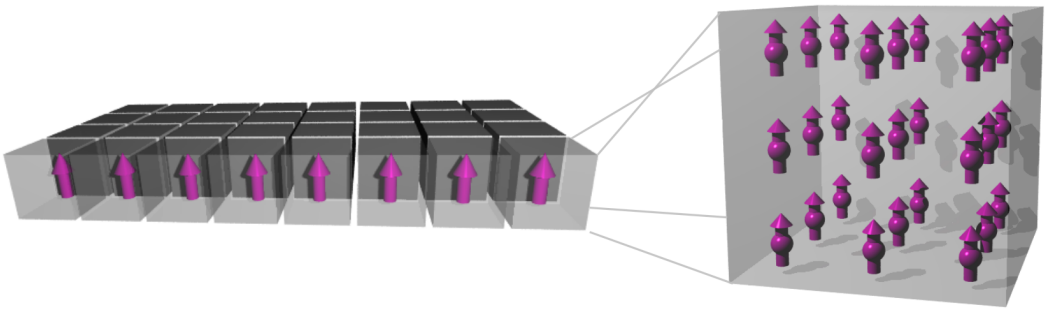


Figure 4.1: Recoloured schematic representation by Andrea Meo (5) of the division of a large magnetic system into discrete macrocells (left) where each macrocell has uniform magnetisation (right).

where n is the number of spins within the macrocell, μ_i^s is the local atomic magnetic moment, and S_i is the reduced spin vector. The position of the dipole magnetic moment ($\boldsymbol{p}_{mc}$) within the macrocell is then corrected by weighting the atomic coordinates by the magnetic moments, moving towards the stronger magnetic moments, this increases the accuracy of the calculation, though prevents numerical shortcuts such as Fast Fourier transforms.

Therefore, the total dipolar field within each macrocell ($B_p^{\text{dip, mc}}$) is given by the two terms:

$$B_p^{\text{dip, mc}} = \frac{1}{4\pi}\left[\sum_{p\neq q}\frac{3(\boldsymbol{m}_q^{mc}\cdot\hat{\boldsymbol{r}}_{pq})\hat{\boldsymbol{r}}_{pq}-\boldsymbol{m}_q^{mc}}{\boldsymbol{r}_{pq}^3}\right]+\frac{2}{3}\frac{\boldsymbol{m}_p^{mc}}{V_p^{mc}} \tag{4.15}$$

where the first term describes the long-range, inter-cell interaction where the summation represents the interaction between macrocell p and surrounding macrocells, and can be rewritten as a sum of the product between the dipole tensor seen in 4.16 and m_q^{mc}. The dipolar tensor is defined by the geometry of the system:

The second term is the Maxwellian internal field of a sphere. The Maxwellian internal field arises from treating the magnetic material as a source of the field it-

self, therefore, ensuring the agreement with the continuous description of magnetic fields(5).

$$\bar{\bar{\boldsymbol{D}}} = \frac{1}{4\pi r^5} \begin{pmatrix} 3r_x^2 - r^2 & 3r_x r_y & 3r_x r_z \\ 3r_y r_x & 3r_y^2 - r^2 & 3r_y r_z \\ 3r_z r_x & 3r_z r_y & 3r_z^2 - r^2 \end{pmatrix} \tag{4.16}$$

The macrocell approach only has accuracy within 10% of the real lattice dipolar energy ($E_{dip}^{mc} \approx E_{dip}$) (71). The total dipolar energy (E_{dip}^{mc}) calculated for the bare macrocell lattice is:

$$E_{dip}^{mc} = -\frac{1}{2} \sum_{p \neq q}^{N_p} \sum_{q}^{N_p} \boldsymbol{m}_q \cdot \bar{\bar{\boldsymbol{D}}}_{pq} \cdot \boldsymbol{m}_p \tag{4.17}$$

This error is a known limitation of the macrocell model, which led to the development of more accurate methods such as the Inter- and Intra-Macrocell Point Dipole Model.

4.3 Monte Carlo Methods

The Monte Carlo method is used to approximate answers to analytically intractable problems (72). It is founded on the Law of Large Numbers which states that the statistical average of many samples converges to the true expectation value. The expected value $\langle f(x) \rangle$ of a function $f(x)$ over a probability distribution $p(x)$ is approximated by the sample mean:

$$\langle f(x) \rangle \approx \frac{1}{N} \sum_{i=1}^{N} f(x_i) \tag{4.18}$$

where x_i are random samples drawn from $p(x)$, and N is the number of samples taken, when $N \to \infty$ the estimated average approaches the true value.

In atomistic simulations the Monte Carlo method is useful in finding time-independent equilibrium properties (average energy, magnetisation). It relies on pseudo-random number generation, as computer algorithms cannot produce truly random numbers; consequently, it does not yield real-time dynamic properties.

Ergodicity and Reversibility

Markov chain Monte Carlo (MCMC) simulations are reliant on ergodicity and reversibility (73). Ergodicity is the property that a Markov chain, after running for an infinite amount of time, has the possibility to visit every state in the target space. This is necessary to satisfy the Ergodic Theorem, the Law of Large Numbers for Markov chains, where the time average of any function of the system's state converges to the true ensemble average(74). In the case where MCMCs do not follow ergodicity, the simulation results will be biased. A Markov chain is reversible with respect to its stationary distribution π if it fulfils the detailed balance equation (DBE) seen in equation 4.19

$$\pi(i)P(j|i) = \pi(j)P(i|j) \tag{4.19}$$

where $\pi(i)$ and $\pi(j)$ are the stationary probabilities of states i and j, respectively, $P(j|i)$ is the forward transition probability from state i to state j, and $P(i|j)$ is the reverse transition probability from state j to state i.

While most MCMCs are reversible, there are cases where MCMCs achieve convergence to the correct stationary distribution without being reversible (75). Non-reversible MCMCs, such as hybrid Monte Carlo approaches, have the poten-

tial to be faster than reversible MCMCs by avoiding random walk behaviour.

4.3.1 Markov Chain Monte Carlo (MCMC)

The Markov Chain Monte Carlo (MCMC) simulations use Markov chains, a stochastic process whose next state is dependent only on the current state, not on past states (76). The goal of MCMC is to construct a Markov chain whose long-term stationary distribution is the target probability distribution, $\pi(\boldsymbol{S})$. In a classical system, the target distribution is typically the Boltzmann distribution:

$$\pi(\boldsymbol{S}) \propto e^{-E(\boldsymbol{S})/(k_B T)} \tag{4.20}$$

where $\pi(\boldsymbol{S})$ is the probability of configuration $\boldsymbol{S}$, $E(\boldsymbol{S})$ is the energy of configuration $\boldsymbol{S}$, k_B is the Boltzmann constant, and T is the thermodynamic temperature.

For the Metropolis algorithm (a type of MCMC with symmetric trial moves), the transition from the current state $\mathbf{S}$ to a trial state $\mathbf{S}'$ is accepted based on the change in energy, ΔE, defined as:

$$\Delta E = E(\boldsymbol{S}') - E(\boldsymbol{S}) \tag{4.21}$$

The acceptance probability, $A(\mathbf{S} \rightarrow \mathbf{S}')$, follows the Metropolis rule shown in Equation 4.22 (77), and this is repeated until the desired number of trial moves N is completed.

$$A(S \rightarrow S') = \begin{cases} 1, & \text{if } \Delta E \leq 0, \\ e^{-\Delta E/(k_B T)}, & \text{if } \Delta E > 0 \end{cases} \tag{4.22}$$

where $e^{-\Delta E/(k_B T)}$ is the ratio of Boltzmann factors, and $A(\mathbf{S} \rightarrow \mathbf{S}')$ is the accep-

tance probability of state **S** becoming **S′**.

The Metropolis acceptance rule shown in Equation 4.22 is only valid when the trial move is symmetric, such that the proposal probability $Q(S|S') = Q(S'|S)$.

Monte Carlo simulations rely on trial moves to generate new spin configurations ($\boldsymbol{S}'$) from the current spin state ($\boldsymbol{S}$), which are then evaluated using the acceptance probability ($A(\boldsymbol{S}' \rightarrow \boldsymbol{S})$). The acceptance probability affects how effective the Markov-chain is when moving through the target space. Trial moves can be local and non-local (78).

An example of a local trial move is the spin-flip trial move, where a single spin moves to a random point on the unit sphere, as the local change only affects the spin's nearest neighbours only local energy changes need to be calculated. Though, as this change is local only long-range correlations over lattices propagate slowly, this is the main cause of critical slowing down.

Non-local trial moves such as the Wolff Cluster Algorithm, update groups of spins at the same time (79). This prevents critical slowing, however, it loses efficiency or cannot incorporate complex dynamics such as the dipolar interaction in large systems (80).

4.3.2 Hinzke and Nowak (HN) Method

Critical slowing down (CSD) is a phenomenon that causes inefficiencies in standard MCMC simulations near phase boundaries, where the simulation explores highly correlated configurations. In a Metropolis algorithm, for example, changes are local and therefore only the nearest neighbours are updated. This leads to CSD because the propagation of long-range correlations occurs slowly, resulting in a divergence of autocorrelation time (τ_{corr}). The HN method overcomes CSD by combining three different trial moves: a Spin flip move (local), a Gaussian move

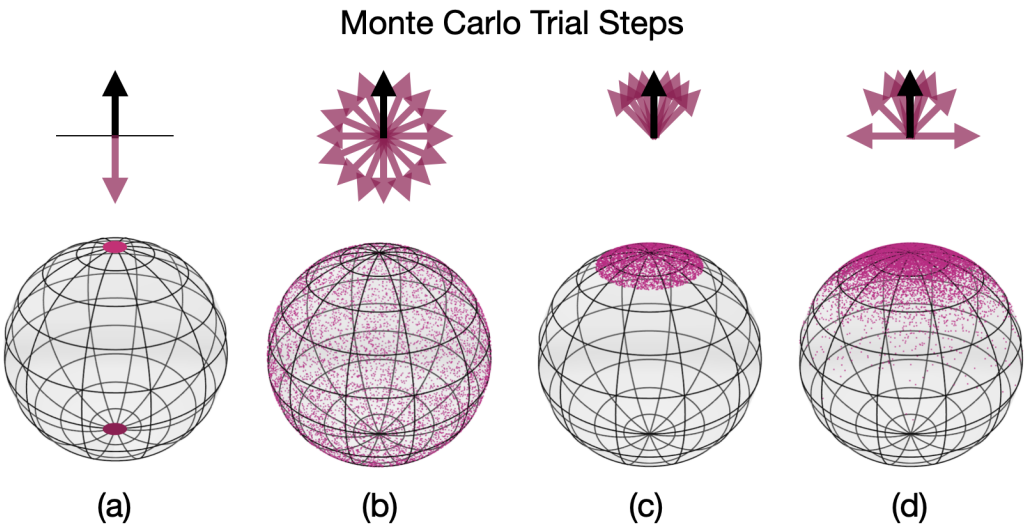


Figure 4.2: Monte Carlo trial steps (a) is the spin flip, (b) is random, (c) is the small step, (d) is Gaussian.

(non-local), and a Random move (global).

The Gaussian and Random moves in the HN method are non-symmetric and so an acceptance criterion is employed to preserve the stationary distribution ($\pi(\boldsymbol{S})$) . The Metropolis-Hastings acceptance criterion, shown in Equation 4.23, is vital for maintaining detailed balance by correcting the non-symmetrical proposal bias and ensuring the moves are selected from the Boltzmann distribution.

$$A(\boldsymbol{S}|\boldsymbol{S'}) = \min\{1, \frac{\pi(\boldsymbol{S'})Q(\boldsymbol{S}|\boldsymbol{S'})}{\pi(\boldsymbol{S})Q(\boldsymbol{S'}|\boldsymbol{S})}\} \tag{4.23}$$

where $\pi(\boldsymbol{S})$ is the target (Boltzmann) probability of state $\boldsymbol{S}$, $Q(S'|S)$ is the probability of the transition from state S to state S', and the proposal ratio $\frac{Q(\boldsymbol{S}|\boldsymbol{S'})}{Q(\boldsymbol{S'}|\boldsymbol{S})}$ corrects for the non-symmetry of the trial move, ensuring the MCMC's stationary distribution targets the Boltzmann distribution $\pi(\boldsymbol{S})$.

The Combined Acceptance Scheme

The three trial moves: spin flip (local, symmetric, Metropolis), Gaussian (global, non-symmetric, MH), random (global, non-symmetric, MH), are chosen using a probability (P_m). In most cases, P_m is chosen to be equal ($P_m = 1/3$) for each trial move (81). The spin flip trial move allows for local relaxation and maintains high acceptance at low temperatures. In contrast, the Gaussian and random moves introduce large jumps that overcome energy barriers and prevent CSD near the critical temperature, T_C. This combination promotes global exploration and allows for "fast mixing", where the system quickly loses its "memory" of the previous state, thus decreasing the autocorrelation time (τ_{corr}) and fast equilibration near T_C.

Spin Flip Trial Move

The spin flip trial move is a fast, symmetric, local move such that:

$$\boldsymbol{S}_i' = -\boldsymbol{S}_i \quad \text{and} \quad Q(\boldsymbol{S'}|\boldsymbol{S}) = Q(\boldsymbol{S}|\boldsymbol{S'}) \tag{4.24}$$

Because this trial move is symmetric, the proposal ratio $\frac{Q(\boldsymbol{S}|\boldsymbol{S'})}{Q(\boldsymbol{S'}|\boldsymbol{S})}$ equals 1, simplifying the Metropolis Hastings acceptance criterion to the standard Metropolis acceptance rule (Eq. 4.23). This trial move is shown in Figure 4.2(a) where the final position is antiparallel to the initial position.

Gaussian Trial Move

The Gaussian trial move (non-symmetric, global update) translates the spin from $\boldsymbol{S_i}$ to $\boldsymbol{S_i'}$ using a Gaussian-distributed random vector (Γ) centred on the current spin.This trial move is represented in Figure 4.2(d) where the probability of moving to the final position from the initial position decreases the further away the final

position is from the initial position. The resulting vector is then normalised to the unit spin length:

$$\boldsymbol{S_i}' = \frac{\boldsymbol{S_i} + \sigma_g \boldsymbol{\Gamma}}{|\boldsymbol{S_i} + \sigma_g \boldsymbol{\Gamma}|} \tag{4.25}$$

where $\boldsymbol{\Gamma}$ is a random vector whose components are taken from a standard Gaussian distribution, and σ_g is the width parameter (the "Gaussian cone" width) which scales the magnitude of the perturbation, and is scaled with temperature:

$$\sigma_g = \frac{2}{25} \left(\frac{k_B T}{\mu_B} \right)^{1/5} \tag{4.26}$$

At low temperatures ($T \ll T_C$), σ_g favours small, local moves with a high acceptance rate. At high temperatures (near T_C), the σ_g prefers larger steps, where the Metropolis-Hastings criterion corrects the non-symmetrical proposal bias so the final acceptance adheres to the detailed balance condition.

Random Trial Move

The random trial move (non-symmetric, global update) translates spin $\boldsymbol{S_i}$ to $\boldsymbol{S_i}'$ chosen randomly from a uniformly at random over the unit sphere. Since the new spin orientation is completely independent of the old one, $Q(S'|S) \neq Q(S|S')$, requiring the full Metropolis-Hastings correction:

$$\boldsymbol{S}_i' = \frac{\boldsymbol{\Gamma}}{|\boldsymbol{\Gamma}|} \tag{4.27}$$

where Γ is a random vector with uniform probability over the unit sphere. This is illustrated in Figure 4.2(b), which shows the probability being equal across the sphere.

Curie Temperature

The Adaptive method developed by Alzate-Cardona *et al.* (82) is used in the software VAMPIRE to study phase transitions that happen near the Curie temperature where Standard Monte Carlo methods become inefficient due to critical slowing down. The Adaptive method uses four distinct trial moves, the spin-flip, random, small-step, and Gaussian moves. The difference between the small step and Gaussian trial move is that the small step trial move has an equal chance of moving within a space of 2θ, and Gaussian has a non-uniform chance of moving the spin orientation within a space of $2\theta \propto \sigma$ where θ is the distance from the initial spin direction ($\boldsymbol{S}$) on the unit sphere, and σ is proportional to the cone and allows for a Gaussian distribution away from $\boldsymbol{S}$.

4.4 Spin Dynamics

In the previous section, the Monte Carlo method was established as a valuable method for calculating time-independent properties such as the Curie temperature. However, it cannot simulate time-resolved dynamics. Therefore it offers no insight into time-dependant properties like hysteresis, switching current, or the writing time in MRAM devices. Simulating these time-dependant phenomena requires the use of the Landau-Lifshitz-Gilbert (LLG) equation.

The LLG equation describes the non-linear movement of magnetic moments over time in the presence of magnetic fields and damping. Equation 4.28 describes the motion of the spin moment $\boldsymbol{S}_i$ at atom or approximation site i:

$$\frac{\partial \boldsymbol{S}_i}{\partial t} = -\frac{\gamma}{(1+\lambda^2)}[\boldsymbol{S}_i \times \boldsymbol{H}^i_{eff} + \lambda \boldsymbol{S}_i \times (\boldsymbol{S}_i \times \boldsymbol{H}^i_{eff})] \tag{4.28}$$

where γ is the gyromagnetic ratio, λ is the Gilbert damping parameter with a larger λ resulting in a faster relaxation, and $\boldsymbol{H}^i_{eff}$ is the effective magnetic field acting on spin i. $\boldsymbol{H}^i_{eff}$ is the sum of various fields, including the Zeeman effect, the exchange interaction, anisotropy, and the demagnetisation field. This form of the LLG equation is only applicable to systems at 0 K. For finite temperature simulations, a stochastic term must be added.

The terms in the LLG Equation are $(\mathbf{S}_i \times \mathbf{H}^i_{eff})$ which is the Precession Term describing the precession of the magnetic spin $\mathbf{S}_i$ around the effective field $\mathbf{H}^i_{eff}$ when $\lambda = 0$, $(\lambda \mathbf{S}_i \times (\mathbf{S}_i \times \mathbf{H}^i_{\text{eff}}))$ which is the Damping Term accounting for energy dissipation and causing the magnetic moment to relax into the direction of $\mathbf{H}^i_{\text{eff}}$ while conserving the magnitude of $\mathbf{S}_i$. Physically, damping is the transfer of angular momentum and energy from the spin system to other forms of excitation, primarily magnons (spin waves) and phonons (lattice vibrations). Figure 4.3 visualises these terms.

4.4.1 Stochastic LLG Equation (sLLG)

To model spin dynamics at a finite temperature T, a stochastic thermal term, $\boldsymbol{H}_{th}$, is added to the LLG equation, a methodology known as Langevin dynamics. This term couples the spin system to a heat bath which reproduces the effects of random thermal energy from the environment.

The LLG equation with Langevin dynamics is:

$$\frac{\partial \boldsymbol{S}}{\partial t} = -\frac{\gamma}{1+\lambda^2}\left[\boldsymbol{S} \times (\boldsymbol{H}_{eff} + \boldsymbol{H}_{th}) + \lambda \boldsymbol{S} \times (\boldsymbol{S} \times (\boldsymbol{H}_{eff} + \boldsymbol{H}_{th}))\right] \tag{4.29}$$

The stochastic thermal field $\boldsymbol{H}^i_{th}$ (acting on spin $\boldsymbol{S}_i$) is an additive term introduced by Brown (1979) to describe the relaxation of ferromagnetic nanoparticles

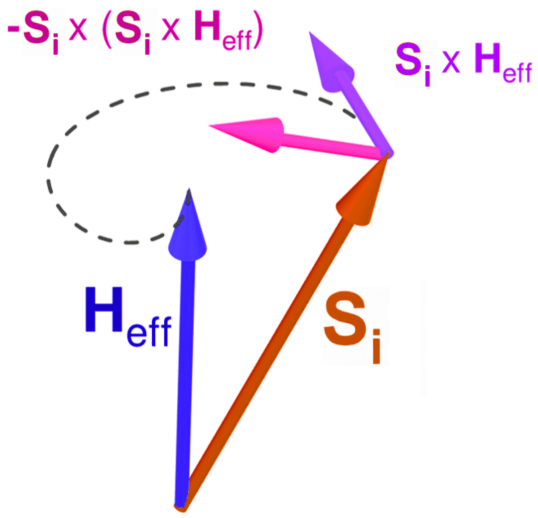


Figure 4.3: Recoloured schematic diagram, adapted from J. Fernandez-Roldan's thesis (6), illustrating the LLG dynamics. The local magnetic moment ($\boldsymbol{M}$) precesses around the effective magnetic field ($\boldsymbol{H}_{eff}$). The precession term is shown in purple, and the damping term is shown in pink.

(83):

$$\boldsymbol{H}_{th}^{i} = \boldsymbol{\Gamma}(t)\sqrt{\frac{2\lambda k_B T}{\gamma \mu_s \Delta t}} \tag{4.30}$$

where $\boldsymbol{H}_{th}$ is the stochastic thermal field, $\boldsymbol{\Gamma}(t)$ is a three-dimensional Gaussian white noise vector with zero mean, T is the temperature, λ is the Gilbert damping parameter, γ is the gyromagnetic ratio, k_B is the Boltzmann constant, and Δt is the change in time. The term $\boldsymbol{\Gamma}(t)$ this satisfies:

$$\langle \Gamma_a(t) \rangle = 0 \quad \text{and} \quad \langle \Gamma_a(t_1)\Gamma_b(t_2) \rangle = \delta_{ab}\delta(t_1 - t_2)$$

The thermal field $\boldsymbol{H}_{th}$ is described as a white noise term which assumes that the timescale of the thermal fluctuations is much shorter than the timescale of the spin motion. In this scenario, the noise is temporally uncorrelated. If this timescale condition is not met, the white noise approximation is insufficient and a

more complex coloured noise generator would be needed to model the fluctuations (84). However, for this thesis, the white noise approximation is sufficient as the model breaks down either on a picosecond or sub-picosecond timescale.

4.4.2 sLLG Equation Midpoint Integration Scheme

For the Stochastic LLG equation, time integration is achieved through several methods, all discretising the time into steps such that $t = n\Delta t$, where the spins are updated at each time step. The implicit midpoint scheme by D'Aquino *et al.* (85) is a second order scheme where the time derivative is calculated at the midpoint of the solution vector, seen in Equation 4.31.

$$\boldsymbol{S}_{\text{mid}} = \frac{1}{2}(\boldsymbol{S}_n + \boldsymbol{S}_{n+1}) \tag{4.31}$$

This solution vector is used to yield the Implicit midpoint scheme:

$$\frac{\boldsymbol{S}_{n+1} - \boldsymbol{S}_n}{\Delta t} = \boldsymbol{F}\left(\boldsymbol{S}_{mid}, t + \frac{\Delta t}{2}\right) \tag{4.32}$$

where $\boldsymbol{F}$ is the drift-diffusion term from the sLLG equation, encompassing both the deterministic and stochastic parts, evaluated at the next time step midpoint, $\boldsymbol{S}_n$ and $\boldsymbol{S}_{n+1}$ are the spin positions at time $n\Delta t$ and $(n+1)\Delta t$, respectively, and Δt is the time step.

In the implicit midpoint scheme, the spin length and energy are conserved exactly, ensuring a good integrator for sLLG. However, for a system of N interacting spins, this integration scheme requires a $3N \times 3N$ system of coupled non-linear equations to be solved. Therefore, this integration scheme while precise, is computationally expensive.

To reduce this computational cost, the semi-implicit midpoint scheme is used to decouple the spins. The fields are calculated between the current and next time step. This involves a predictor and corrector step leading to an iterative solution. In the predictor step, fields are calculated at $t_{n+1/2}$ using the current magnetisation $\boldsymbol{S}_n$, and in the corrector step, the predictor fields are used to calculate the next magnetisation.

For the semi-implicit scheme to handle a large system of spins efficiently, the equations have to be analytically inverted by using a Cayley transform. This requires rewriting the sLLG equation to factor out the cross product with the spin vector. The Cayley transform combines the drift and diffusion terms into a single vector:

$$\boldsymbol{A}(\boldsymbol{S}, t) = \boldsymbol{a}(\boldsymbol{S}, t) + \boldsymbol{b}(\boldsymbol{S}, t)\Delta\boldsymbol{W} \tag{4.33}$$

where $\boldsymbol{a}$ is the deterministic drift, and $\boldsymbol{b}\Delta\boldsymbol{W}$ is the stochastic diffusion.

The Cayley transform is then applied to the spin vector:

$$\mathrm{Cay}(\boldsymbol{A})\boldsymbol{S} = \boldsymbol{S} + \frac{\boldsymbol{A} \times \boldsymbol{S} + \frac{1}{2}\boldsymbol{A} \times (\boldsymbol{A} \times \boldsymbol{S})}{1 + \frac{1}{4}|\boldsymbol{A}|^2} \tag{4.34}$$

The Cayley transform allows the semi-implicit scheme to be written as a two-step rotational update:

$$\boldsymbol{S}'_{n+1} = \mathrm{Cay}(\boldsymbol{A}(\boldsymbol{S}_n, t))\boldsymbol{S}_n \tag{4.35}$$

$$\boldsymbol{S}_{n+1} = \mathrm{Cay}\left(\boldsymbol{A}\left(\frac{\boldsymbol{S}_n + \boldsymbol{S}'_{n+1}}{2}, t\right)\right)\boldsymbol{S}_n \tag{4.36}$$

The semi-implicit model, when written explicitly with the Cayley transform, uses a rotational update instead of a translational one. These transforms guarantee the conservation of the magnetisation magnitude ($|\boldsymbol{S}_{n+1}|$) at every time step, prevent-

ing numerical drift.

5

MRAM Stack Characterization

Current industry efforts in STT MRAM focus on thermal stability while reducing critical switching current. Achieving these conflicting goals at the nanoscale requires magnetic engineering at the atomistic scale, as macrospin models may suffer numerical instabilities and fail to accurately capture all thermal effects and the resulting non-coherent switching dynamics (86).

The system modelled in this thesis utilises a SAF free layer to increase thermal stability, decrease the critical switching current, and reduces scaling difficulties, this improves data retention in downscaled MRAM devices (87). This synthetic antiferromagnetic free layer results in five times more thermal stability, but only an 80% increase in critical current (88). This configuration, however, is much more complex than a traditional pinned- and free-layer MRAM model as it involves four distinct magnetic/non-magnetic interfaces (CoFeB/MgO and CoFeB/Ru) where PMA, and RKKY are localised. In the ideal SAF MRAM configuration, the SAF layers must also switch coherently, introducing more complexity to the model.

In experiments by Parkin *et al.* (89), the strength of the RKKY interaction was controlled by varying the Ru layer thickness. However, in the simulations detailed in the following chapters, the exchange coupling was varied parametrically by directly modifying the interlayer exchange values within the simulation files, without changing the Ru layer thickness.

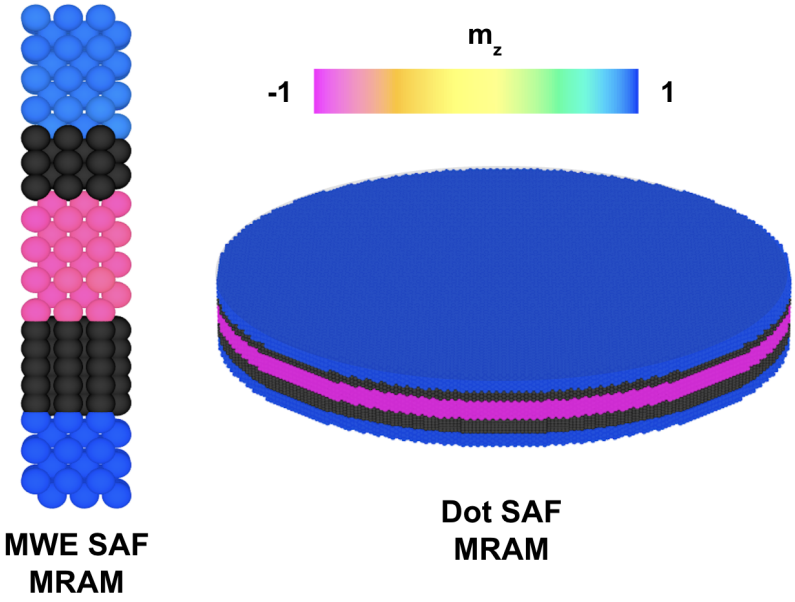


Figure 5.1: Diagram of the minimum working example (MWE) SAF MRAM with dimensions of $1 \times 1 \times 6$nm, and the dot SAF MRAM where the dot has dimensions $40 \times 40 \times 6$ nm.

The following sections describe an STT-MRAM device using a Magnetic Tunnel Junction (MTJ) stack with a synthetic antiferromagnetic (SAF) free layer. The stack, from bottom to top, is CoFeB/MgO/CoFeB/Ru/CoFeB and is shown in Figure 5.1. The top three layers form the free layer, where the intermediate Ruthenium (Ru) layer creates the SAF structure via negative exchange coupling.

5.1 Material Choice

The performance and long-term viability of MRAM are largely dependent on the materials used in the MTJ and SAF layers. The requirements for the next generation of MRAM are to have high thermal stability, low critical switching current (90). From these requirements there needs to be materials with high saturation magnetisation, and strong perpendicular magnetic anisotropy. The following sec-

tions outline the materials chosen for the MRAM device and their properties.

5.1.1 CoFeB

CoFe alloys benefit from high saturation magnetisations of 2.3 - 2.5 T as given by the Slater-Pauling curve seen in Figure 5.2. This high saturation magnetisation is required for a strong magnetic read signal and high thermal stability. The high saturation magnetisation is linked to a high spin polarisation (β), CoFeB $\beta \approx 0.56$ to 0.6, allowing the pinned layer to spin polarise the injection current and cause efficient generation of spin torque.

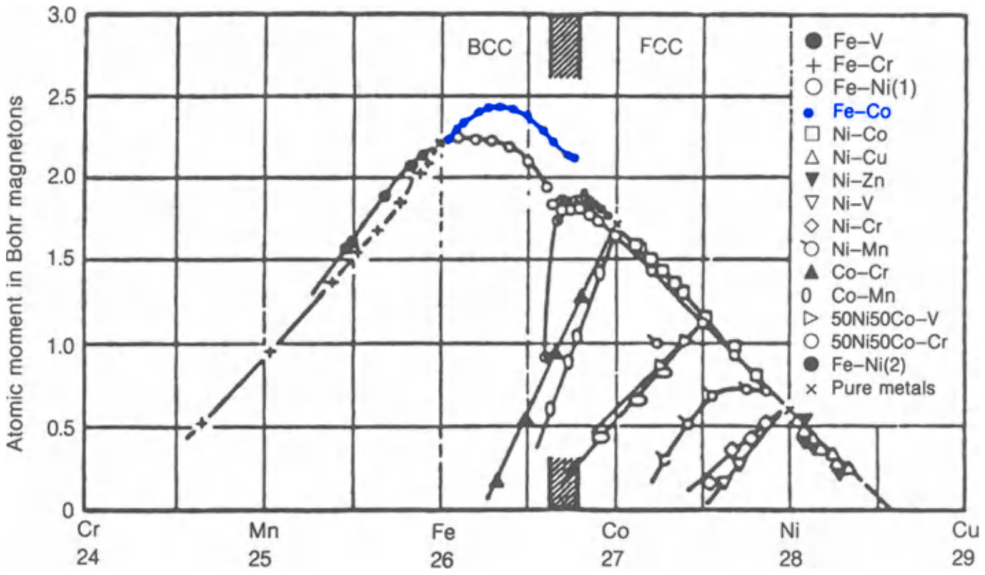


Figure 5.2: Slater-Pauling curve showing the atomic moment (μ/μ_B) against the material alloys number of valence electrons for various transition metal alloys. The Fe-Co alloy being highlighted in blue shows higher saturation magnetisation compared to other magnetic alloys, supporting its use in MRAM free layer for high density memory (7).

The addition of Boron to CoFe forms an amorphous glass that suppresses

crystal formation. Upon annealing at 360° (91), it forms the desired BCC (001) texture, which is necessary to lattice match to the highly ordered MgO layer (92). This process not only suppresses structural defects but also ensures highly coherent tunnelling and high TMR ratios at the interface. Since bulk CoFeB tends to be amorphous, the strong MgO-induced lattice matching is required to suppress this amorphous state in the ultra-thin CoFeB layer (< 2 nm). Therefore, the CoFeB is assumed to be BCC throughout the layer for all simulations.

The intrinsic Gilbert damping (α) of CoFeB is very low ($0.002-0.008$). This low damping leads to faster switching times, a lower critical current, and reduced power consumption (93). Damping is increased near interfaces by two primary mechanisms: spin pumping (94) and interface spin-flip scattering (95). Spin pumping is angular momentum loss from the CoFeB layer into an adjacent conductive, non-magnetic layer. Interface spin-flip scattering occurs at the CoFeB/MgO interface, driven by the hybridisation of Iron (Fe) and Oxygen (O) orbitals. This hybridisation simultaneously enhances the perpendicular magnetic anisotropy (PMA) and increases the scattering (96).

5.1.2 Ruthenium

Ruthenium is used as the non-magnetic spacer in the synthetic antiferromagnetic free layer due to its role in generating an antiparallel coupling through the RKKY interaction. The RKKY coupling between the magnetic free layers depends on distance as described in Section 2.2. Ruthenium's high spin transparency, allows polarised spin currents to penetrate easily through it.

Ruthenium being a $4d$ transition metal and having a long diffusion length ($\lambda_{\text{sdl}} \approx 7$ nm) leads to having high spin transparency. This spin transparency is due to its relatively weak spin-orbit coupling compared to heavier $5d$ metals, such as

Platinum. Weak spin-orbit coupling minimises the spin-flip scattering rate. This ensures the spin polarised current moves through the Ruthenium with minimal loss of angular momentum, maximising the generated spin torque.

5.2 CoFeB/MgO/CoFeB MTJ

For reliable, low-current, and fast switching, the MTJ must have high thermal stability (Δ) and a sufficiently large read margin, achieved through a high TMR ratio and strong interfacial anisotropy.

Coherent Tunnelling and TMR

CoFeB/MgO/CoFeB MTJs offer high TMR ratios due to the lattice matching between CoFeB and MgO(001) with a mismatch of only 3%. Unlike amorphous spacer layers such as Al_2O_3, which exhibit incoherent tunnelling, the crystalline MgO barrier enables coherent tunnelling through Δ_1 channels. Coherent tunnelling yields much higher TMRs than incoherent tunnelling; for example, over 600% at room temperature in a CoFeB/MgO/CoFeB MTJ compared with just 18% at 300 K in an $Fe/Al_2O_3/Fe$ MTJ (52).

Thermal Stability Factor (Δ)

The thermal stability of MRAM devices is governed by the Arrhenius-Néel law, which describes the spontaneous reversal, or thermal relaxation, of a single-domain magnetic particle over an energy barrier. This relaxation time (τ) to spontaneously switch states (parallel/antiparallel) is given by:

$$\tau = \tau_0 e^{\left(\frac{E_B}{k_B T}\right)} \tag{5.1}$$

where E_b is the energy barrier separating two stable magnetic states (parallel/antiparallel), k_B is the Boltzmann constant, T is the temperature of the system, τ is the relaxation time, and τ_0 is the attempt frequency, typically 1×10^{-9} s in MRAM systems (97). This definition of thermal stability is used in simulations of MRAM devices, as it is based on the concept of a magnetic moment being separated from its stable reversed state by an energy barrier.

From the Arrhenius-Néel Law the thermal stability factor, which determines data retention time, is found and defined as:

$$\Delta = \frac{E_b}{k_b T} \tag{5.2}$$

A factor of $\Delta \geq 60$ is typically required for commercially viable, 10-year data retention (98).

The energy barrier E_b that prevents random thermal switching is primarily determined by the magnetic anisotropy and volume of the free layer:

$$E_b \approx \frac{1}{2}\mu_0 M_s H_k V \tag{5.3}$$

where μ_0 is the permeability of free space, M_s is the spontaneous magnetisation of the free layer material, H_k is the anisotropy field, and V is the volume of the free layer. The effective anisotropy (K_t) provides this energy barrier and is defined as:

$$K_t = K_b - \frac{\mu_0 M_s^2}{2} + \frac{K_i}{t} \tag{5.4}$$

where K_b is the bulk anisotropy from magnetocrystalline origin only, $(-\frac{\mu_0 M_s^2}{2})$ is the demagnetising field, K_i is the interfacial anisotropy, and t is the ferromagnetic layer thickness .

Along the CoFeB/MgO interface, the hybridisation of Fe/Co $3d$ and oxygen $2p$ orbitals causes large interfacial anisotropy (K_i). When the CoFeB layer is ultra-thin (1.0 - 1.5 nm), the $\frac{K_i}{t}$ term becomes dominant as the bulk term K_b is negligible. Since the negative demagnetising term $-\frac{\mu_0 M_s^2}{2}$ favours in-plane magnetic alignment, perpendicular magnetic anisotropy is achieved only when the interfacial anisotropy is larger than the demagnetising field, which is the configuration discussed in this thesis.

Table 5.1: The properties of bulk and interfacial CoFeB and MgO, taken from Sampan-A-Pai *et al.* (1)

	CoFeB (Bulk)	**CoFeB (Interface)**	**MgO**	**Parameter Name**
$\boldsymbol{\alpha}$	0.02	0.11	-	Gilbert Damping
$\boldsymbol{J_{ij}(J/\text{link})}$	1.547×10^{-20}	7.735×10^{-21}	-	NN exchange energy
$\boldsymbol{k_u(J/\text{atom})}$	1.35×10^{-22}	0	-	Uniaxial anisotropy energy
$\boldsymbol{\mu_s(\mu_b)}$	1.6	1.6	-	Atomic spin moment
$\boldsymbol{\beta}$	0.56	0.56	0.11	Conductivity spin polarization
$\boldsymbol{\beta'}$	0.72	0.72	0.14	Diffusion spin polarization
$\boldsymbol{J_{sd}}$	0.1	0.1	0.01	s–d exchange energy
$\boldsymbol{m_\infty(MC/m^3)}$	261.50	261.50	0.0	Equilibrium spin accumulation

5.3 CoFeB/Ru/CoFeB Synthetic Antiferromagnet

In the MRAM stack shown in Figure 5.1, the middle, Ruthenium, and top layer comprise a synthetic antiferromagnet, through inducing an RKKY-mediated negative exchange between the two CoFeB layers. The primary benefit of this is the cancellation of the dipole fields, leading to the layers having a near-zero-net moment structure (87). This reduces the stray magnetic field outside the free layers, this increases the long-term retention and thermal stability of the MRAM. With

less stray fields, MRAM can have a higher density of MRAM cells. Furthermore, by structuring the free layer as a synthetic antiferromagnet the critical current required for switching is lower than the current required to switch two separate layers, increasing the efficiency of the MRAM device.

Current research on SAF MRAM structures is broadly centred on optimising the fundamental trade-off between thermal stability and critical current in device performance. This optimisation includes tuning the Interlayer Exchange Coupling IEC, maximising switching efficiency, and enabling field-free operation.

Optimising the IEC is necessary as it influences both the data retention and switching speed. The IEC is directly influenced by the non-magnetic metallic spacer layer's electronic structure and thickness. Bendra *et al.*'s paper on optimising the IEC in a SAF free-layer MRAM utilised finite element simulations and the LLG equation to explore how precise tuning of the IEC affects magnetisation dynamics and switching efficiency (87).

The simulations in enabling field-free operation are motivated by the desire for spin-orbit torque (SOT) MRAM applications. The requirement for conventional MRAM to have an external magnetic field significantly limits scalability. SOT MRAM uses an in-plane current to induce a torque via the spin hall effect. This was investigated by Li *et al.*, who employed a spatial gradient spin texture to preserve the thermal stability of the SAF structure's while enabling deterministic switching (99).

Because these avenues rely heavily on continuous micromagnetic or finite element methods, STT SAF MRAM has not been extensively modelled using atomistic methods. This thesis provides a novel methodological approach to MRAM simulations.

Table 5.2: Properties of interfacial CoFeB and bulk Ru.

	CoFeB (Interface)	**Ru**	**Parameter Name**
$\boldsymbol{\alpha}$	0.11	-	Gilbert Damping
$\boldsymbol{J_{ij}(J/link)}$	7.735x10^{-21}	-	NN exchange energy
$\boldsymbol{k_u(J/atom)}$	0	-	Uniaxial anisotropy energy
$\boldsymbol{\mu_s(\mu_b)}$	1.6	-	Atomic spin moment
$\boldsymbol{\beta}$	0.56	0.11	Conductivity spin polarization
$\boldsymbol{\beta'}$	0.72	0.14	Diffusion spin polarization
$\boldsymbol{J_{sd}}$	0.1	0.01	s–d exchange energy
$\boldsymbol{m_\infty(MC/m^3)}$	261.50	0.0	Equilibrium spin accumulation
$\boldsymbol{\lambda_{\mathrm{sdl}}(nm)}$	1.3	7	Spin diffusion length

While many of the bulk parameters in Table 5.2 are the same as the bulk CoFeB outlined in Table 5.1, the Gilbert damping parameter for the interface between CoFeB/Ru is larger, taking into account spin pumping into the Ru layer. Ruthenium's spin diffusion length has a range from as low as 3.59 nm (100) to over 15 nm (101), the 7 nm used as an inbetween number in this thesis's simulations, employing spin-diffusion length is used as an in-between number as the simulations performed at 0 K and did not include finite-temperature effects.

5.3.1 Ruthenium structure

In bulk Ruthenium has a hexagonal close packed structure (HCP), however in MRAM, the Ruthenium is grown under strain between BCC-CoFeB (001) layers, the layers crystallise into an FCC lattice. HCP and FCC have the same packing fractions and are similar energetically, the main difference is in the stacking sequence as seen in Figure 5.3, where HCP has an ABA and FCC has a ABCABC sequence. When the Ruthenium is grown it is forced to lattice match the BCC-CoFeB structure, under this strain the FCC close packed structure becomes

energetically comparable, or in the case of Ru and Co favourable compared to HCP when grown on BCC materials.

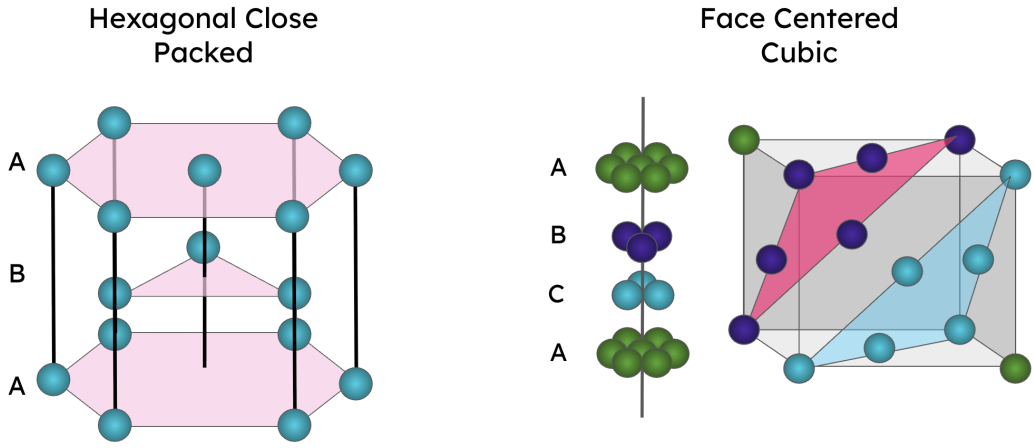


Figure 5.3: Example of hexagonal close-packed HCP and face-centred cubic FCC crystal structure, demonstrating the similarities in structure and packing fraction.

5.3.2 RKKY in CoFeB/Ru/CoFeB

The strength of the RKKY interaction is governed by the interlayer exchange coupling (J_{IEC}). In experiments on CoFeB/Ru/CoFeB the maximum observed IEC when Ru= $1nm$ is $J_{IEC} = -1.7$ mJ/m^2 (102), this provides an upper bound to the strength of the RKKY interaction can be in the atomistic simulation. To be used in the simulation, it must be converted to the exchange energy per bond, J_{ij}:

$$J_{ij} = \frac{J_{IEC}\ (\mathrm{J/m^2})}{\rho_A\ (\mathrm{atoms/m^2})} \tag{5.5}$$

To find the areal atomic density ρ_A in a BCC system in CoFeB, ρ_A is equal to $1/a^2_{\mathrm{BCC}}$, where a_0 is the in-plane lattice constant. Therefore, in a BCC system where the lattice constant is 3.5 Å:

$$\rho_A = \frac{1}{(3.5 \times 10^{-10})^2} \approx 8.16 \times 10^{18} \text{ atoms/m}^2 \tag{5.6}$$

Substituting these values generates the maximum RKKY interaction strength:

$$J_{ij} = \frac{-1.7 \times 10^{-3}}{8.16 \times 10^{18}} = -2.08 \times 10^{-22} \text{ J/link} \tag{5.7}$$

This value can be used as the upper bound for the RKKY interaction in the CoFeB/Ru/CoFeB system.

5.4 Generation in code

The Python code seen in the appendix is used to generate the simulation files for the MRAM stack's crystal structure. It generates the material input file, crystal configuration file, and simulation parameter file. The code uses monolayers of atoms to ensure the correct epitaxial stacking for the interfaces between CoFeB/MgO and CoFeB/Ru. Figure 5.4 highlights the interface atoms in green, which are defined separately from the bulk CoFeB due to their unique interfacial characteristics. These properties, including the Gilbert damping, RKKY coupling, and significant interfacial anisotropy, differ from bulk values and must be defined independently to ensure accuracy of the model.

All CoFeB layers and interfaces are modelled as a BCC structure. MgO is modelled as a rock-salt like structure, with a FCC lattice with two interpenetrating an FCC sublattices: one of Mg^{2+} ions and one of O^{2-} ions, offset by half a lattice constant. This lattice structure matches exactly to the CoFeB lattice, though in simulation, the interface layer has its properties altered to reflect experimental data.

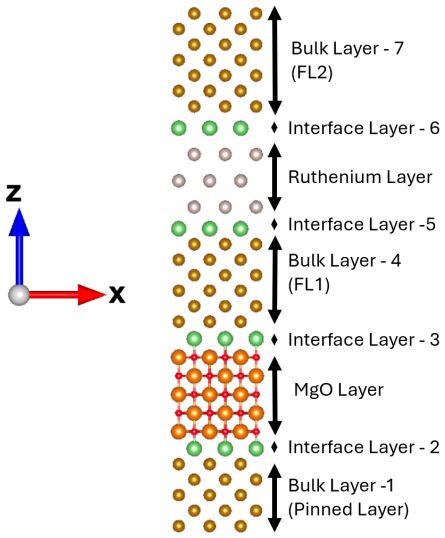


Figure 5.4: Diagram of the MWE MRAM in VESTA highlighting the interfaces in green, CoFeB in gold, oxygen in red, Mg in orange, and Ruthenium in white. The labelled layers correspond to those in Table 5.3.

5.4.1 Parameter Mapping and Nearest Neighbours

For CoFeB, all atoms in the bulk layer are assigned their intrinsic values through parameter mapping. This is generated by a Python script which creates the simulation input files (see Appendix). The script generates a simulation material file with the intrinsic exchange (J_{ij}), Gilbert damping parameter, and atomic spin moment in relation to their nearest neighbours, other CoFeB atoms. The CoFeB interface layers adjacent to the MgO are assigned a strong uniaxial anisotropy to account for orbital hybridisation of Fe-O at the interface. Gilbert damping parameter is explicitly given to all atoms and takes into account spin pumping and spin-flip interactions at interfaces. All material properties are assigned to each interface and material using "vamp_mat_id", this ensures the different interfaces and bulk material have different properties despite being the same material.

5.4.2 RKKY Interlayer Exchange Coupling

The nearest-neighbour calculation used in the rest of the simulation does not extend to cover the distances required to simulate the RKKY interaction that goes through the Ruthenium layer. Consequently, a specialized treatment within the code is required. The RKKY interaction is calculated through a defined function that uses Equation 5.8 which depends on the atomic distance, and is discussed further in Section 2.2.

$$J_{RKKY}(d) = J_0 \frac{\cos(2\pi k_F d)}{d^3} \tag{5.8}$$

where J_0 is the exchange interaction between two CoFeB atoms at their bulk atomic distance, and d is the distance between two CoFeB atoms across the Ru layer.

The RKKY interaction in code uses targeted coupling allowing the creation of effectively a nearest neighbour calculation to extend across the Ruthenium layer. This nearest-neighbour calculation used `mat_id = 5` and `mat_id = 7` to ensure the coupling is only between the interface layers around the Ruthenium. The RKKY calculation also employs an epitaxial alignment check. To simplify the calculation, the interface atoms are directly stacked on top of each other, this is checked through ensuring the Ruthenium has an odd number of monolayers and the epitaxial check `atom.position[0] == other_atom.position[0]`. The Ruthenium is modelled as non-magnetic and are assigned zero magnetic moment or exchange coupling, functioning as a pure non-magnetic spacer.

5.5 Curie Temperature

The Curie temperature (T_{C}) represents a hard upper bound for the operating temperature of an MRAM device, making its accurate determination essential. Operation of the MRAM stack near the T_{C} results in the collapse of spontaneous magnetisation and therefore has no thermal stability and is not able to be used.

Standard Monte Carlo methods become inefficient near T_{C} due to critical slowing down. The adaptive Monte Carlo algorithm is applied within the VAMPIRE software to significantly reduce the autocorrelation time (τ_{corr}), which ensures an accurate estimation of T_C despite critical slowing down.

5.5.1 Finite Size Scaling (FSS)

In materials of finite size, typically in nanometres such as in MRAM, the Curie temperature is typically reduced compared to its bulk value. This reduction is due to reduced coordination, and loss of criticality.

The reduced coordination originates from when the size of a system is reduced, the atoms at the surface have less nearest-neighbours than those in the bulk, leading to a weakening in the exchange interaction. This weakening in exchange directly reduces the Curie temperature.

The loss of criticality is where the divergence of spin-spin correlation length near T_C is limited by the system size and leads to a rounded critical behaviour.

$$M(T) \approx |T_C - T|^{\beta} = 1 - \left(\frac{T}{T_C}\right)^{\beta} \tag{5.9}$$

Where $M(T)$ is the Magnetisation at temperature T, T_{C} is the Curie temperature, and β is the critical exponent.

Equation 5.9 is used to find the Curie temperature from the rounded phase transition data. By using a scaled-down version of the large MRAM stack, the intrinsic properties of thermal stability can be found and compared against a larger system.

5.5.2 Curie Temperature Results

The T_C for a simple MRAM stack with a CoFeB pinned layer, MgO layer, and CoFeB free layer is represented in Figure 5.5 and the visualisation in Figure 5.6 . This configuration is found to have a Curie temperature of (1071 ± 1.0) K, and the full SAF MRAM stack has a T_C of (1052 ± 1.1) K.

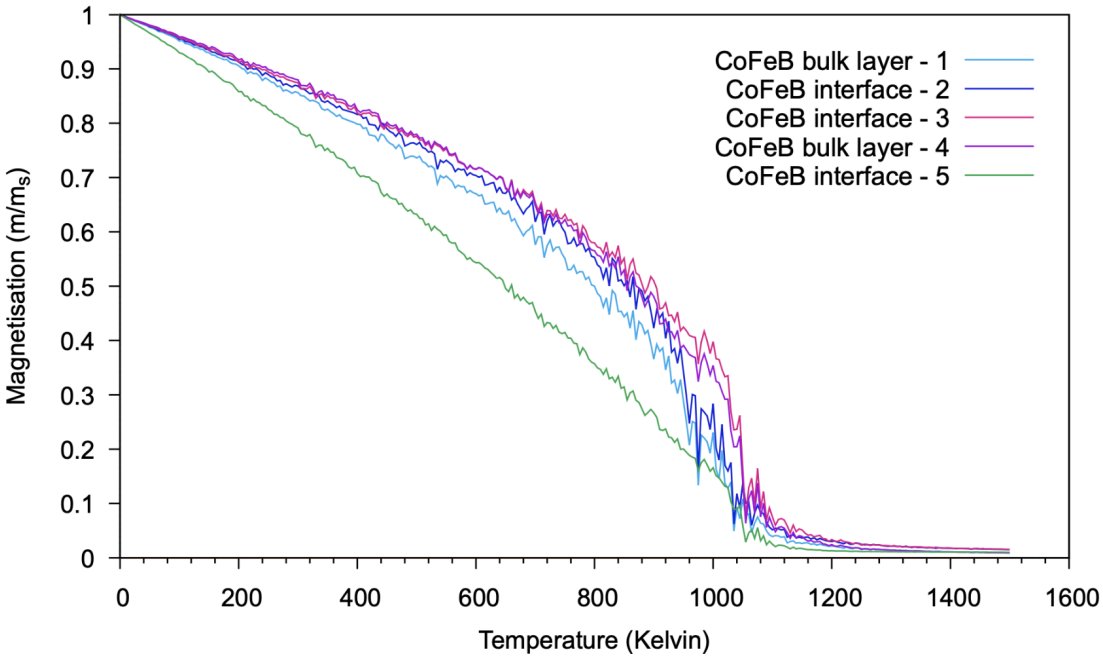


Figure 5.5: Magnetisation ($\boldsymbol{M}$) versus Temperature (T) curve of a simple MRAM stack: CoFeB/MgO/CoFeB. Showing the layer-resolved magnetisation that have different critical exponents (β) from different environments, such as CoFeB interface layer 5, on the surface, exposed to the vacuum.

In this structure, the CoFeB interface layer exposed to vacuum (Layer 5) shows

a lower effective critical exponent (β), resulting in a more gradual demagnetisation over a broader temperature range. This behaviour is a direct consequence of the finite-size effects arising from the reduced coordination at the free surface.

Conversely, the other bulk and interface layers show a sharp drop in magnetisation near T_C, characteristic of a higher effective β. The layers that are not separated by the tunnel barrier, such as layers 1 and 2, exhibit similar thermal behaviour due to the stronger exchange coupling between adjacent bulk and interfacial layers compared to coupling across the tunnel barrier. Snapshots illustrating the temperature dependence of the magnetisation are shown in Figure 5.6.

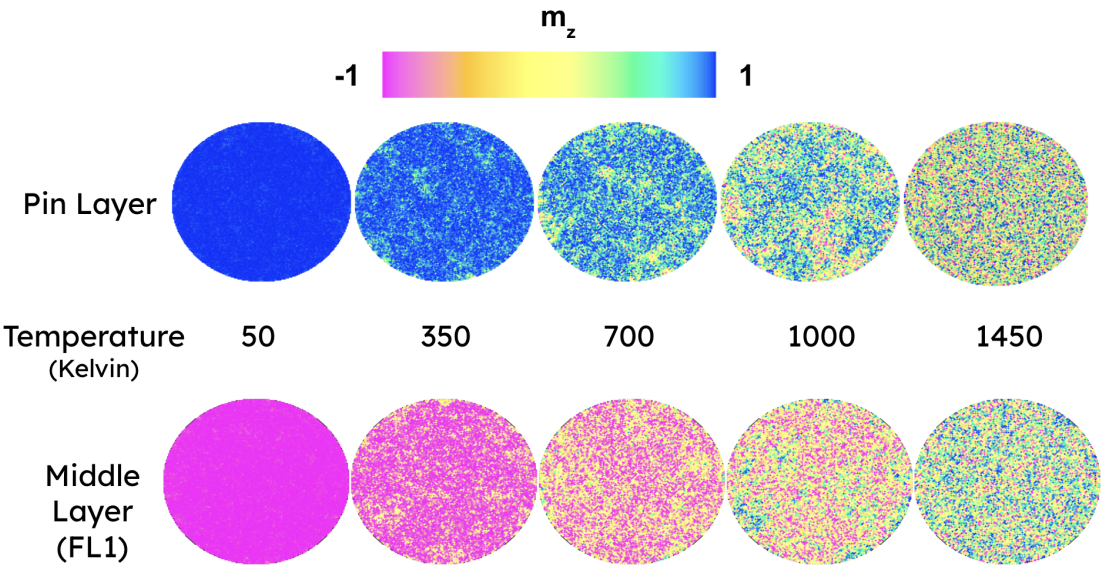


Figure 5.6: Snapshots of Magnetisation at various Temperatures in Kelvin for the MRAM stack of CoFeB/MgO/CoFeB. The colour scheme is shown where the (m/m_S) is from pink at -1, to blue at $+1$. These show the temperature dependence of (m/m_S).

In larger systems, mean material magnetisation, $\boldsymbol{M}(T)$, fluctuates, resulting in a noisy curve at lower temperatures (103). This noise is due to the apparent reduction in spin correlation caused by competing short-range exchange interactions. These fluctuations are characterised by the longitudinal susceptibility ($\chi_{\parallel}$)

and the transverse susceptibility ($\chi_\perp$).

$\boldsymbol{\chi}_\parallel$ measures the fluctuations in the magnitude of the exchange length parallel to the easy (z) axis and shows the largest peak in susceptibility at the Curie temperature:

$$\boldsymbol{\chi}_\parallel = \frac{1}{k_B T}(\langle \boldsymbol{M}_z^2 \rangle - \langle \boldsymbol{M}_z \rangle^2) \tag{5.10}$$

where $\boldsymbol{\chi}_\parallel$ is the isotropic susceptibility, and $\boldsymbol{M}_z$ is the total magnetisation in the easy axis (z direction).

$\boldsymbol{\chi}_\perp$ measures these same fluctuations perpendicular to the easy axis:

$$\boldsymbol{\chi}_\perp = \frac{1}{2k_B T}(\langle \boldsymbol{M}_x^2 \rangle + \langle \boldsymbol{M}_y^2 \rangle) \tag{5.11}$$

where $\chi_\perp$ is the transverse susceptibility, and $\boldsymbol{M}_x$ and $\boldsymbol{M}_y$ are the total magnetisation components in x and y direction respectively.

The noise observed in the $M(T)$ graph, in Figure 5.7, shows the magnetic fluctuations. By applying the susceptibility analysis as outlined in equations 5.10 and 5.11, these fluctuations can be quantified. Figure 5.7 shows the layer-resolved magnetisation where interface layer 5 and 6, that surround the Ruthenium layer, show finite size effects. These effects result in a lower Curie temperature, and higher critical exponent seen in Table 5.3.

5.6 Hysteresis

Hysteresis is the history dependence of magnetisation $\boldsymbol{M}$ on the applied field $\boldsymbol{H}$ (104). It is caused by the system's anisotropy, as the applied field must overcome local energy barriers to switch magnetisation. The loop is generated based on the LLG equation. The shape of the hysteresis loop defines three key parameters:

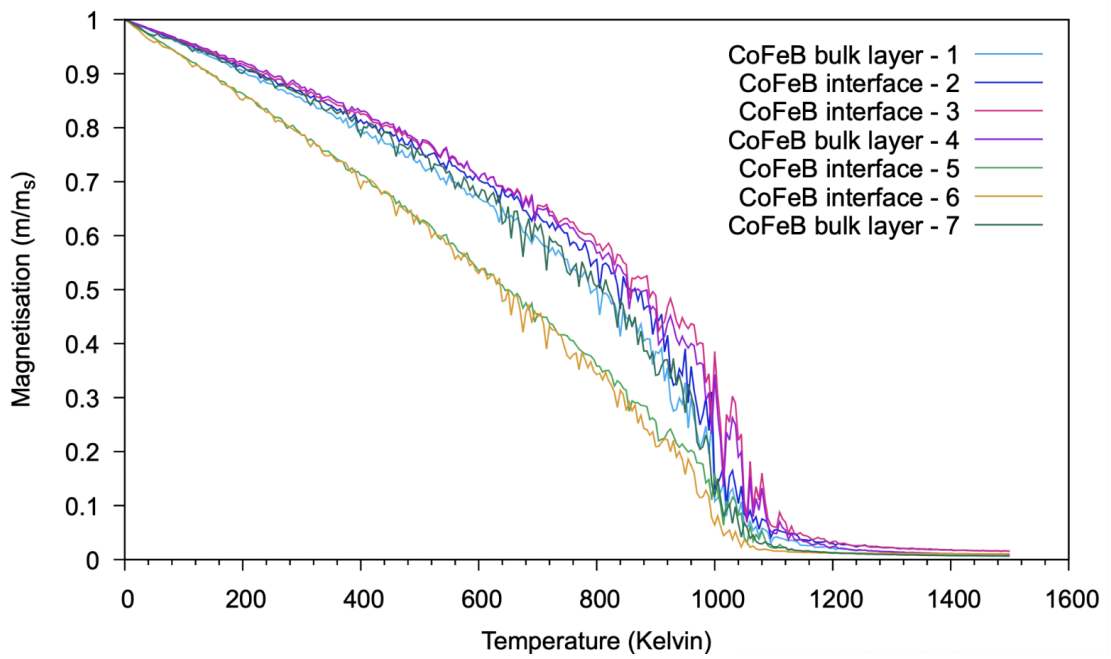


Figure 5.7: Magnetisation ($\boldsymbol{M}$) versus Temperature (T) curve of the full MRAM stack with CoFeB/MgO/CoFeB/Ru/CoFeB, showing the layer-resolved magnetisation and finite size effects of the top layer where due to weak RKKY interaction the interface layers have a lower critical exponent.

Table 5.3: Curie temperature by layer, with critical exponent, showing the lower exchange in RKKY coupling (-1×10^{-23} J/link) compared to bulk and interfacial MgO layers creates a finite size effect and, therefore, a lower Curie Temperature.

Layer Name	**Curie Temperature**(K)	**Critical Exponent** (β)
Bulk layer - 1	1038 ± 1	0.487 ± 0.001
Interface layer - 2	1063 ± 2	0.477 ± 0.002
Interface layer - 3	1102 ± 2	0.473 ± 0.002
Bulk layer - 4	1092 ± 2	0.479 ± 0.002
Interface layer - 5	966 ± 3	0.502 ± 0.002
Interface layer - 6	937 ± 3	0.500 ± 0.003
Bulk layer - 7	1037 ± 1	0.488 ± 0.001

saturation magnetisation (M_{S}), remanent magnetisation (M_{R}), and Coercive Field (H_{C}).

M_S is the maximum $\boldsymbol{M}$ where a further increase in $\boldsymbol{H}$ does not increase the $\boldsymbol{M}$ of the MRAM stack. M_{R} is the remaining $\boldsymbol{M}$ when $\boldsymbol{H}$ returns to zero. H_{C} is the $\boldsymbol{H}$ required to switch the MRAM stack to zero magnetisation.

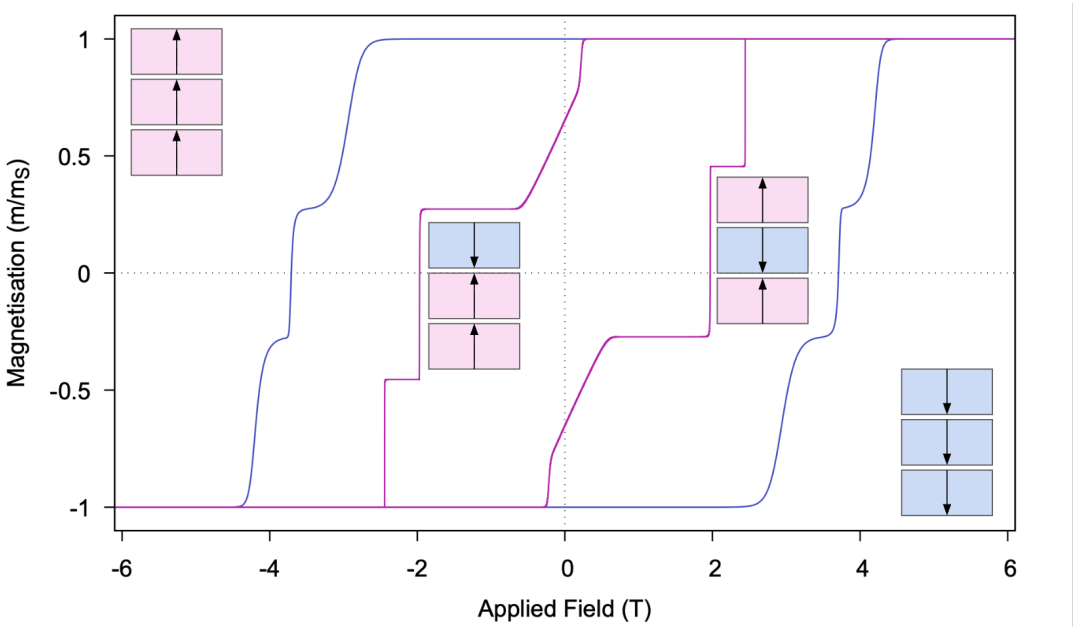


Figure 5.8: Sweep rate (T/s) dependence of CoFeB/MgO/CoFeB/Ru/CoFeB where the blue line has a sweep rate of 1×10^{13} T/s and the purple line has a sweep rate of 1×10^{11} T/s. The diagrams show the orientation of the pin and SAF free layers at each step. The highly variable sweep rate shows a dynamic hysteresis needing many loop steps to equilibrate (8).

Dynamic Effects and Simulation Protocol

Accurate hysteresis measurement requires a slow field sweep rate, as seen in Figure 5.8. A fast sweep rate leads to dynamic effects and an overestimation of the coercive field (105). The dynamic effects include non-equilibrium switching and delayed reversal.

Non-equilibrium switching occurs when the rate of field change exceeds the time required for the reversal of the magnetic moments. Delayed reversal occurs

when the spin has not had sufficient time to explore lower-energy switching configurations, resulting in an apparently higher energy barrier which requires a stronger applied field to complete the reversal.

For the hysteresis loops investigating the RKKY effects, the PMA-MRAM stack is based on the version seen in Chapter 6. The simulation uses a sweep from -10 T to 10 T, with 0.0001 T steps. At each step, the system is allowed to equilibrate using 1000 time steps of 1.0 fs each before the field is changed. The resulting hysteresis loop describes the MRAM's critical current, This is important for finding the optimal switching scheme where FL1 and FL2 can switch without aligning in parallel.

5.6.1 RKKY Effects

A systematic approach was taken to explore how RKKY strength affects the hysteresis loop. A synthetic antiferromagnetic free layer creates a stair-like hysteresis loop as there are several stable magnetisation states when a large magnetic field can be applied. The fully saturated state, both free layers are aligned in parallel so the net magnetisation ($\boldsymbol{M}_z/\boldsymbol{M}_\mathrm{s}$) is equal to ± 1.

The intermediary state, the free layers are in an antiparallel state, leading the net magnetisation to be ≈ 0. When there is a strong RKKY interaction, at $\boldsymbol{H} = 0$ the antiparallel state is stable. However, with weak RKKY interactions the antiparallel state is less stable and the stair-like switching transition becomes less pronounced, which indicates a weaker internal coupling field. To ensure the validity of the loops, a convergence test was performed by varying the sweep rate and found increasing the equilibration steps above 1000 with a field increment of 0.01 T, results in negligible changes to the magnetic response. Figure 5.9 (a) shows the hysteresis loops for -1×10^{-20} and -1×10^{-21} J/link strength RKKY,

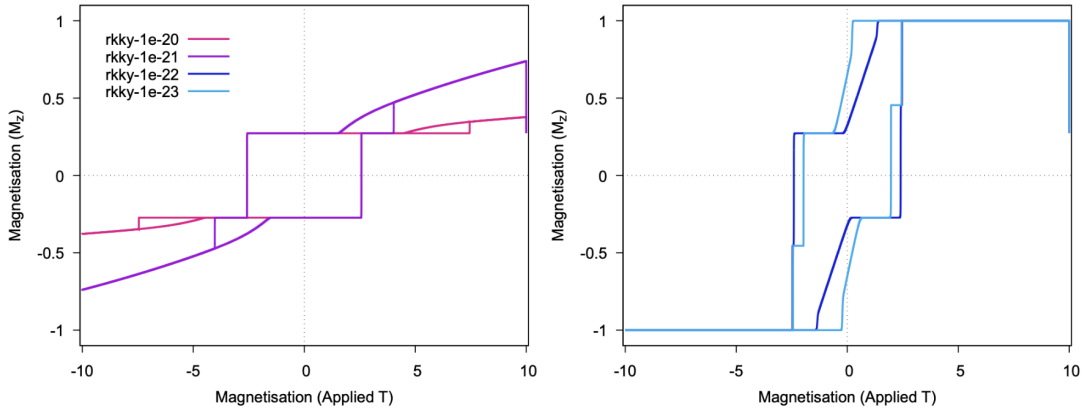


Figure 5.9: Comparison of hysteresis loops with varying RKKY interaction strength. Seen in the right graph the RKKY interaction reaches the saturation magnetisation ($\pm$ 1) when the applied magnetiic field is less than 5 T. The pink line (-1$\times 10^{-20}$ J/link) and the purple line (-1$\times 10^{-21}$ J/link) in Figure 5.9 (a) show the systems not reaching saturation magnetisation under 10 Tesla. In contrast, the dark blue (-1$\times 10^{-22}$ J/link) and the light blue line (-1$\times 10^{-23}$ J/link) reach saturation magnetisation in less than 5 Tesla.

this shows the effect RKKY has in preventing saturation magnetisation under strong applied fields up to 10 T. This contrasts to the dark blue line representing -1$\times 10^{-22}$ J/link in Figure 5.9 (b), where the system is able to switch under much lower applied magnetisation while still having enough RKKY to maintain the top layers antiparallel alignment at zero applied magnetic force. This can also be seen as not the case when RKKY is -1$\times 10^{-23}$ J/link as the system's magnetisation at zero applied magnetism is above 0.5 T and below -0.5 T.

6

Parameter Sweep for Small System

The behaviour of STT-MRAM is dependent on many interrelated material and operational parameters, such as anisotropy, damping, RKKY strength, and current density. To understand, the influence of a single variable on the MRAM a parameter sweep is necessary. The parameter sweep involves fixing all parameters except one, which is then varied across reasonable operating values. This isolates the influence of a single variable on the system and allows the optimisation of future MRAM designs.

The initial analysis of magnetisation dynamics is performed using a small-system MRAM cell ($1 \times 1 \times 6$ nm) seen in Figure 6.1. This works as a minimal working example (MWE) designed to be used to force coherent switching dynamics to examine fundamental dynamics.

This system forces coherent switching dynamics, as its small dimensions suppresses the formation of complex spin textures such as domain walls or vortices. This ensures coherent switching, and the analysis of simple MRAM switching. The switching is used as benchmarking as it establishes the maximum switching speed and critical switching current unimpeded by incoherence. These dynamics form the basis of comparison for the more complex systems explored in later chapters.

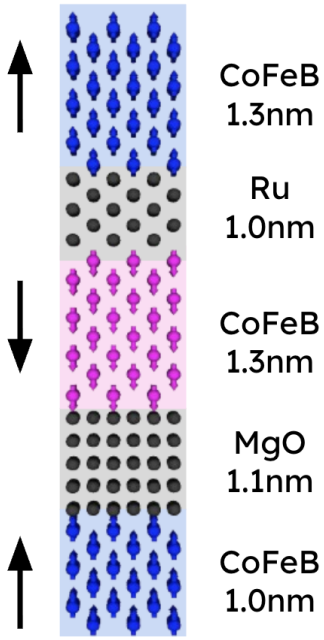


Figure 6.1: Diagram of the small system MRAM cell, $1 \times 1 \times 6$ nm

6.1 Incubation and Switching Time

The total time needed to completely switch the free layer is made up of two components: the incubation time, and the switching time, as seen in Figure 6.2.

The incubation time originates from the time required to overcome the static energy barrier. The accumulation of spin in the free layer until enough torque is generated to initiate switching. In simulations, it is defined as the time taken ($t_{\text{incubation}}$) for the magnetisation component along the anisotropy axis (lM_z) to deviate by 10% from its initial state. The reversal time is the duration over which the magnetisation rotates 180° from its initial antiparallel or parallel state. In simulations, the reversal time is measured from the end of the incubation period and is the time taken for the free layer to achieve 90% of its final magnetisation.

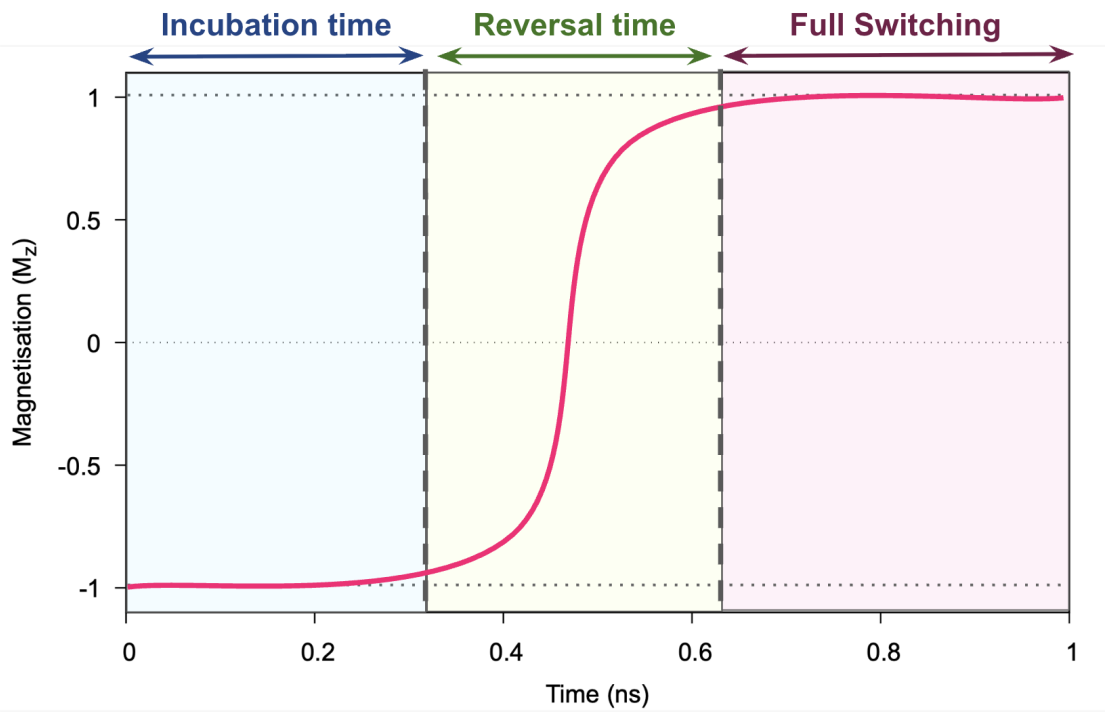


Figure 6.2: Magnetisation reversal showing three distinct regions, the incubation time in light blue, the reversal time in yellow, and full switching in pink.

6.2 Benchmark

A benchmark simulation was conducted to establish the switching mechanism of the MRAM device at 0 K and provide a reference for subsequent parameter sweeps. The simulation used 0 K to eliminate thermal effects, along with an applied magnetic field of 1 T to reliably induce STT switching. The RKKY exchange coupling was set to a strongly antiparallel value of -1×10^{-21} J/link , ensuring a strong coupling between the Free Layer 1 (FL1) and Free Layer 2 (FL2), facilitating a synchronised reversal. Additionally, the FL2 anisotropy was set to 5×10^{-24} J/link, which is sufficient for maintaining the FL2's thermal stability. Other parameters were defined according to Table 5.1. The primary objective was to produce a pre-

dictable switching event for comparison against simulations investigating critical factors, like RKKY strength, FL2 polarisation, and the critical switching current.

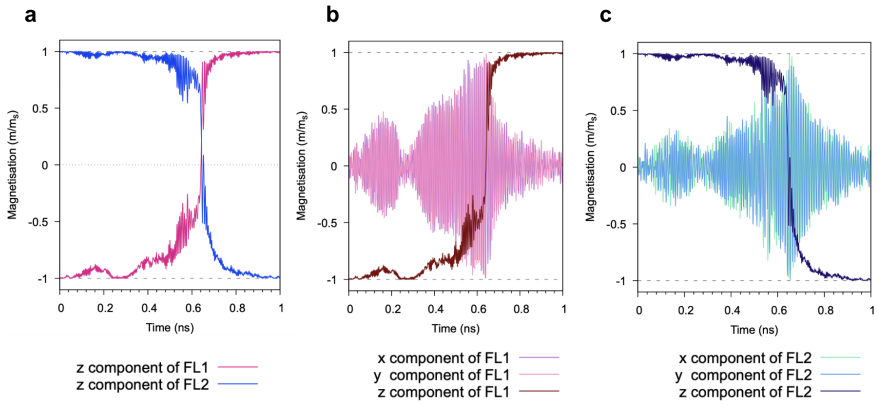


Figure 6.3: Magnetisation switching of MRAM device with zero polarisation injected into FL2. Key parameters: FL2 anisotropy 5×10^{-24} J/link, RKKY exchange coupling -1×10^{-21} J/link, (a) the z components of the bulk SAF layers, (b) and (c) the x, y, and z components of FL1 and FL2.

The magnetisation components $(\boldsymbol{m}_x, \boldsymbol{m}_y, \boldsymbol{m}_z)$ of FL1 (b) and for FL2 (c) in Figure 6.3 show a two-step reversal process. The switching initiates when the applied STT drives the reversal of FL1. The strong antiparallel RKKY coupling then drives FL2 to switch as FL1 begins its reversal, resulting in a highly correlated process. In this specific simulation, FL1 switching is driven solely by the STT, while FL2 switching is driven solely by the strong RKKY interaction.

Figure 6.4, provides a 3D visualisation of Figure 6.3 in POV-Ray, illustrating the two-step switching process where FL1 switches before FL2. This is most obvious at 0.7 ns in Figure 6.4, where FL1 has switched fully while FL2 has not yet completely switched.

The strong RKKY coupling ensures that the longitudinal components (m_z) of the SAF layers switch almost simultaneously. The high-frequency oscillations observed in the transverse components (m_x, m_y) are the defining characteristic of

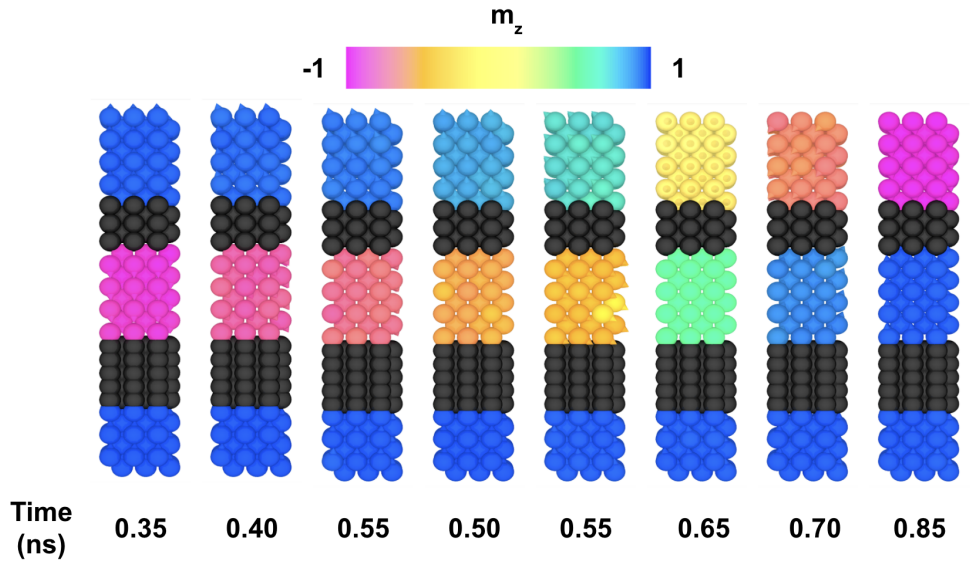


Figure 6.4: Simulation of switching occurring with top layer of anisotropy of 5×10^{-24} J/link, RKKY of -1×10^{-21} J/link, and zero polarisation being injected into the top layer.

precessional switching, which occurs due to the low damping coefficient (0.02) used in the simulation.

6.3 Parameter Sweep

The parameter sweep explores the performance envelope of the small-system MRAM device. This sweep systematically varies three key parameters to find the optimal switching scheme that balances speed, critical field, and thermal stability:

1. Anisotropy (critical field),
2. RKKY strength, and
3. Polarisation strength.

This analysis is essential because MRAM devices exhibit a trade-off: increased thermal stability requires a higher energy barrier, which in turn necessitates a

higher critical field to switch. The previously established MWE is used to systematically vary these parameters and provide a qualitative understanding of how each effect governs the speed, and critical field of the MRAM stack.

6.3.1 Effect of STT Field Magnitude

The primary driving force of switching in this MWE MRAM device is the applied STT field. To determine the minimum critical field for deterministic switching, the parameter space is explored at 0 K to prevent any switching from thermal effects. In this parameter sweep, the RKKY interaction is -1×10^{-21} J/link, the top layer anisotropy is 5×10^{-24} J/link, the STT deposited in FL2 is 0, and the STT deposited in FL1 is varied. This is done to find the critical switching field when the switching in FL2 is driven solely by RKKY exchange.

The simulations demonstrate three distinct qualitative regimes governed by the magnitude of STT that is deposited into FL1. First, in the low-STT scheme, the magnitude of the STT is insufficient to overcome the anisotropy barrier (Δ), and the MRAM is unable to undergo reversal. In the optimal STT regime, the STT is able to overcome the anisotropy barrier and, within the operating range, increasing the magnitude of STT creates a faster switching time until the point of instabilities occur. In the High-STT regime the system creates oscillations in the lm_x - lm_y plane preventing switching.

This non-switching can be seen in Figure 6.5, this figure demonstrates the magnetic moments do not deviate from the initial magnetisation direction despite the applied field. This shows the magnitude of STT in FL1 is less than the restoring torque exerted by the perpendicular magnetic anisotropy, the moments are effectively pinned by the anisotropy. Mathematically this can be described as

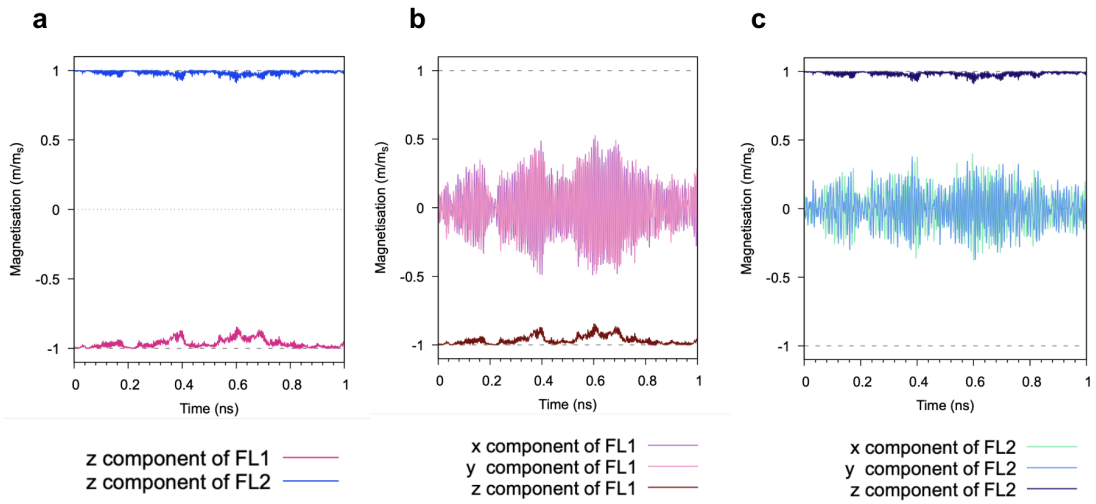


Figure 6.5: Non-switching dynamics of MRAM with the STT deposited in FL1 = 0.8 Tesla, demonstrating failure to switch or deflect from initial magnetisation direction. This scheme is typical for low current with a high PMA.

the sum of all torques being equal to zero :

$$\boldsymbol{\tau}_{\text{anisotropy}} + \boldsymbol{\tau}_{\text{STT}} + \boldsymbol{\tau}_{\text{Damping}} \approx 0 \tag{6.1}$$

This defines the lower operational bound for STT strength for this MRAM stack.

In the optimal switching scheme, the $\boldsymbol{H}_{\text{STT}}$ overcomes the PMA barrier and the MRAM is able to reverse, as seen in Figure 6.6. In this scheme it can be seen that incubation time decreases with increasing STT field, however past 1.2 Tesla, instabilities occur and delay full switching.

At an STT field of 0.95 T, seen in Figure 6.6(a), the minimum amount of field required for switching is found. Increasing the STT field to 1.2 as seen in Figure 6.6(b) the switching time is reduced to 0.31 ns, but this begins to introduce in-

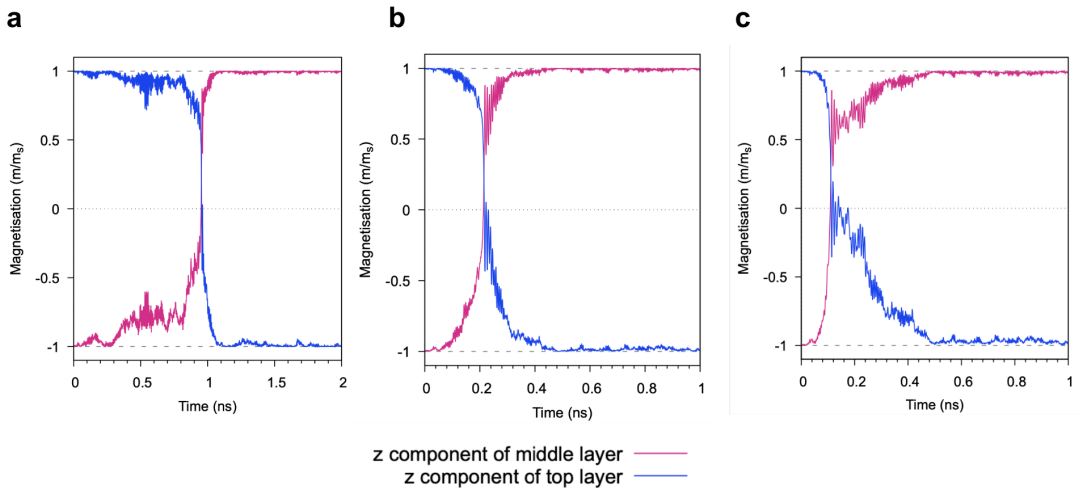


Figure 6.6: Switching of (a) with STT field in FL1 of 0.95 Tesla, the minimal switching field found when increasing the STT field in 0.05 T increments. (b) STT in FL1 of 1.2 Tesla, (c) STT in FL1 of 1.6 Tesla, where the incubation time is minimal.

plane oscillations (m_x, m_y). At 1.6 T, Figure 6.6(c), while the initial incubation time is minimised the, the onset of precessional instabilities delays the complete reversal.

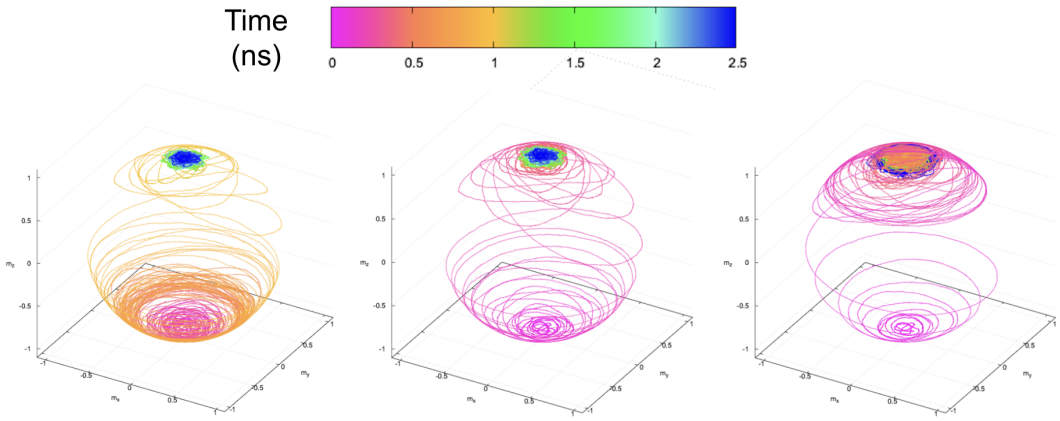


Figure 6.7: Switching dynamics of FL1 plotted in 3D with axis representing the magnetisation direction of $\boldsymbol{m}_x$, $\boldsymbol{m}_y$, and $\boldsymbol{m}_z$. Where (a) has the STT in FL1 of 0.95 Tesla, (b) STT in FL1 of 1.2 Tesla, and (c) STT in FL1 of 1.6 Tesla.

The 3D trajectory plots in Figure 6.7 visually demonstrates the trade-off between incubation delay and precessional stability. While higher field reduce the incubation time, they can introduce pronounced precession in the m_x and m_y axes. An STT field of 1.2 T represents the optimal operating point for this stack.

As the STT field increases past 1.6 T, the STT field minimises the incubation time as the STT torque immediately pushes the magnetic moment away from the z axis. However, as seen in Figure 6.6 (c), while the onset is fast, the total switching time is delayed due to dynamic instabilities. The 3D trajectory as seen in Figure 6.7 (c) highlights the precession around the x and y axis, showing the high torque preventing coherent reversal. In cases such as those illustrated in Figure 6.8, the STT injected in FL1 is high enough that creates dynamic instability preventing switching at all, and is unsuitable for use in MRAM. In Figure 6.8 (d) shows the magnetisation of FL1 rotating at a range between 0.5 and 1.0 in the z-direction, while oscillating in the x-y plane.

6.3.2 RKKY effects

The RKKY exchange couples the synthetic antiferromagnetic free layer and determines the strength of the parallel and antiparallel alignments. The RKKY exchange adds a significant term to the overall effective magnetic field ($\boldsymbol{H}_{\text{eff}}$) experienced by each layer. Therefore, investigating the influence of varying the RKKY strength on thermal stability and critical switching current is essential for understanding the optimal parameter space. The RKKY interaction has two competing roles in the MRAM: increasing thermal stability (by increasing $\boldsymbol{H}_{\text{eff}}$), and facilitating coherent reversal of the second layer. To characterise these contrasting objectives, a parameter sweep was conducted, varying the RKKY strength from 1×10^{-23} to 1×10^{-20} J/link while keeping all other parameters equal to the

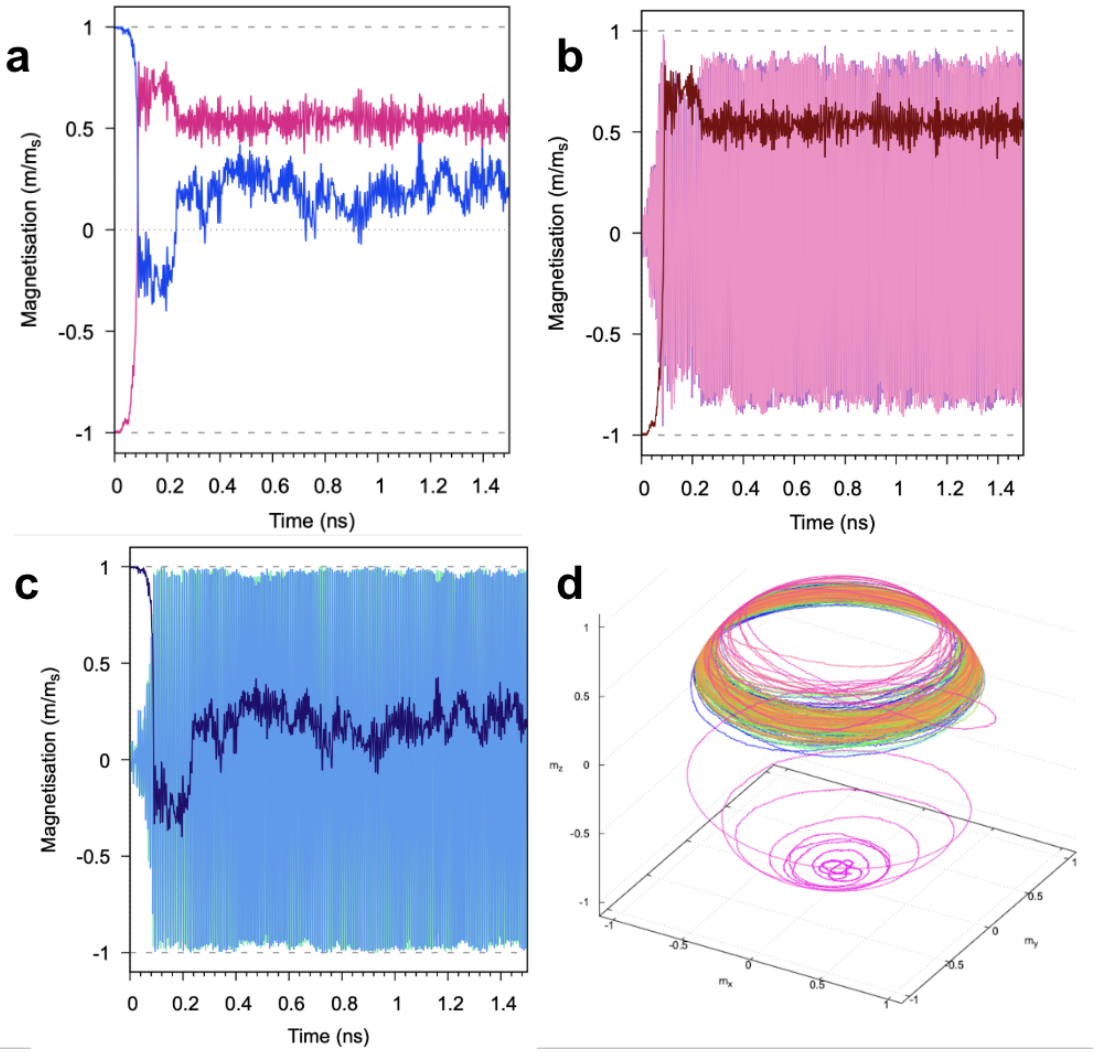


Figure 6.8: STT in FL1 is 1.9 Tesla, creating dynamic instability which creates a precession that prevents switching. The parameters used are outlined in "Effect of STT Field Magnitude". (a) is the z components of FL1 and FL2, (b) are the xyz components of FL1, (c) are the xyz components of FL2, and (d) is the 3D plot of magnetisation direction in FL1.

benchmark simulation.

Effect on Switching Dynamics

Strong RKKY interactions (eg., -1×10^{-20} J/link) prevent the MRAM from switching because the coupling creates a large internal $\boldsymbol{H}_{\text{eff}}$ that the applied STT

cannot overcome. The optimal RKKY coupling regime allows the STT to overcome the PMA and RKKY coupling barrier, assisting the MRAM switching for a highly correlated and fast switching.

Table 6.1: Table of RKKY strengths, the time taken to switch in nanoseconds, the percentage increase or decrease from the benchmark calculation, and the type of dynamic. The parameters used are the same as the benchmark simulation (STT in FL1 is 1.0 T , STT in FL2 is 0.0 T) with varying RKKY.

RKKY strength (J/link)	t_{switch} **(ns)**	**% change from Baseline**	**Dynamic**
-1×10^{-20}	N/A	N/A	Non-Switching
-1×10^{-21}	≈ 0.75	N/A	RKKY-Driven Reversal
-6×10^{-22}	≈ 0.55	$\downarrow 27\%$	RKKY-Driven Reversal
-5×10^{-22}	≈ 0.70	$\downarrow 7\%$	RKKY-Driven Reversal
-3×10^{-22}	≈ 0.60	$\downarrow 20\%$	Optimal RKKY-Driven Reversal
-2×10^{-22}	≈ 1.20	$\uparrow 60\%$	RKKY-Driven Reversal
-1.8×10^{-22}	≈ 0.80	$\uparrow 7\%$	RKKY-Driven Reversal
-1×10^{-22}	N/A	N/A	Weak RKKY FL1 Switching
-1×10^{-23}	N/A	N/A	Weak RKKY FL1 Switching

The summary of the RKKY parameter sweep is shown in Table 6.1. In this table three distinct dynamics are identified: non-switching due to excessive coupling (Figure 6.9), RKKY-driven reversal (Figure 6.10, and uncoupled single layer switching (Figure 6.11). The RKKY strengths were chosen to show a range from rigid RKKY coupling to a strength comparable to natural anisotropy.

The optimal switching scheme seen in Figure 6.10, has a weaker RKKY compared to the benchmark at half the strength (optimal RKKY $= -5 \times 10^{-22}$ J/link). This has the effect of a very short incubation time, the switching time is reduced to below 0.4 ns, a total switching time competitive with DRAM.

Conversely, in weak RKKY interactions, the STT is able to overcome the energy barrier ($\boldsymbol{H}_{\text{eff}}$) but if the RKKY is too weak, this leads to delayed switching, or

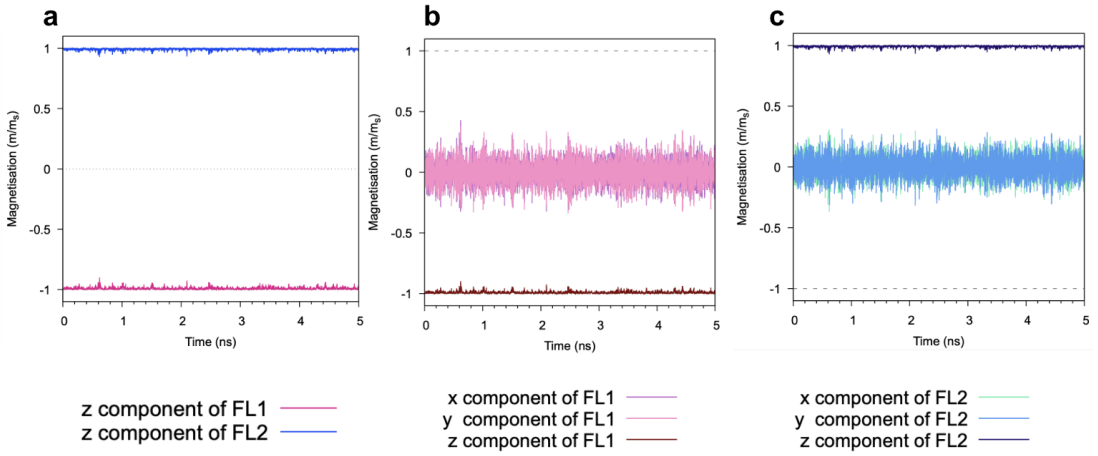


Figure 6.9: STT in FL1 is $1.0T$, STT in FL2 is $0.0T$, the RKKY coupling is -1×10^{-20}, stronger than the benchmark simulation by a factor of 10. This has the effect of increasing the energy barrier such that 1 T is insufficient to switch the system.

in very weak cases (1×10^{-23} J/link), the top layer does not switch at all. Yosida *et al.* found that while the RKKY increases the energy barrier (15) improving thermal stability Δ which is important for reliable operation at elevated temperatures. In these simulations, the drawback of increased thermal stability is a larger incubation time or a higher critical field, which can render the MRAM unsuitable for commercial applications.

In Figure 6.9, the RKKY is -1×10^{-20} J/link, stronger than the benchmark which has a RKKY of -1×10^{-21} J/link. This increase in RKKY increases the energy barrier such that $B_{\mathrm{STT}} = 1$ Tesla is not able to overcome it and lead to the MRAM switching.

In Figure 6.11, the simulated SAF MRAM stack displays switching in FL1, however, the RKKY coupling between the FL1 and FL2 layers is not sufficient to drive switching in FL2. While the z component in FL2 has a small deviation from its initial position it does not switch entirely and returns to its initial position.

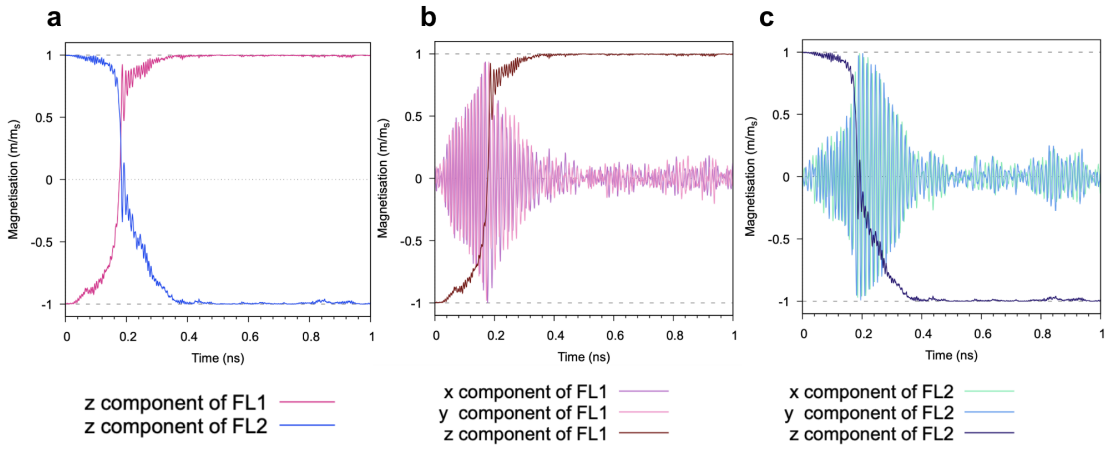


Figure 6.10: Switching where STT in FL1 is $1.0T$, STT in FL2 is $0.0T$, the RKKY coupling is -5×10^{-22} J/link, weaker than the benchmark simulation by half.

Under optimal RKKY coupling, such as those investigated in Figure 6.10, the RKKY coupling facilitates the switching, balancing the energy barrier and not preventing switching, leading to a lower switching time = 0.4 ns.

Therefore, the RKKY interaction plays two roles; it increases the energy barrier, improving thermal stability, and facilitates the switching of the second layer once the energy barrier is overcome. However, the drawback of increased thermal stability is a larger incubation time, or a higher critical field, which may make a particular MRAM configuration unsuitable for commercial applications.

6.3.3 STT polarisation in Free layer 2

In standard VAMPIRE simulations, the spin diffusion length (λ_{SD}) is assumed to be zero. However, this assumption is inaccurate when λ_{SD} is similar to the layer thickness, as is the case for CoFeB ($\lambda_{\mathrm{SD}} \approx 1.3$ nm). When $\lambda_{\mathrm{SD}} \approx d$, where d is the thickness of the layer, the assumption $\lambda_{\mathrm{SD}} = 0$ fails to capture non-local spin injection and ignores the spin relaxation that occurs in the bulk of the material. This spin relaxation is captured in Figure 6.13, where the average spin current is

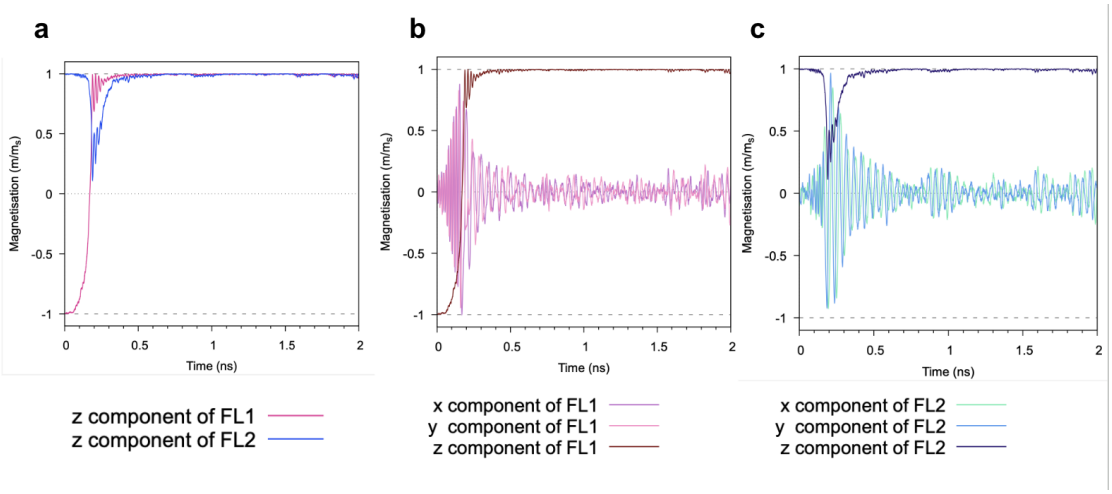


Figure 6.11: Non-Switching where the STT in FL1 is $1.0T$, STT in FL2 is $0.0T$, the RKKY coupling is -1×10^{-22} J/link. This RKKY coupling is weaker than the benchmark simulation (-1×10^{-21} J/link).

found at varying spin diffusion lengths.

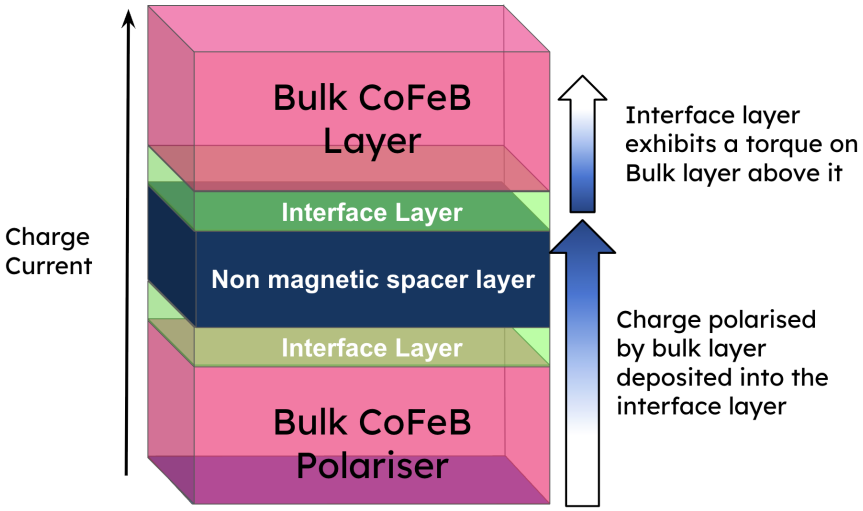


Figure 6.12: Diagram of how the bulk CoFeB layer coming from the current direction acts as a polariser which deposits a percentage of the polarisation onto the interface layer above the non-magnetic spacer layer. This occurs in the MRAM device around both MgO and Ru non-magnetic layers.

Solving the spin drift-diffusion equation with the LLG equation is prohibitively

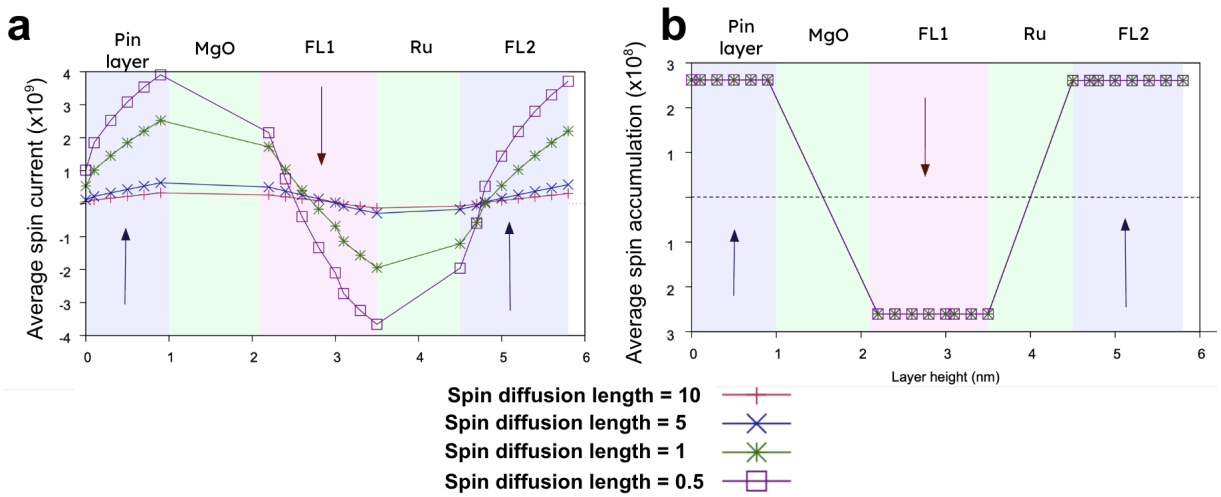


Figure 6.13: Graph of (a) average spin current against layer height, and (b) average spin accumulation against layer height. The parameters of this MRAM have been determined by spin transport

computationally expensive. Therefore, this thesis uses a simplified, phenomenological approach. Spin transport is modelled by using the bulk CoFeB layer beneath as a spin polariser ($\boldsymbol{P}$), which deposits a fraction of the spin current onto the adjacent interface layer (Figure 6.12). This parameter can be precisely tuned within the simulation. This model is verified by comparing predicted torques to spin accumulation calculated from micromagnetic models.

This simplified model is used to investigate switching dynamics, particularly the effect of a highly polarised middle layer (e.g., 100% spin polarisation). With a high polarisation, the top layer initially switches fast, but once the middle layer switches past the midway point, the large polarisation torque can overcome the RKKY interaction, forcing the top layer to return to its starting position instead of maintaining an antiparallel state.

Figure 6.13 shows the spatial dependence of the spin current (Figure 6.13(a)), and spin accumulation varying against the MRAM height. Both graphs compare

varying spin diffusion lengths effect on spin accumulation and spin current when there is insufficient current injection to drive reversal. These graphs show the origin of the polarisation assumption used in the VAMPIRE atomistic simulations.

Effect on Switching Dynamics

This section investigates the percentage deposition of increasing spin polarisation into free layer 2 from 20% to 100% and its effects on switching time. The results show a trade-off between switching speed and the coherence of the SAF structure.

Table 6.2: Table of polarisation strength deposited into FL2, the switching time, the deviation from the benchmark simulation, and the qualitative dynamic.

Polarisation (%)	t_{switch}	**% change from Baseline**	**Dynamic**
0	≈ 0.75	N/A	RKKY-Driven Reversal
20	≈ 0.55	$\downarrow 27\%$	STT assisted switching
50	≈ 0.40	$\downarrow 47\%$	STT assisted (optimised) switching
80	≈ 1.3	$\uparrow 73\%$	Dynamic Instability
100	≈ 0.45	N/A	Stable Spin Torque Oscillator

Table 6.2 shows the different simulated polarisation strengths deposited into FL2, the effect on switching time, and their qualitative difference how the MRAM switches. RKKY driven reversal has no associated polarisation deposited such that the switching in the top layer is driven entirely by RKKY interaction within the SAF structure in the MRAM. STT assisted switching has a lowered switching time, whereas dynamic instability shows a increased switching time from increased polarisation deposited. This increase in switching is driven by oscillations driven in the middle and top layer, which under a further increase in polarisation deposited in the top layer leads to the MRAM not switching at all.

At low spin polarisation being deposited into FL2 (= 20%, Figure 6.14), the supplementary STT assists the RKKY driven reversal. This decreases the over-

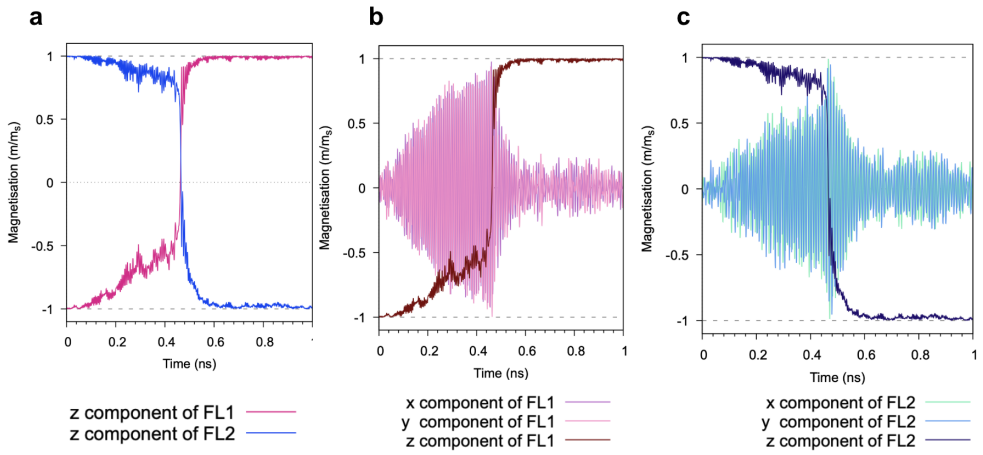


Figure 6.14: Switching of middle and top layer with top layer of anisotropy of 5×10^{-24}, RKKY of 1×10^{-21} J/link, and 20% polarisation being injected into the top layer. (a) is the z components of the bulk SAF layers, (b) has the x, y and z components of Free layer 1 and (c) has the x, y, and z components of Free layer 2. This leads to the switching being driven by both the polarisation current from bulk middle layer, and the rotation of the middle layer with the antiparallel coupling.

all switching time, where in the benchmark simulation the switching time was ($\approx 0.75ns$) compared to 20% STT-2 of ($\approx 0.55ns$). Compared to the benchmark simulation the dynamics seen in FL1 and FL2 are largely similar, with coherent switching and oscillations in the x and y direction that increases until switching occurs.

When the polarisation into FL2 reaches 50% the optimal switching parameters are reached, where switching time is minimised ($0.45ns$). Compared to the benchmark, there is a 47% reduction in switching speed. While FL2 in Figure 6.15, the x and y component continues to oscillate after the z component switches past the z = 0 point, leading to a slight delay in switching compared to the z component in FL1. The STT deposited into FL2 assists the switching without inducing instabilities which slow down or prevent switching.

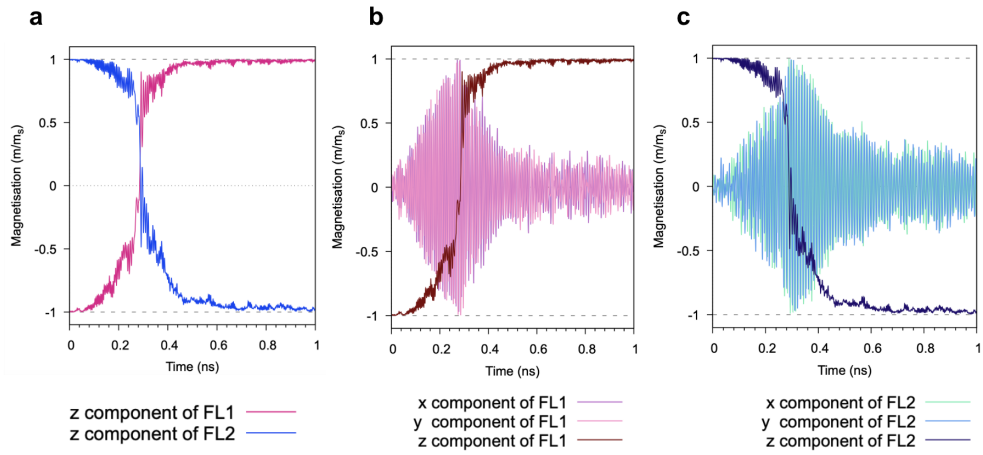


Figure 6.15: Switching of middle and top layer with top layer of anisotropy of 5×10^{-24}, RKKY of 1×10^{-21} J/link, and 50% polarisation being injected into the top layer. (a) is the z components of the bulk SAF layers, (b) has the x, y and z components of Free layer 1 and (c) has the x, y, and z components of Free layer 2. Compared to Figure 6.14 the switching time is faster, with only the polarisation being changed.

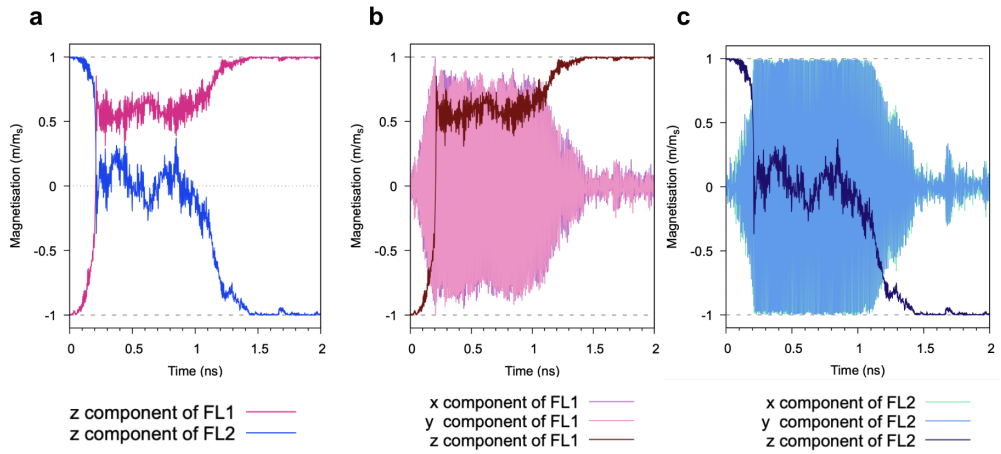


Figure 6.16: Switching of middle and top layer with top layer of anisotropy of 5×10^{-24}, RKKY of 1×10^{-21} J/link, and 50% polarisation being injected into the top layer. (a) is the z components of the bulk SAF layers, (b) has the x, y and z components of Free layer 1 and (c) has the x, y, and z components of Free layer 2.

At high spin polarisation ($>$ 80%) the dynamics shift into an undesirable regime. The spin polarisation creates a dynamic conflict where the STT torque

switching the FL2 and the RKKY torque maintaining the antiparallel coupling balance the damping torque.Figure 6.16 compared to the benchmark simulation in Figure 6.3, the transverse oscillations have become dominant preventing switching until 1.4 ns have passed. This dynamic instability prevents switching and transfers the MRAM into an oscillatory regime. When the polarisation is 80% the switching occurs (1.3ns).

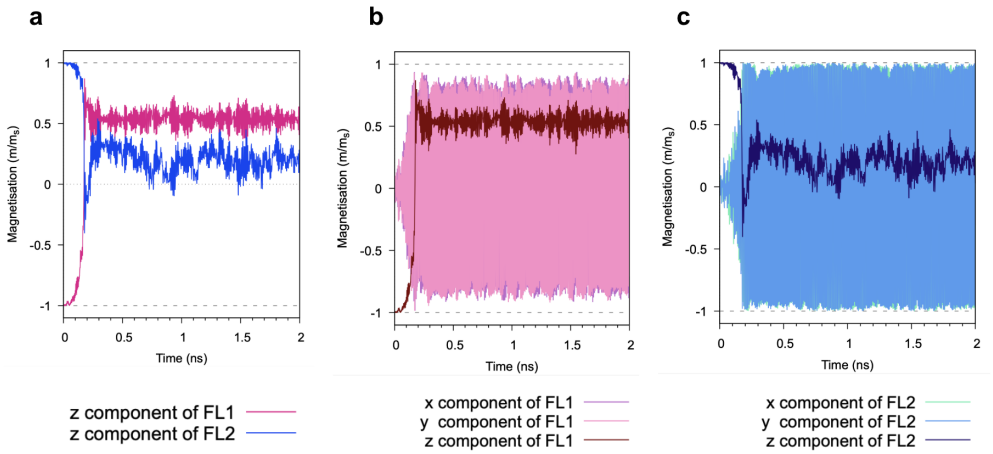


Figure 6.17: Spin torque oscillator scheme where the STT deposited in FL2 is 100% of the STT FL1, leading to no switching occurring and out-of plane rotation ($\neq \boldsymbol{m}_x, \boldsymbol{m}_y$), such that both layers have a slight positive m_z component.

At higher spin polarisation, 100%, this scheme effectively acts as a spin torque oscillator without switching at all seen in Figure 6.17, where the SAF layer precesses in the x and y axis without achieving the reversed state. Therefore, these high polarisations being deposited in FL2 are unsuitable for memory applications. Though, there are applications in replacing microwave generating radio-controlled oscillators in wireless transceivers, offering a smaller device with higher tuneability (106) (107).

7 Device Scale Synthetic Antiferromagnetic MRAM Simulations

The minimum working example (MWE) in the previous section describes the fundamental dynamics of a SAF free-layer MRAM system under STT injection, outlining the RKKY driven reversal in FL1 and FL2. When the system increases in size to a high-density MRAM cell, known as a thin-film dot, the dynamics become more complicated. Specifically, the shape anisotropy arising from the long dot width and magnetisation reversal via nucleation significantly affecting switching time and reliability. As shown in Figure 7.1, the MRAM stack contains the same layers as in the small system outlined in Chapter 6: the bottom pinned layer, the MgO layer, FL1, the Ruthenium layer, and FL2. However, in the device scale MRAM the lateral dimensions are larger. This chapter isolates these factors in a parameter sweep and analyses their individual contributions.

7.1 Nucleation and Switching

In large-scale MRAM systems, this magnetisation reversal is non-uniform. The non-uniform switching occurs through nucleation rather than the coherent rotation observed in the MWE. In MRAM dots, the energy barrier is not overcome uniformly as the edges of the dot have the strongest demagnetisation field ($\boldsymbol{H}_{\mathrm{d}}$)

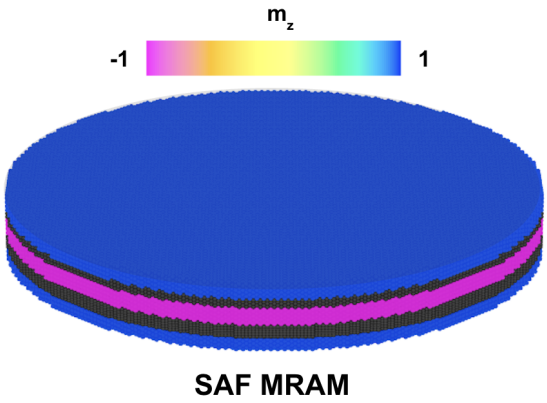


Figure 7.1: Diagram of a SAF MRAM stack from bottom to top CoFeB/MgO/CoFeB/Ru/CoFeB, where the free layer 1 is in pink, the pinned layer and free layer 2 is in blue, and the non-magnetic MgO and Ruthenium is in grey. The dimensions are 40 x 40 x 6 nm disc.

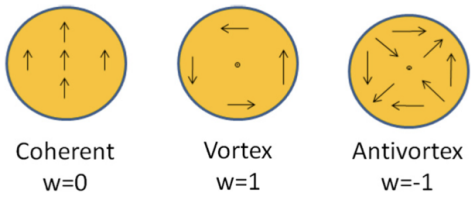


Figure 7.2: Lowest three normal modes of MRAM switching in a cylinder, labelled by winding number. From Visscher *et al.* (9)

(108), leading to local misalignments or "soft spots" in the total effective field. Local misalignments do not drive the switching alone; unless a critical radius is reached by the soft spots (r_c) such that the local moments to overcome the energy barrier, the local moments return to their original position. The time taken when the system waits for a small local reversal is known as the incubation time, which is driven by thermal fluctuations at the soft spot. This is illustrated in Figure 7.3 demonstrating the nucleation of local switching within FL1 and FL2 which then propagates in a vortex in an anticlockwise direction, which is also described by Visscher *et al* in the central diagram in Figure 7.2. While coherent switching

(w=0) was the mode of switching in the small-scale system, in this device-scale SAF MRAM vortex propagation (w=1) is the observed mode of switching within simulations.

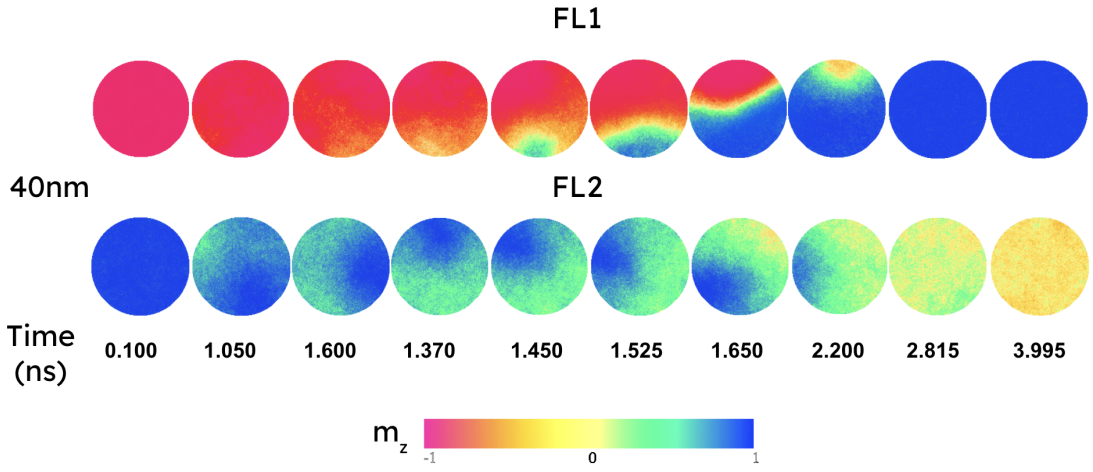


Figure 7.3: Example of nucleation on a disc shaped MRAM at 0 K, where the local change occurs on the edge of FL1 before reaching a size where it can propagate in a vortex in the x-y plane around the MRAM device and inducing switching in FL2 under weak RKKY.

For the soft spot to cause reversal it must overcome two competing energy contributions, the exchange energy cost and the external energy field. The exchange energy creates the domain wall boundary between the switched section and the surrounding unswitched regions, this domain wall costs exchange energy and favours a small reversed region. The external energy field has energy gained by aligning with the applied STT field, this term favours a large area of reversal. The critical radius represents the point where the energy barrier is maximised, such that when the radius grows beyond it the energy gains from the external field is larger than the energy cost from the domain wall and the reversed area grows rapidly.

When modelling the nucleation time LLG is used, where the total switching time (τ_{sw}) is made up from the incubation time (τ_{inc}) and the domain wall propagation time (τ_{prop}). Nucleation governs the incubation time, fast nucleation allows for a faster overall switching time. Domain wall motion governs the propagation time.

$$\tau_{sw} = \tau_{inc} + \tau_{prop} \tag{7.1}$$

The incubation time, the time before switching starts, can be modelled as the probability of a thermal event providing enough energy to overcome the reduced energy barrier. This is described by the Arrhenius-Néel law when used in conjunction with the Sharrock equation (109; 110):

$$\tau_{pulse} = \tau_0 e^{\left(\frac{\Delta E}{k_B T}\left(1-\frac{H_{app}}{H_{c0}}\right)\right)} \tag{7.2}$$

where τ_0 is the attempt frequency, ΔE is the zero-field energy barrier, H_{c0} is the deterministic switching field at 0 K, and H_{app} is the applied field from the STT. As the applied field is constant, τ_{inc} becomes the average lifetime of the stable unswitched state under the constant driving force of the applied field.

7.2 Top Layer Anisotropy

The introduction of perpendicular magnetic anisotropy (PMA) in FL2 is used to compete with the dot's inherent shape anisotropy. PMA is physically induced by capping layers such as Cobalt-Platinum (CoPt), MgO, or Tantalum, which promote electronic hybridisation at the interface (111).

Finding the optimal PMA strength for FL2 is crucial to overcoming shape anisotropy. If shape anisotropy dominates, the magnetic moment in FL2 relaxes

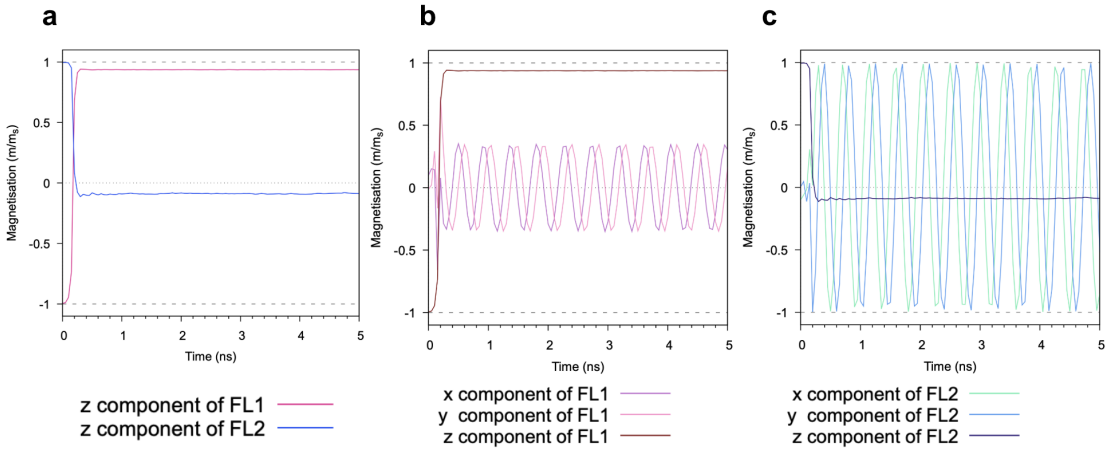


Figure 7.4: MRAM relaxing with 1 T applied STT field, 0 top layer anisotropy, RKKY coupling strength of -1×10^{-22} J/link where the z magnetisation component of FL2 relaxes towards zero, while the x and y component oscillates.

into the $x - y$ plane, seen in Figure 7.4, making the MRAM volatile as it cannot retain information while unpowered. Conversely, if the PMA is too strong, the energy barrier increases raising the critical writing field.

Specific cap layer materials are used for their interfacial properties. An MgO interface can induce high anisotropy due to the Fe-O hybridisation at the interface. Capping FL2 with MgO ensures that FL1 and FL2 have similar properties, creating a highly symmetric SAF layer, though this additional interface increases the Gilbert damping and is difficult to fabricate. Alternatively, CoPt is frequently used due to its high intrinsic magnetocrystalline anisotropy (112). This high PMA is highly tunable by Co and Pt mix, which changes the saturation magnetisation and the anisotropy constant. Therefore, simulations in this chapter vary the FL2 anisotropy to find the optimal parameters for non-volatility.

In the oscillatory regime, where shape anisotropy overcomes the PMA, or in schemes where the thermal fluctuations degrade the anisotropy in FL2, the MRAMs become spin torque nano-oscillators (STNO). In Figure 7.5 (b), demon-

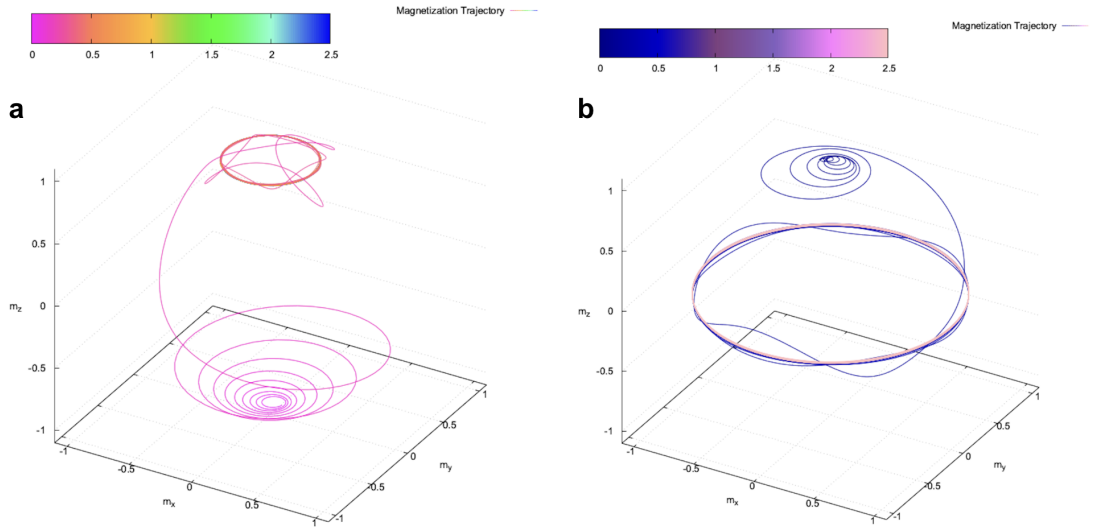


Figure 7.5: Diagram of the movement of the magnetic moment of the SAF MRAM relaxing with 1 T applied STT field, 0 top layer anisotropy, RKKY coupling strength of -1×10^{-22} J/link where the m_z of FL2 relaxes towards $m_z = 0$, while the x and y component of FL2 oscillates. This shows (a) the FL1 magnetic moment movement and (b) the FL2 magnetic moment oscillating in the x and y plane.

strates the oscillation of FL2 in the x-y direction around $m_z = 0$ while Figure 7.5 (a) oscillates FL1 in the x-y direction after near total switching. This occurs in this system as the RKKY coupling strength (-1×10^{-22} J/link) and the anisotropy applied to the top layer are not sufficient to overcome the shape anisotropy and drive total switching in FL2. While undesirable for MRAM applications, the high-frequency oscillations creates the opportunity to develop small scale, high-frequency, and low-powered ($0.2 - 0.8$T) (113) devices used in 5G telecommunications (114).

7.3 Thermal effects

This section investigates the effect of finite temperature on SAF MRAM switching, sweeping from $10K$ to $\approx 500K$. The analysis focuses on the effect of the stochastic

switching time on the incubation period and overall switching time. While 500 K is well below the previously calculated Curie temperature, investigations by Meo *et al.* into CoFeB/MgO/CoFeB MRAM show that thermal fluctuations reduce the measured saturation magnetisation in hysteresis loops, resulting in a lower measured current and a reduction in coercivity, as seen in Figure 7.6.

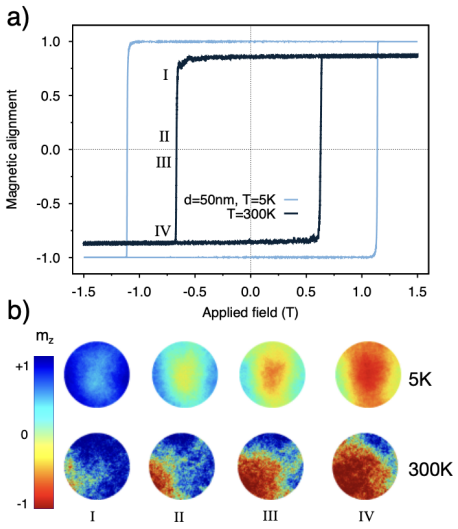


Figure 7.6: A simulated easy-axis hysteresis loop by Andrea Meo (10) for 1 nm thick 50 nm diameter nanodot at temperatures 5 K and 300 K, showing a reduction in coercivity at 300 K compared to 5 K

This reduction in coercivity creates a potential upper operating temperature limit, below the Curie temperature, where the thermal fluctuations make the memory reading process unreliable.

7.3.1 Thermal Nucleation and Stochastic Limits

The magnetisation reversal at nanoscale is thermally nucleated and incoherent at typical device operating temperatures ($\approx$ 300 K). Thermal energy allows lower energy pathways for switching, favouring nucleation and propagation rather than high-energy coherent reversal. This key difference in reversal mechanism provides

a potential solution to reducing the critical current at room temperatures. Due to this effect, comparable MRAM systems without a synthetic antiferromagnetic free layer show a strong reduction in coercivity, decreasing by up to 45% from 5 K to 300 K, as seen in Figure 7.6.

This random switching leads to an intrinsic thermal switching field distribution (TSFD), which is noticeable on sub-nanosecond time scale, even in the absence of material defects, or parameter variations. This provides a fundamental limitation that controls how accurately the magnetisation reversal can be managed and therefore an intrinsic limitation to reliability in nanoscale MRAM devices (10).

7.3.2 Simulation Results

The magnetisation dynamics of the SAF MRAM dot under an applied STT field of 1 T, shown in Figure 7.7, displays highly asymmetric switching. FL1 reverses rapidly, with an incubation time of 0.3 ns. Conversely, FL2 magnetisation initially decreases towards $m_z = 0$ but exhibits a significant delay, requiring ≈ 2 ns for full reversal. This significant delay and the stalling observed near the x - y plane, Figure7.7 (c), is due to a combination of insufficient PMA in FL2 and the weak RKKY coupling strength of -1×10^{-22} J/link. This weak coupling is unable to overcome the shape anisotropy near the switching barrier.

Further investigation into thermal stability shows that increasing the temperature from 0 K (Figure 7.7) to 300 K (Figure 7.8), causes the SAF MRAM to transition from a switching state into a spin-torque oscillator. This is because magnetic anisotropy decreases with increasing temperature (115), allowing the precessional component of the dynamics to dominate. The stable oscillation observed at $300K$, with a frequency of approximately 17 GHz, renders the devices investigated in this parameter space thermally unstable and unsuitable for memory

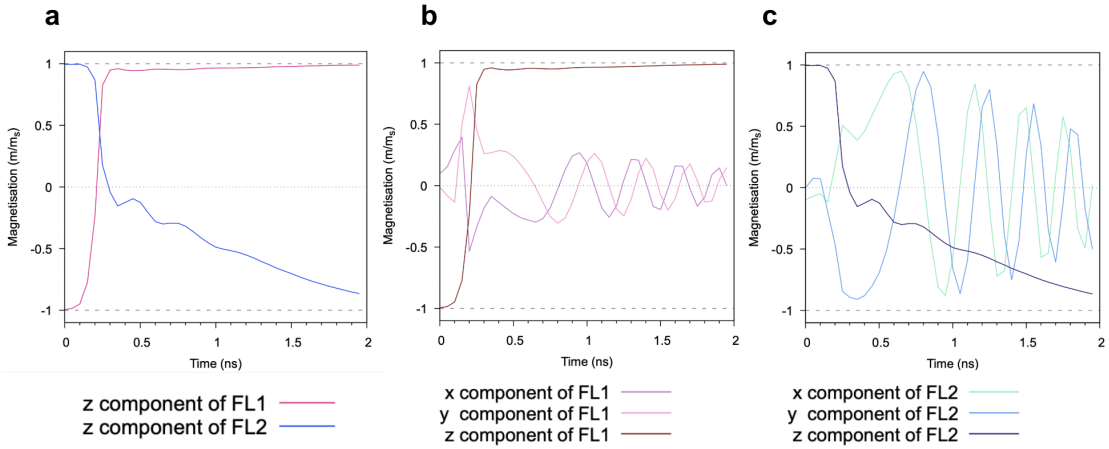


Figure 7.7: SAF MRAM dot switching with FL2 anisotropy of 5×10^{-24}, RKKY coupling strength of -1×10^{-22} J/link, 1 T of applied STT field, and 0% of the polarised field deposited in FL2. (a) has the z components of FL1 and FL2, (b) and (c) has the x, y,and z components of FL1 and FL2 respectively.

applications at room temperature.

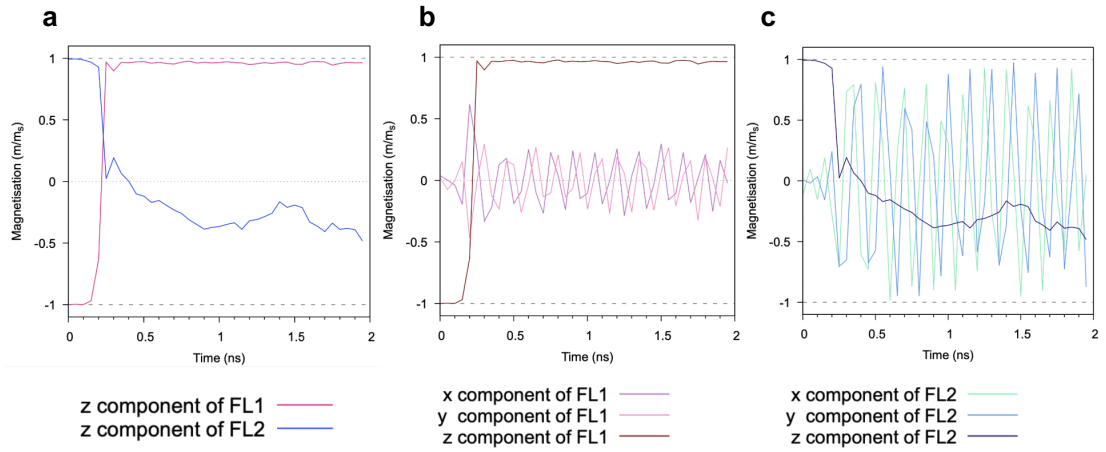


Figure 7.8: SAF MRAM in the Spin Torque Oscillation scheme at 300 K, with FL2 anisotropy of 5×10^{-24} J/link, RKKY coupling strength of -1×10^{-22}, 1 T of applied STT field, and 0% of the polarised field deposited in FL2. (a) has the z components of FL1 and FL2, (b) and (c) has the x, y,and z components of FL1 and FL2 respectively. The top layer oscillates with a frequency of ≈ 17 GHz

8 Conclusion

The primary objective of this thesis was to investigate STT MRAM with a SAF free layer to address the demand for high-performance, high-efficiency, non-volatile memory capable of surpassing conventional DRAM. The structure was modelled using the atomistic simulation package VAMPIRE.

The atomistic approach was necessary because the continuum assumption in the micromagnetic model fails to accurately capture the dynamics of the nanoscale MRAM system, specifically non-uniform thermal nucleation and the high thermal stability required for nanoscale MRAM systems.

This closing chapter will outline the main findings and their implications, highlight significant results, and detail potential future work required to gain a deeper insight into SAF MRAM dynamics and identify potential paths for further SAF MRAM optimisation.

8.1 Development of Code

The primary methodological contribution of this thesis is a Python code developed to generate the novel SAF MRAM structure and corresponding input files for atomistic simulations in VAMPIRE.

This code accurately mapped the complex multilayer CoFeB/MgO/CoFeB/Ru/CoFeB structure onto a crystal lattice. By constructing the system monolayer by mono-

layer, the code ensured perfect epitaxial alignment, allowing the simulation parameters to model a theoretically ideal system devoid of structure or interfacial defects.

The use of this code allowed the generation of physically accurate, highly parametrised, and tunable SAF geometries for subsequent simulations.

8.2 Dynamics of MWE MRAM

Chapter 6 used a minimal working example of an SAF-MRAM stack to investigate the properties of CoFeB/MgO/CoFeB/Ru/CoFeB. Using input parameters from previous studies (1), the critical field, RKKY strength, and polarisation deposited into FL2, were systematically varied .

Simulation results characterised a parameter space where the switching speed has a non-linear relationship with RKKY strength, and polarisation deposited in FL2. Increasing the critical field in 0.05 Tesla increments from 0.8 Tesla (where the MRAM did not switch), demonstrated the minimum required switching field as 0.95 Tesla. A significant reduction in incubation time was observed above 1.6 Tesla, but this "overclocking" effect was accompanied by dynamic instabilities, resulting in a larger total switching time.

The RKKY coupling strengths above 1×10^{-20} created an energy barrier that prevented switching at an applied field of 1.0 Tesla. Conversely, RKKY coupling below 1×10^{-22} was insufficient to induce switching in FL2, causing FL1 and FL2 to align in parallel instead of undergoing coherent switching.

The optimal operating window for polarisation deposited in FL2 was between 20% and 50%, with the best performance found at 50%. Notably, polarisation exceeding 80% introduced system instabilities, which either prolonged switching times or prevented switching entirely by inducing a spin torque oscillator dynamic

scheme.

8.3 Dynamics of Disc MRAM

In chapter 7 we used a device-sized SAF MRAM disc ($40 \times 40 \times 6$ nm) to find the influence of thermal effects and anisotropy on FL2, using the same parameters as the MWE. Limited investigation into the disc parameter space was conducted due to time constraints.

At 0 K, the MRAM cell was functional, exhibiting a switching time of ≈ 2 ns using parameters of 5.0×10^{-24} for anisotropy, RKKY strength of -1×10^{-21}, 1 Tesla applied STT field, and 0% polarisation deposited into FL2. However, increasing the temperature to 300 K reduced the magnetic anisotropy due to thermal fluctuations, causing the shape anisotropy to become dominant. This led to the MRAM transitioning into an oscillatory regime at a frequency of approximately 17 GHz. While this oscillatory regime is undesirable for memory applications, it highlights the potential of this structure for use in spin-transfer torque nano oscillators for applications such as 5G and microwave generation.

8.4 Summary of Conclusions and Future Work

This thesis established the core dynamics in the minimum working example and more complex dynamics within the MRAM dot. Based on these findings, the following further possible investigations are warranted:

1. **Full Spin Transport Modelling:** Future studies should replace the phenomenological STT term and the polarisation deposited in FL2, used in this study, with a full spin transport model. This will capture more accurate MRAM dynamics by precisely modelling the generation of STT at the inter-

faces.

2. **Further Disc Simulations:** Additional simulations investigating the performance of the SAF MRAM disc with larger anisotropy in FL2 to overcome the shape anisotropy and find a reasonable switching space for devices.

3. **Varying SAF Free Layer Height:** Varying the height of the SAF Free layers, which causes the resulting structure to transition from an antiferromagnet to ferrimagnet, should be investigated This has the potential to uncover new optimised switching pathways or a lower critical switching current.

4. **Detailed RKKY Coupling Analysis:** Further investigation of RKKY coupling should observe its effect into the bulk material, going beyond the interface layer and the nearest neighbours to include the next nearest neighbours. This will provide a clearer understanding of the long-range nature of the interaction. The investigation should systematically investigate the thermal stability and critical field to gain a more accurate insight into SAF-MRAM dynamics.

This continued line of research has potential to create high-performance MRAM cell and to drastically improve the performance, efficiency and economics of future computing.

Appendices

A

Appendix

A.1 Python Script: stack_generator.py

The primary Python script used to define the atomistic crystal structure, assign material parameters, and calculate the nearest neighbours for the VAMPIRE input files is provided below. This script handles the epitaxial stacking and the parameter mapping required for the layered SAF structure.

Listing A.1: Python Script for VAMPIRE Stack Generation - this generates the input file, the material file, and the .ucf file which describes the position of each individual atom. A VESTA file is also generated for easy visualisation and checking the structure before simulations are run

```
import math
import numpy as np
from itertools import product
import matplotlib.pyplot as plt

# global variables defined
atoms = []
FeCoBpin=[]
cell_size = 3.5

class Atom:
```

```
12      def __init__(self, element, x, y, z, dx, dy, dz, atom_type, id
            , parity, mat_id, c_constant=0):
13          self.element = element
14          self.position = np.array([x, y, z])
15          self.dx = dx
16          self.dy = dy
17          self.dz = dz
18          self.atom_type = atom_type
19          self.id = id
20          self.parity = parity
21          self.mat_id = mat_id
22          self.c_constant = c_constant
23
24      def distance_to(self, other_atom):
25          return np.linalg.norm(self.position - other_atom.position)
26
27      def __repr__(self):
28          return f"Atom(ID={self.id}, element={self.element}, pos={
                self.position}, type={self.atom_type})"
29
30  class InteractionMatrix:
31      def __init__(self, num_materials):
32          self.distance_matrix = np.full((num_materials,
                num_materials), np.inf)  # start with large distances
33          self.strength_matrix = np.zeros((num_materials,
                num_materials))  # int. strengths default to 0
34
35      def set_interaction(self, i, j, rij, Jx, Jy, Jz):
36          #  shortest distance and strongest Jij for the pair
37          if rij < self.distance_matrix[i][j]:
38              self.distance_matrix[i][j] = rij
```

```
39              self.distance_matrix[j][i] = rij
40              self.strength_matrix[i][j] = [Jx, Jy, Jz]
41              self.strength_matrix[j][i] = [Jx, Jy, Jz]
42
43  def in_unit_cell_skinny(atom):
44      return 0<= atom.position[0] <= 0.9 and 0<= atom.position[1] <=
            0.9
45
46  def assign_material_properties(layer_details, layer_properties):
47      for layer in layer_details:
48          prop = next((p for p in layer_properties if p["name"] ==
                layer["name"]), None)
49          if prop:
50              layer.update(prop)
51
52  def generate_layer_atom_mapping(atoms, list_layers):
53      layer_atom_mapping = {}  # maps atom_IDs to layer names --
            used later
54      vamp_mat_id_to_layer = {layer.vamp_mat_id: layer.name for
            layer in list_layers}
55
56      for atom in atoms:
57          # match atom's mat_id with layer's vamp_mat_id for vesta
                and input files
58          layer_name = vamp_mat_id_to_layer.get(atom.mat_id, None)
59          if layer_name:
60              layer_atom_mapping[atom.id] = layer_name
61          else:
62              print(f"Atom␣id␣{atom.id}␣has␣mat_id␣{atom.mat_id}␣
                    with␣no␣corresponding␣layer.")
63
```

```
64      return layer_atom_mapping
65
66  def rkky_interaction(distance, J0=7.735e-21, kF=2.0,
        decay_exponent=3):
67
68      interaction = J0 * math.cos(2 * math.pi * kF * distance) / (
            distance**decay_exponent)
69
70      return interaction
71
72
73  def calculate_interaction_matrix(list_layers):
74      # populate the interaction matrix with zeros
75      interaction_matrix = [[0.0 for _ in range(len(list_layers))]
            for _ in range(len(list_layers))]
76      distance_5_7 = distance_matrix[5][7]
77      if distance_5_7 == float('inf') :
78          RKKY = 0
79      else:
80          RKKY = rkky_interaction(distance_5_7)
81      for i, layer1 in enumerate(list_layers):
82          for j, layer2 in enumerate(list_layers):
83              # restrict interactions to adjacent layers or specific
                    RKKY interaction - so the NN calc is correct.
84              if abs(i - j) > 1 and not (
85                  (layer1.name == "CoFe_interface_feco_Ro" and
                        layer2.name == "CoFe_interface_Ro_CoFeB")
86                  or (layer1.name == "CoFe_interface_Ro_CoFeB" and
                        layer2.name == "CoFe_interface_feco_Ro")
87              ):
88                  continue  # skiping non-adjacent layers, except
```

```
            for RKKY interaction, therefore only nn
            interactions done
89
90          name1, name2 = layer1.name, layer2.name
91
92          # defining interaction rules
93          if "MgO" in (name1, name2) or "Ru" in (name1, name2):
94              interaction_matrix[i][j] = [0.0, 0.0, 0.0]
95          elif "interface_CoPt_CoFe" in name1 or "
            interface_CoPt_CoFe" in name2:
96              interaction_matrix[i][j] = [1.547e-20, 1.547e-20,
                1.547e-20]
97          elif "CoPt" in name1 or "CoPt" in name2:
98              interaction_matrix[i][j] = [4.88e-21, 4.88e
                -21,4.88e-21]
99          elif (name1 == "CoFe_interface_feco_Ro" and name2 == "
            CoFe_interface_Ro_CoFeB") or (
100             name1 == "CoFe_interface_Ro_CoFeB" and name2 == "
                CoFe_interface_feco_Ro"
101         ):
102             interaction_matrix[i][j] = RKKY
103         elif name1.startswith("CoFe_interface") and not name2.
            startswith("CoFe_interface") and name2.startswith("
            CoFe"):
104             interaction_matrix[i][j] = [1.547e-20, 1.547e-20,
                1.5504891e-20]
105         elif name2.startswith("CoFe_interface") and not name1.
            startswith("CoFe_interface") and name2.startswith("
            CoFe"):
106             interaction_matrix[i][j]=[1.547e-20, 1.547e-20,
                1.5504891e-20]
```

```
107             elif name1.startswith("CoFe_interface") and name2.
                    startswith("CoFe_interface"):
108                 interaction_matrix[i][j]=[0.0, 0.0, 0.0]
109             elif name1.startswith("CoFe") and name2.startswith("
                    CoFe"):
110                 interaction_matrix[i][j] = [7.735e-21,7.735e
                        -21,7.735e-21]
111             else:
112                 interaction_matrix[i][j] = [0.5, 0.5,0.5] #easy to
                        check if interaction matrix is not formed
                        correctly as no interaction should be = 0.5
113
114     return interaction_matrix
115
116 def calculate_distance_and_interaction_matrices(list_layers, atoms
        , cutoff_distance):
117     num_layers = len(list_layers)
118     distance_matrix = np.full((num_layers, num_layers), float('inf
            '))
119
120     atom_to_layer = {atom.id: atom.mat_id for atom in atoms}
121     layer_indices = {layer.vamp_mat_id: idx for idx, layer in
            enumerate(list_layers)}
122
123     for i, atom in enumerate(atoms):
124         for j, other_atom in enumerate(atoms):
125         # skip some so the i and j interaction matrix is symmetric
126             if i >= j:
127                 continue
128
129         # calculate distances
```

```
130             distance = atom.distance_to(other_atom)
131
132         # mapping mat_ids to layer indices
133             layer1_idx = layer_indices.get(atom.mat_id, None)
134             layer2_idx = layer_indices.get(other_atom.mat_id, None
                    )
135
136         # making sure both layers are good
137             if layer1_idx is not None and layer2_idx is not None:
138             # check specific RKYY interaction conditions
139                 layer1_name = list_layers[layer1_idx].name
140                 layer2_name = list_layers[layer2_idx].name
141
142                 if (
143                     (layer1_name == "CoFe_interface_feco_Ro" and
                            layer2_name == "CoFe_interface_Ro_CoFeB")
144                     or (layer1_name == "CoFe_interface_Ro_CoFeB"
                            and layer2_name == "CoFe_interface_feco_Ro"
                            )
145                 ):
146                 # add RKYY interaction at specific matrix
                        positions for atoms directly above - therefore,
                         RKKY is correct
147                     if atom.position[0] == other_atom.position[0]
                            and atom.position[1] == other_atom.position
                            [1]:
148                         if layer1_idx == 5 and layer2_idx == 7:
149                             distance_matrix[5][7] = distance
150                             distance_matrix[7][5] = distance
151                         elif layer1_idx == 7 and layer2_idx == 5:
152                             distance_matrix[5][7] = distance
```

```
153                             distance_matrix[7][5] = distance
154
155             # update the distance matrix with the minimum distance
                    (default logic)
156                 if distance <= cutoff_distance and distance <
                        distance_matrix[layer1_idx][layer2_idx]:
157                     distance_matrix[layer1_idx][layer2_idx] =
                            distance
158                     distance_matrix[layer2_idx][layer1_idx] =
                            distance
159
160     return distance_matrix
161
162 class Neighbor:
163     def __init__(self, atom, distance):
164         self.atom = atom
165         self.distance = distance
166
167 def is_in_adjacent_unit_cells(atom):
168     dx, dy, dz = atom.dx, atom.dy, atom.dz
169     return 0.0 <= dx <= 1.0 and 0.0 <= dy <= 1.0
170
171 def mirror_atoms_in_unit_cell(unit_cell_atoms):
172     mirrored_atoms = []
173     unique_id = 0
174     translations = [(dx, dy) for dx in [-1, 0, 1] for dy in [-1,
            0, 1]]
175
176     for dx, dy in translations:
177         for atom in unit_cell_atoms:
178             translated_x = atom.position[0] + dx
```

```
179             translated_y = atom.position[1] + dy
180             translated_z = atom.position[2]  # keeping zs as is
181             translated_dx = atom.dx + dx
182             translated_dy = atom.dy + dy
183             translated_dz = atom.dz
184 
185             mirrored_atoms.append(
186                 Atom(
187                     element=atom.element,
188                     x=translated_x,
189                     y=translated_y,
190                     z=translated_z,
191                     dx=translated_dx,
192                     dy=translated_dy,
193                     dz=translated_dz,
194                     atom_type=atom.atom_type,
195                     id=atom.id,
196                     parity=atom.parity,
197                     mat_id=atom.mat_id,
198                     c_constant=atom.c_constant,
199                 )
200             )
201             unique_id += 1
202     return mirrored_atoms
203 
204 
205 ## finding neighbours for the mirrored atoms,
206 def find_neighbors(mirrored_atoms, cutoff_distance):
207     nn_list = {atom.id: [] for atom in mirrored_atoms}
208 
209     for i, atom in enumerate(mirrored_atoms):
```

```
        for j, other_atom in enumerate(mirrored_atoms):
            if i != j:  # avoid self-comparison
                distance = atom.distance_to(other_atom)
                if distance <= cutoff_distance:
                    # calculate relative displacements
                    dx = round(other_atom.dx - atom.dx)
                    dy = round(other_atom.dy - atom.dy)
                    dz = round(other_atom.dz - atom.dz)
                    nn_list[atom.id].append({
                        'atom_id': other_atom.id,
                        'distance': distance,
                        'dx': dx,
                        'dy': dy,
                        'dz': dz,
                    })

    return nn_list


class atom_lis_t:
    def __init__(self, element, x, y, z, mat_id, atom_id=None):
        self.element = element
        self.x = x
        self.y = y
        self.z = z
        self.mat_id = mat_id
        self.id = atom_id

list_layers = []
class layers:
    def __init__(self, name, monolayers, atom_list, c_constant,
```

```
        vamp_mat_id):
241         self.name = name
242         self.monolayers = monolayers
243         self.atom_list = atom_list
244         self.c_constant = c_constant
245         self.vamp_mat_id = vamp_mat_id
246 
247 
248 interaction_strengths = {}
249 
250 layer_combinations = list(product(list_layers, list_layers))
251 
252 
253 size_xy = 3
254 def build_unit_cell(list_layers):
255     global atoms
256     parity = -1
257     ucatoms = []
258     making_id = 0
259     height = 0.0
260     current_height = 0.0
261     # create unit cell and build through layers and create atoms
        for the unit cell
262     for layer in list_layers:
263         numml = layer.monolayers  # number of monolayers in this
            layer
264         c = layer.c_constant  # layer c constant -- (height)
265         atom_list = layer.atom_list if isinstance(layer.atom_list,
             list) else [layer.atom_list]
266 
267         for _ in range(numml):  # loop over monolayers
```

```
268             for atom in atom_list:
269                 dx, dy = int(atom.x // cell_size), int(atom.y //
                        cell_size)
270                 newz = atom.z + current_height
271                 if parity == -1:
272                     ucatoms.append(Atom(atom.element, atom.x, atom
                            .y, newz, 0, 0, 0, atom.mat_id, making_id,
                            0, layer.vamp_mat_id, layer.c_constant))
273                 else:
274                     newx = (atom.x + 0.5) % 1  # ensure stays in
                            unit cell
275                     newy = (atom.y + 0.5) % 1
276                     ucatoms.append(Atom(atom.element, newx, newy,
                            newz, 0, 0, 0, atom.mat_id, making_id, 0,
                            layer.vamp_mat_id, layer.c_constant))
277                 making_id += 1  # inc. unique ID for each atom
278             current_height += c * 0.5  # incrs. height by half c-
                constant for monolayer
279             parity *= -1  # flip parity
280             height += c*0.5  # add total layer height
281
282     #  atoms for supercell
283     replicated_atoms = []
284     making_id = 0
285     for atom in ucatoms:
286         for ix in range(size_xy):
287             for iy in range(size_xy):
288                 newx = atom.position[0] + ix
289                 newy = atom.position[1] + iy
290                 newz = atom.position[2]
291                 newdx = int(newx//cell_size)
```

```
292                 newdy = int(newy//cell_size)
293                 replicated_atoms.append(Atom(atom.element, newx,
                        newy, newz, newdx, newdy, atom.dz, atom.
                        atom_type, making_id, atom.parity, atom.mat_id)
                        )
294                 making_id += 1  # creates a unique ID for
                        replicated atoms
295
296     #  atoms to global list
297     atoms = replicated_atoms
298
299     # debugging the atoms positions-- Print final atom positions
            and IDs
300     for a in ucatoms:
301         print(f"Atom␣ID={a.id},␣Element={a.element},␣Position={a.
                position}")
302
303     return height  # return the total height of the unit cell
304
305
306 layer_height = 1.0
307
308 feco = atom_lis_t("FeCo", 0.0,0.0,0.0,0)
309 Ru = atom_lis_t("Ru", 0.0,0.0,0.0,1)
310 MgO = [
311     atom_lis_t("Mg", 0.0, 0.0,0.0,2),
312     atom_lis_t("O", 0.5, 0.5, 0.0,3),
313 ]
314 CoPt = atom_lis_t("CoPt", 0.0,0.0,0.0,5)
315
316
```

```
317 #layers made of :layer name, number of monolayers, material
        defined ^, unit cell height (relative), layer no
318 list_layers.append(layers("CoFe_pin", 5, feco, 1,0))
319 list_layers.append(layers("CoFe_interface_cofe_MgO", 1, feco,
        1.1,1))
320 list_layers.append(layers("MgO", 5 , MgO, 1.2,2))
321 list_layers.append(layers("CoFe_interface_MgO_CoFe", 1, feco
        ,1.1,3))
322 list_layers.append(layers("CoFe_Ref", 6, feco, 1,4))
323 list_layers.append(layers("CoFe_interface_feco_Ro", 1, feco,1.1,5)
        )
324 list_layers.append(layers("Ru", 3, Ru, 1.2,6))
325 list_layers.append(layers("CoFe_interface_Ro_CoFeB",1, feco,
        1.1,7))
326 list_layers.append(layers("CoFe_Free",7, feco, 1,8))
327
328 height = build_unit_cell(list_layers)
329
330 unit_cell_atoms = [atom for atom in atoms if 0 <= atom.position[0]
        < 0.9
331                                                 and 0 <= atom.
                                                        position[1] < 0.9
332                                                 and 0 <= atom.
                                                        position[2]]
333
334 # find neighbors
335 height = build_unit_cell(list_layers)
336 mirrored_atoms = mirror_atoms_in_unit_cell(unit_cell_atoms)
337
338 cutoff_distance = 0.9
339 neighbors = {atom.id: [] for atom in unit_cell_atoms}
```

```
340 for atom in unit_cell_atoms:
341     for other_atom in mirrored_atoms:
342         if atom != other_atom:
343             dx = round(other_atom.dx - atom.dx)
344             dy = round(other_atom.dy - atom.dy)
345             dz = round(other_atom.dz - atom.dz)
346             distance = atom.distance_to(other_atom)
347             if distance < cutoff_distance:
348                 neighbors[atom.id].append({
349                     'atom_id': other_atom.id,
350                     'distance': distance,
351                         'atom_id': other_atom.id,
352                         'distance': distance,
353                         'dx': dx,
354                         'dy': dy,
355                         'dz': dz,
356                 })
357 
358 
359 print("\n")
360 mirrored_atoms = mirror_atoms_in_unit_cell(atoms)
361 atom_position_list = [atom for atom in mirrored_atoms if atom in
       unit_cell_atoms]
362 
363 normalised_z = []
364 min_z = min(atom.position[2] for atom in unit_cell_atoms)
365 max_z = max(atom.position[2] for atom in unit_cell_atoms)
366 normalized_z_list = [
367     (atom.position[2] - min_z) / (height) if max_z > min_z else
          0.0
368     for atom in unit_cell_atoms
```

```
]
print(min_z, max_z, height)
normalized_z_list = []

for atom in mirrored_atoms:
    if atom.id in neighbors and len(neighbors[atom.id]) == 0:
        print(f"Warning: Atom ID {atom.id} has no neighbors.")

cutoff_distance = 0.9
nn_list = find_neighbors(mirrored_atoms, cutoff_distance)

## calculate distance and interaction matrices
## used list_layers, atoms and cutoff dist so only NN//RKKY calculated
distance_matrix = calculate_distance_and_interaction_matrices(
    list_layers, atoms, cutoff_distance
)

interaction_matrix = calculate_interaction_matrix(list_layers)
for i in range(len(distance_matrix)):
    for j in range(len(distance_matrix[i])):
        if distance_matrix[i][j] == float('inf'):
            distance_matrix[i][j] = 0.0

# print matrices for debugging
print("Distance Matrix:")
for row in distance_matrix:
    print(" ".join(f"{value:6.2f}" if value != float('inf') else "   inf" for value in row))

print("Interaction Matrix:")
```

```
398 for row in interaction_matrix:
399     print("␣".join(
400     f"{value:6.2f}" if isinstance(value, (float, int)) and value
        != float('inf')
401     else "␣␣␣inf" if value == float('inf')
402     else str(value)  # convert lists to strings
403     for value in row
404 ))
405
406 for atom in atoms:
407     if atom.id not in neighbors:
408         print(f"Warning:␣Atom␣ID␣{atom.id}␣has␣no␣neighbors.")
409         continue
410
411     for neighbor in neighbors[atom.id]:
412         neighbor_id = neighbor['atom_id']
413         distance = neighbor['distance']
414         dx = other_atom.dx
415         dy = other_atom.dy
416         # additional processing here
417
418 ## making the z normalised for .ucf file xx ##
419 if max_z > min_z:  # avoid errors from division by zero
420     normalized_z_list = [(atom.position[2] - min_z) / (height -
        min_z) for atom in atoms]
421 else:
422     print("Error:␣All␣z-values␣are␣identical.␣Normalization␣
        skipped.")
423     normalized_z_list = [0.0] * len(atoms)
424 filtered_normalized_z_list = [
425     (atom.position[2] - min_z) / (height - min_z)
```

```
426     for atom in atom_position_list
427 ]
428 # define cutoff distance and call the function - less than 1 as
        the cutoff dist id % of unit cell, 1.0 or more will take into
        nnn not just nn
429 cutoff_distance = 0.9
430
431
432
433 # print out atoms and their neighbors!!!##
434 for atom in atoms:
435     print(f"Atom␣ID␣{atom.id}:␣{atom.element}␣at␣{atom.position}")
436     if atom.id in neighbors:
437         print(f"Neighbors:␣{[neighbor['atom_id']␣for␣neighbor␣in␣
                neighbors[atom.id]]}")
438     else:
439         print("No␣neighbors␣found.")
440
441
442 # Debugging: After creating and mirroring atoms
443 print(f"Before␣mirroring:␣{len(atoms)}␣atoms")
444
445 print(f"After␣mirroring:␣{len(mirrored_atoms)}␣atoms")
446 layer_atom_mapping = generate_layer_atom_mapping(atoms,
        list_layers)
447
448 # print the mapping for debugging
449 for atom_id, layer_name in layer_atom_mapping.items():
450     print(f"Atom␣ID␣{atom.mat_id}␣belongs␣to␣layer␣{layer_name}")
451 # print positions of a few mirrored atoms to ensure correct
        placement
```

```
452 for i in range(len(unit_cell_atoms)):  # print first 10 mirrored
    atom positions for inspection
453     print(f"Translated␣Atom␣ID:␣{atoms[i].id},␣Position:␣{atoms[i
        ].position}")
454
455 # ensure list_layers has been initialized
456 print(len(list_layers))
457 normalized_z_per_layer = []
458 for vamp_mat_id in sorted(set(atom.mat_id for atom in
    unit_cell_atoms)):
459
460     layer_atoms = [atom for atom in unit_cell_atoms if atom.mat_id
        == vamp_mat_id]
461
462     if not layer_atoms:  # skip empty layers
463         continue
464
465     layer_min_z = min(atom.position[2] for atom in layer_atoms)
466     layer_max_z = max(atom.position[2] for atom in layer_atoms)
467
468     # normalize z values for this layer
469     normalized_layer_min_z = (layer_min_z - min_z) / height
470     normalized_layer_max_z = (layer_max_z - min_z) / height
471
472     normalized_z_per_layer.append((vamp_mat_id,
        normalized_layer_min_z, normalized_layer_max_z))
473
474 written_interactions = set()
475 interaction_count = 0
476 for atom in unit_cell_atoms:
477     for neighbor in neighbors[atom.id]:
```

```
478         neighbor_id = neighbor['atom_id']
479         dx = neighbor['dx']
480         dy = neighbor['dy']
481         dz = neighbor['dz']
482         interaction_tuple = (atom.id, neighbor_id, dx, dy, dz)
483         if interaction_tuple not in written_interactions:
484             written_interactions.add(interaction_tuple)
485             interaction_count += 1
486
487 atom_ids = [atom.id for atom in mirrored_atoms]
488 neighbor_ids = list(neighbors.keys())
489
490 missing_ids = [atom_id for atom_id in atom_ids if atom_id not in
       neighbor_ids]
491 if missing_ids:
492     print(f"These␣atom␣IDs␣are␣missing␣in␣neighbors:␣{missing_ids}
          ") #makes sure the atoms have NNs.
493 else:
494     print("All␣atoms␣have␣neighbors.")
495
496 # write to .ucf file with absolute dx, dy, dz
497 output_ucf = "output031124.ucf"
498 # already written interactions to avoid duplicates
499 written_interactions = set()
500 cell_height = round(cell_size*height*1.05263157)
501 ##do the input so cell height (z is .1 cell_height)
502
503
504 with open(output_ucf, "w") as f:
505     f.write("#␣Unit␣Cell␣Size␣\n")
506     f.write(f"{cell_size}␣\t␣{cell_size}␣\t␣{cell_height}\n␣#unit␣
```

```
        cell␣vectors␣\n␣1.0␣\t␣0.0␣\t␣0.0␣\n␣0.0␣\t␣1.0␣\t␣0.0␣\n␣
        0.0␣\t␣0.0␣\t␣1.0␣\n")
507     f.write("␣#Atoms␣num,␣id,␣cx,␣cy,␣cz,␣mat,␣lc,␣hc␣␣\n")
508     f.write(f"{len(unit_cell_atoms)}␣\n")
509     i = 0
510     for atom in unit_cell_atoms:
511         normed_z = atom.position[2]/(height)
512         f.write(f"{(i)}␣\t␣{atom.position[0]}␣\t␣{atom.position
            [1]}␣\t␣{normed_z:.4f}␣\t␣{atom.mat_id}␣\n")
513         i += 1
514     # Write interactions using absolute dx, dy, dz values
515     f.write("#␣Interactions␣n␣exctype,␣id␣i␣j␣dx␣dy␣dz␣Jij\n")
516     interaction_id = 0
517     filtered_atoms = [atom for atom in mirrored_atoms if (-0.1 <
        atom.dx < 0.9) and (-0.1 < atom.dy < 0.9)]
518     f.write(f"{interaction_count}\t␣normalised-isotropic␣\n")
519     for atom in filtered_atoms:
520         for neighbor in neighbors[atom.id]:
521             neighbor_id = neighbor['atom_id']
522             distance = neighbor['distance']
523             dx = neighbor['dx']
524             dy = neighbor['dy']
525
526             # look up the actual neighbor atom using neighbor_id
527             neighbor_atom = next((a for a in mirrored_atoms if a.
                id == neighbor_id), None)
528
529             # write the interaction to the file - creating the ucf
                file
530             f.write(f"{interaction_id}\t{atom.mat_id}\t{
                neighbor_atom.mat_id}\t"
```

```
                    f"{dx}\t{dy}\t{atom.dz}\t1.0\n")

            interaction_id += 1


print(f"Output written to {output_ucf}")
output_mat = "d03output.mat"
with open(output_mat, "w") as file:
    file.write("
        #------------------------------------------------------ \n")
    file.write("# Generated material file for CoFeB AFM MRAM \n")
    file.write("# LA Elliot 2024/5 \n")
    file.write("
        #------------------------------------------------------\n")
    file.write("# Number of Materials \n")
    file.write("
        #------------------------------------------------------ \n")
    file.write(f"material:num-materials = {len(list_layers)} \n")

    for i, atom in enumerate(list_layers, start=1):
        name1 = atom.name
        file.write(f"
            #------------------------------------------------------\n"
            )
        file.write(f"# Material {i} {atom.name} \n")
        file.write(f"
            #------------------------------------------------------\n"
            )
        file.write(f"material[{i}]:material-name = {atom.name} \n"
            )

```

```
554         # write interactions specific to this material
555         for j, target_atom in enumerate(list_layers, start=1):
556             values = interaction_matrix[i-1][j-1]  # access list
                of values or a single value
557 
558             if isinstance(values, list):  # if it's a list,
                process each value
559                 value_str = ", ".join(f"{v:.6e}" for v in values)
                     # format all values in scientific notation
560                 has_non_zero = any(v != 0.0 for v in values)  #
                    check if any value is non-zero
561             else:  # If it's a single float
562                 value_str = f"{values:.6e}"  # format single value
                     in scientific notation
563                 has_non_zero = values != 0.0  # check if the
                    single value is non-zero
564 
565     # Only write non-zero values
566             if has_non_zero:
567                 file.write(f"material[{i}]:exchange-matrix[{j}] =
                    [{value_str}] \n")
568         if name1 == ("CoFe_Ref") or name1 == ("CoFe_Free"):
569             file.write(f"material[{i}]:uniaxial-anisotropy-
                constant = 0.0 \n")
570         if name1 == ("CoFe_Free")or name1 == ("
            CoFe_interface_Ro_CoFeB"):
571             file.write(f"material[{i}]:initial-spin-direction =
                0,0,-1 \n")
572         if name1 ==("CoFe_interface_MgO_CoFe") or name1 == ("
            CoFe_Ref") or name1 == ("CoFe_interface_cofe_MgO") or
            name1 == ("CoFe_pin") or name1 == ("
```

```
            CoFe_interface_feco_Ro"):
573             file.write(f"material[{i}]:initial-spin-direction␣=␣
                    0,0,1␣\n")
574             #specific materials need to be processed with sp.
                    values
575         file.write(f"material[{i}]:unit-cell-category␣=␣{i}␣\n")
576         if name1.startswith("CoFe_interface"):
577             file.write(f"material[{i}]:material-element␣=␣Li␣\n")
                    #interfaces are given the material Li, they are
                    given material values consistent with CoFeB, but by
                     giving them Li they show up green in VESTA, some
                    other materials end up with similar colours to Fe,
                    etc
578             file.write(f"material[{i}]:atomic-spin-moment␣=␣1.6!
                    muB␣\n")
579             file.write(f"material[{i}]:damping-constant␣=␣0.1␣\n")
580         elif "CoPt_up" in name1: #not used in this thesis due to
                time constraints :(
581             file.write(f"material[{i}:material-element␣=␣Pt\n")
582             file.write(f"material[{i}]:atomic-spin-element=␣1.0␣!
                    muB␣\n")
583             file.write(f"material[{i}]:damping-contant␣=␣1.0␣\n")
584         elif "CoPt_down" in name1:
585             file.write(f"material[{i}:material-element␣=␣Be\n")
586             file.write(f"material[{i}]:atomic-spin-element=␣1.0␣!
                    muB␣\n")
587             file.write(f"material[{i}]:damping-contant␣=␣1.0␣\n")
588         elif name1.startswith("CoFe"):
589             file.write(f"material[{i}]:material-element␣=␣Fe␣\n")
590             file.write(f"material[{i}]:atomic-spin-moment␣=␣1.6!
                    muB␣\n")
```

```
591             file.write(f"material[{i}]:damping-constant␣=␣0.1␣␣\n"
                    )
592         elif name1.startswith("MgO"):
593             file.write(f"material[{i}]:material-element␣=␣H␣\n")
594             file.write(f"material[{i}]:non-magnetic␣=␣remove␣\n")
595         else:
596             file.write(f"material[{i}]:material-element␣=␣Ru␣\n")
597             file.write(f"material[{i}]:non-magnetic␣=␣remove␣\n")
                    # Ru and MgO are non-magnetic=removed as in VAMPIRE
                     you can approximate the interactiton over the
                    distances and not need to simulate them directly
                    saving time.
598
599 #Input file generated with ::
600 output_input = "input"
601 with open(output_input, "w") as file:
602     file.write(f"#----------------------------------------␣\n#␣
            Creation␣attributes\n
            #----------------------------------------\n")
603     file.write(f"create:periodic-boundaries-x\ncreate:periodic-
            boundaries-y\ncreate:cylinder\n
            #----------------------------------------\n#␣System␣
            dimensions\n#----------------------------------------\n")
604     file.write(f"dimensions:unit-cell-size␣=␣3.54␣!A\ndimensions:
            system-size-x␣=␣40␣!nm\ndimensions:system-size-y␣=␣40␣!nm\n
            ")
605     file.write(f"dimensions:system-size-z␣=␣{cell_height/10}␣!nm␣\
            n␣") #makes sure even if you change the monolayers the
            height is correct.
606     file.write(f"create:cylinder␣\n␣#dimensions:particle-size␣=␣40
            ␣!nm␣\n")
```

```
607     file.write(f"#----------------------------------------\n# Material File\n#----------------------------------------\n\nmaterial:file = d03output.mat\nmaterial:unit-cell-file = output031124.ucf\n")
608     file.write(f"#----------------------------------------\n# Simulation attributes\n#----------------------------------------\n")
609     file.write(f"sim:minimum-temperature = 000.9\n")
610     file.write(f"sim:time-steps = 1 !fs\nsim:loop-time-steps = 100000\nsim:time-steps-increment = 100\nsim:spin-transfer-torque-polarization-unit-vector = 0,0,-1\n")
611     file.write(f"#----------------------------------------\n# Program and integrator details\n#----------------------------------------\n")
612     file.write(f"sim:program = time-series\nsim:integrator = llg-heun\n#----------------------------------------\n")
613     file.write(f"# data output\n#----------------------------------------\n")
614     file.write(f"config:atoms\nconfig:atoms-output-rate = 100\noutput:real-time")
615     file.write(f"output:material-magnetisation\nscreen:time-steps\nscreen:material-magnetisation")
616
617     # output to .xyz file - useful for visualisation and can be opened in VESTA
618 output_filename = "VESTA_file.xyz"
619 with open(output_filename, "w") as file:
620     file.write(f"{len(atoms)}\n\n")
621     for atom in mirrored_atoms:
622         file.write(f"{atom.element}\t{(atom.position[0]*cell_size):.2f}\t{(atom.position[1]*cell_size):.2f}\t{(atom.
```

```
            position[2]*cell_size):.2f}\n")
for layer in list_layers:
    print(f"Layer: {layer.name}, Vamp Mat ID: {layer.vamp_mat_id}"
        )
```

References

[1] Sutee Sampan-A-Pai, Rattaphon Phoomatna, Worawut Boonruesi, Andrea Meo, Jessada Chureemart, Richard F. L. Evans, Roy W. Chantrell, and Phanwadee Chureemart. Magnetization dynamics at finite temperature in cofeb–mgo based mtjs. *Scientific Reports*, 13(1), February 2023.

[2] R. Sbiaa, H. Meng, and S. N. Piramanayagam. Materials with perpendicular magnetic anisotropy for magnetic random access memory. *physica status solidi (RRL) – Rapid Research Letters*, 5(12):413–419, October 2011.

[3] Phanwadee Chureemart. Models of spin torque using self-consistent solutions of the magnetisation and spin accumulation. *University of York*, 2013.

[4] Evgeny Y Tsymbal and Žutić Igor. *Spintronics handbook, second edition: Spin transport and magnetism*. CRC Press, London, England, 2 edition, March 2021.

[5] Andrea Meo. *Atomistic model of magnetisation dynamics and equilibrium properties of magnetic tunnel junctions*. Phd thesis, University of York, September 2018. Available at `https://etheses.whiterose.ac.uk/id/eprint/22730/`.

[6] J. Fernandez-Roldan. *Micromagnetism of cylindrical nanowires with compositional and geometric modulations*. PhD thesis, 06 2019.

[7] Krisztián Bán, Csaba Gulyás, Gábor Remport, and Antal Lovas. The background of amorphous curie-point tailoring for temperature regulation, using glassy fe-based alloys. *Advanced Electronic Materials*.

[8] A. Jesche, R.W. McCallum, S. Thimmaiah, J.L. Jacobs, V. Taufour, A. Kreyssig, R.S. Houk, S.L. Bud'ko, and P.C. Canfield. Giant magnetic anisotropy and tunnelling of the magnetization in li2(li1-xfex)n. *Nature Communications*, 5(1), February 2014.

[9] P. B. Visscher, Kamaram Munira, and Robert J. Rosati. Instability mechanism for stt-mram switching, 2016.

[10] Andrea Meo, Phanwadee Chureemart, Shuxia Wang, Roman Chepulskyy, Dmytro Apalkov, Roy W. Chantrell, and Richard F. L. Evans. Thermally nucleated magnetic reversal in cofeb/mgo nanodots. *Scientific Reports*, 7(1), December 2017.

[11] TrendForce. [news] memory price rally may run past 2028 as samsung, sk hynix reportedly cautious on expansion. *TrendForce News*, dec 2025. Accessed: 2025-12-12.

[12] Dadmehr Rahbari and Mohsen Nickray. Task offloading in mobile fog computing by classification and regression tree. *Peer-to-Peer Networking and Applications*, 13(1):104–122, February 2019.

[13] Mark Horowitz. 1.1 computing's energy problem (and what we can do about it). In *2014 IEEE International Solid-State Circuits Conference Digest of Technical Papers (ISSCC)*. IEEE, February 2014.

[14] Hyunsung Jung, Yoon Jong Song, Seungpil Ko, Jeong-Heon Park, and Su Jin Ahn. Overview of reliability in scaling embedded stt-mram. In *2025 IEEE International Reliability Physics Symposium (IRPS)*, page 01–06. IEEE, March 2025.

[15] Chikako Yoshida, Takashi Takenaga, Yoshihisa Iba, Yuichi Yamazaki, Hideki Noshiro, Koji Tsunoda, Akiyoshi Hatada, Masaaki Nakabayashi, Atsushi Takahashi, Masaki Aoki, and Toshihiro Sugii. Enhanced thermal stability in perpendicular top-pinned magnetic tunnel junction with synthetic antiferromagnetic free layers. *IEEE Transactions on Magnetics*, 49(7):4363–4366, July 2013.

[16] Meiyin Yang, Yan Cui, Jingsheng Chen, and Jun Luo. Materials, processes, devices and applications of magnetoresistive random access memory. *International Journal of Extreme Manufacturing*, 7(1):012010, November 2024.

[17] Xing Huang. Experimental research on the South-Pointing loadstone spoon (¡italic¿Sinan¡/italic¿)[1]. *Chinese Annals of History of Science and Technology*, 3(1):21–43, June 2019.

[18] Peter J Mohr, David B Newell, Barry N Taylor, and Eite Tiesinga. CODATA recommended values of the fundamental physical constants: 2022. *Rev. Mod. Phys.*, 97(2), April 2025.

[19] C. T. Chen, Y. U. Idzerda, H.-J. Lin, N. V. Smith, G. Meigs, E. Chaban, G. H. Ho, E. Pellegrin, and F. Sette. Experimental confirmation of the x-ray magnetic circular dichroism sum rules for iron and cobalt. *Physical Review Letters*, 75(1):152–155, July 1995.

[20] P. A. M. Dirac. The quantum theory of the electron. *Proceedings of the Royal Society of London. Series A, Containing Papers of a Mathematical and Physical Character*, 117:610–624, 1928.

[21] P Kusch and H M Foley. The magnetic moment of the electron. *Phys. Rev.*, 74(3):250–263, August 1948.

[22] Toichiro Kinoshita. The fine structure constant. *Reports on Progress in Physics*, 59(11):1459–1492, November 1996.

[23] W Heisenberg. Mehrkrperproblem und resonanz in der quantenmechanik. *Eur. Phys. J. A*, 38(6-7):411–426, June 1926.

[24] W Heisenberg. Zur theorie des ferromagnetismus. *Eur. Phys. J. A*, 49(9-10):619–636, September 1928.

[25] H Kliem, M Kuehn, and B Martin. The weiss field revisited. *Ferroelectrics*, 400(1):41–51, September 2010.

[26] M A Ruderman and C Kittel. Indirect exchange coupling of nuclear magnetic moments by conduction electrons. *Phys. Rev.*, 96(1):99–102, October 1954.

[27] Tadao Kasuya. A theory of metallic ferro- and antiferromagnetism on zener's model. *Prog. Theor. Phys.*, 16(1):45–57, July 1956.

[28] Kei Yosida. Magnetic properties of cu-mn alloys. *Phys. Rev.*, 106(5):893–898, June 1957.

[29] P Bruno and C Chappert. Oscillatory coupling between ferromagnetic layers separated by a nonmagnetic metal spacer. *Phys. Rev. Lett.*, 67(12):1602–1605, September 1991.

[30] S S Parkin, N More, and K P Roche. Oscillations in exchange coupling and magnetoresistance in metallic superlattice structures: Co/Ru, Co/Cr, and Fe/Cr. *Phys. Rev. Lett.*, 64(19):2304–2307, May 1990.

[31] M N Baibich, J M Broto, A Fert, Nguyen Van Dau F, F Petroff, P Etienne, G Creuzet, A Friederich, and J Chazelas. Giant magnetoresistance of (001)Fe/(001)Cr magnetic superlattices. *Phys. Rev. Lett.*, 61(21):2472–2475, November 1988.

[32] G Binasch, P Grünberg, F Saurenbach, and W Zinn. Enhanced magnetoresistance in layered magnetic structures with antiferromagnetic interlayer exchange. *Phys. Rev. B Condens. Matter*, 39(7):4828–4830, March 1989.

[33] N F Mott. The resistance of liquid metals. *Proc. R. Soc. Lond. A Math. Phys. Sci.*, 146(857):465–472, September 1934.

[34] T Valet and A Fert. Theory of the perpendicular magnetoresistance in magnetic multilayers. *Phys. Rev. B Condens. Matter*, 48(10):7099–7113, September 1993.

[35] M. Julliere. Tunneling between ferromagnetic films. *Physics Letters A*, 54(3):225, September 1975.

[36] N F Mott. Electrons in transition metals. *Adv. Phys.*, 13(51):325–422, July 1964.

[37] van Son PC, van Kempen H, and P Wyder. Boundary resistance of the ferromagnetic-nonferromagnetic metal interface. *Phys. Rev. Lett.*, 58(21):2271–2273, May 1987.

[38] M Johnson and R H Silsbee. Interfacial charge-spin coupling: Injection and detection of spin magnetization in metals. *Phys. Rev. Lett.*, 55(17):1790–1793, October 1985.

[39] Saburo Takahashi and Sadamichi Maekawa. Spin current, spin accumulation and spin hall effect. *Sci. Technol. Adv. Mater.*, 9(1):014105, January 2008.

[40] Selman Hershfield and Hui Lin Zhao. Charge and spin transport through a metallic ferromagnetic-paramagnetic-ferromagnetic junction. *Phys. Rev. B Condens. Matter*, 56(6):3296–3305, August 1997.

[41] M Johnson and R H Silsbee. Ferromagnet-nonferromagnet interface resistance. *Phys. Rev. Lett.*, 60(4):377, January 1988.

[42] M Johnson and R H Silsbee. Coupling of electronic charge and spin at a ferromagnetic-paramagnetic metal interface. *Phys. Rev. B Condens. Matter*, 37(10):5312–5325, April 1988.

[43] H J V Tyrrell. The origin and present status of fick's diffusion law. *J. Chem. Educ.*, 41(7):397, July 1964.

[44] R J Elliott. Theory of the effect of spin-orbit coupling on magnetic resonance in some semiconductors. *Phys. Rev.*, 96(2):266–279, October 1954.

[45] MI Dyakonov and VI Perel. Spin relaxation of conduction electrons in noncentrosymmetric semiconductors. *Soviet Physics Solid State, Ussr*, 13(12):3023–3026, 1972.

[46] Abhijeet Ranjan, Chun-Liang Yang, Chia-Chang Lee, Rudis Ismael Salinas Padilla, and Chih-Huang Lai. Spin–orbit torque driven perpendicular magnetization switching in Re/CoFeB/MgO with high thermal stability. *APL Mater.*, 10(1):011104, January 2022.

[47] E I Rashba. Spin dynamics and spin transport. *J. Supercond.*, 18(2):137–144, April 2005.

[48] A Manchon, H C Koo, J Nitta, S M Frolov, and R A Duine. New perspectives for rashba spin-orbit coupling. *Nat. Mater.*, 14(9):871–882, September 2015.

[49] A Brataas, Y V Nazarov, and G E Bauer. Finite-element theory of transport in ferromagnet-normal metal systems. *Phys. Rev. Lett.*, 84(11):2481–2484, March 2000.

[50] A Brataas, Y Tserkovnyak, G E W Bauer, and P J Kelly. Spin pumping and spin transfer. In *Spin Current*, pages 87–135. Oxford University Press, July 2012.

[51] W H Butler, X-G Zhang, T C Schulthess, and J M MacLaren. Spin-dependent tunneling conductance ofFe—MgO—Fesandwiches. *Phys. Rev. B Condens. Matter*, 63(5), January 2001.

[52] T Miyazaki and N Tezuka. Giant magnetic tunneling effect in Fe/Al2O3/Fe junction. *J. Magn. Magn. Mater.*, 139(3):L231–L234, January 1995.

[53] J Mathon and A Umerski. Theory of tunneling magnetoresistance of an epitaxial Fe/MgO/Fe(001) junction. *Phys. Rev. B Condens. Matter*, 63(22), May 2001.

[54] Shinji Yuasa, Taro Nagahama, Akio Fukushima, Yoshishige Suzuki, and Koji Ando. Giant room-temperature magnetoresistance in single-crystal Fe/MgO/Fe magnetic tunnel junctions. *Nat. Mater.*, 3(12):868–871, December 2004.

[55] Stuart S P Parkin, Christian Kaiser, Alex Panchula, Philip M Rice, Brian Hughes, Mahesh Samant, and See-Hun Yang. Giant tunnelling magnetoresistance at room temperature with MgO (100) tunnel barriers. *Nat. Mater.*, 3(12):862–867, December 2004.

[56] L Berger. Emission of spin waves by a magnetic multilayer traversed by a current. *Phys. Rev. B Condens. Matter*, 54(13):9353–9358, October 1996.

[57] J C Slonczewski. Current-driven excitation of magnetic multilayers. *J. Magn. Magn. Mater.*, 159(1-2):L1–L7, June 1996.

[58] T L Gilbert. Classics in magnetics a phenomenological theory of damping in ferromagnetic materials. *IEEE Trans. Magn.*, 40(6):3443–3449, November 2004.

[59] Peter M Levy and Shufeng Zhang. Resistivity due to domain wall scattering. *Phys. Rev. Lett.*, 79(25):5110–5113, December 1997.

[60] J Z Sun. Spin-current interaction with a monodomain magnetic body: A model study. *Phys. Rev. B Condens. Matter*, 62(1):570–578, July 2000.

[61] Ernst Ising. Beitrag zur theorie des ferromagnetismus. *Zeitschrift für Physik*, 31(1):253–258, February 1925.

[62] S. Blundell. *Magnetism in Condensed Matter*. Oxford Master Series in Condensed Matter Physics. OUP Oxford, 2001.

[63] R F L Evans, W J Fan, P Chureemart, T A Ostler, M O A Ellis, and R W Chantrell. Atomistic spin model simulations of magnetic nanomaterials. *Journal of Physics: Condensed Matter*, 26(10):103202, February 2014.

[64] A.I. Liechtenstein, M.I. Katsnelson, V.P. Antropov, and V.A. Gubanov. Local spin density functional approach to the theory of exchange interactions in ferromagnetic metals and alloys. *Journal of Magnetism and Magnetic Materials*, 67(1):65–74, May 1987.

[65] G. Kotliar, S. Y. Savrasov, K. Haule, V. S. Oudovenko, O. Parcollet, and C. A. Marianetti. Electronic structure calculations with dynamical mean-field theory. *Reviews of Modern Physics*, 78(3):865–951, August 2006.

[66] David L. Price and Kurt Skold. *1. Introduction to Neutron Scattering*, page 1–97. Elsevier, 1986.

[67] D. C. Jiles. *Introduction to Magnetism and Magnetic Materials*. Chapman Hall, London [or New York], 1st edition, 1991.

[68] Risi Guo, Xiulan Xu, Yan Ma, Gang Han, Lihua Wang, Jiao Teng, and Guanghua Yu. Study of the relationship between magnetic anisotropy and composition ratio of fe oxide to fe at cofeb/mgo film interface. *Applied Surface Science*, 585:152697, May 2022.

[69] Patrick Bruno. Tight-binding approach to the orbital magnetic moment and magnetocrystalline anisotropy of transition-metal monolayers. *Physical Review B*, 39(1):865–868, January 1989.

[70] S. Ikeda, J. Hayakawa, Y. Ashizawa, Y. M. Lee, K. Miura, H. Hasegawa, M. Tsunoda, F. Matsukura, and H. Ohno. Tunnel magnetoresistance of 604 *Applied Physics Letters*, 93(8), August 2008.

[71] G J Bowden, G B G Stenning, and G van der Laan. Inter and intra macrocell model for point dipole–dipole energy calculations. *Journal of Physics: Condensed Matter*, 28(6):066001, January 2016.

[72] N Metropolis and S Ulam. The monte carlo method. *J. Am. Stat. Assoc.*, 44(247):335–341, September 1949.

[73] Charles J. Geyer. Practical markov chain monte carlo. *Statistical Science*, 7(4):473–483, 1992.

[74] Christophe Andrieu and Éric Moulines. On the ergodicity properties of some adaptive mcmc algorithms. *The Annals of Applied Probability*, 16(3), August 2006.

[75] Achille Thin, Nikita Kotelevskii, Christophe Andrieu, Alain Durmus, Eric Moulines, and Maxim Panov. Nonreversible mcmc from conditional invertible transforms: a complete recipe with convergence guarantees, 2020.

[76] Nicholas Metropolis, Arianna W. Rosenbluth, Marshall N. Rosenbluth, Augusta H. Teller, and Edward Teller. Equation of state calculations by fast computing machines. *The Journal of Chemical Physics*, 21(6):1087–1092, June 1953.

[77] W K Hastings. Monte carlo sampling methods using markov chains and their applications. *Biometrika*, 57(1):97, April 1970.

[78] G. T. Barkema and M. E. J. Newman. New monte carlo algorithms for classical spin systems, January 1999.

[79] Ulli Wolff. Collective monte carlo updating for spin systems. *Physical Review Letters*, 62(4):361–364, January 1989.

[80] D. C. Rapaport. Book review: A guide to monte carlo simulations in statistical physics. d. p. landau and k. binder, cambridge university press, 2000, pp. 384+xiii. *Journal of Statistical Physics*, 103(5–6):1143–1145, June 2001.

[81] D. Hinzke and U. Nowak. Magnetization switching in a heisenberg model for small ferromagnetic particles. *Physical Review B*, 58(1):265–272, July 1998.

[82] J D Alzate-Cardona, D Sabogal-Suárez, R F L Evans, and E Restrepo-Parra. Optimal phase space sampling for monte carlo simulations of heisenberg spin systems. *Journal of Physics: Condensed Matter*, 31(9):095802, January 2019.

[83] W Brown. Thermal fluctuation of fine ferromagnetic particles. *IEEE Trans. Magn.*, 15(5):1196–1208, September 1979.

[84] Julien Tranchida, Pascal Thibaudeau, and Stam Nicolis. Colored-noise magnetization dynamics: From weakly to strongly correlated noise. *IEEE Transactions on Magnetics*, 52(7):1–4, July 2016.

[85] M. d'Aquino, C. Serpico, G. Coppola, I. D. Mayergoyz, and G. Bertotti. Midpoint numerical technique for stochastic landau-lifshitz-gilbert dynamics. *Journal of Applied Physics*, 99(8), April 2006.

[86] Sabpreet Bhatti, Rachid Sbiaa, Atsufumi Hirohata, Hideo Ohno, Shunsuke Fukami, and S.N. Piramanayagam. Spintronics based random access memory: a review. *Materials Today*, 20(9):530–548, November 2017.

[87] M. Bendra, W. Goes, S. Selberherr, and V. Sverdlov. Simulation of saf-enhanced multilayered stt-mram structures. *Microelectronic Engineering*, 302:112426, January 2026.

[88] Atsufumi Hirohata, Keisuke Yamada, Yoshinobu Nakatani, Ioan-Lucian Prejbeanu, Bernard Diény, Philipp Pirro, and Burkard Hillebrands. Review on spintronics: Principles and device applications. *Journal of Magnetism and Magnetic Materials*, 509:166711, September 2020.

[89] S. S. P. Parkin. Systematic variation of the strength and oscillation period of indirect magnetic exchange coupling through the 3d, 4d, and 5dtransition metals. *Physical Review Letters*, 67(25):3598–3601, December 1991.

[90] L. Tillie, B. Dieny, R. C. Sousa, J. Chatterjee, S. Auffret, N. Lamard, J. Guelffucci, E. Nowak, and I.L. Prejbeanu. P-stt-mram thermal stability and modeling of its temperature dependence. In *2018 International Symposium on VLSI Technology, Systems and Application (VLSI-TSA)*, page 1–2. IEEE, April 2018.

[91] Takashi Takeuchi, Koji Tsunekawa, Young-Suk Choi, Yoshinori Nagamine, David D Djayaprawira, Akira Genseki, Yoichi Hoshi, and Yoshitaka Kitamoto. Crystallization of amorphous CoFeB ferromagnetic layers in CoFeB/MgO/CoFeB magnetic tunnel junctions. *Jpn. J. Appl. Phys. (2008)*, 46(25):L623–L626, June 2007.

[92] Jun-Su Kim, Gukcheon Kim, Jinwon Jung, Kuyoul Jung, Jaehun Cho, Woo-Yeong Kim, and Chun-Yeol You. Control of crystallization and magnetic properties of CoFeB by boron concentration. *Sci. Rep.*, 12(1):4549, March 2022.

[93] James Lourembam, Khoong Hong Khoo, Jinjun Qiu, Huiqing Xie, Seng Kai Wong, Qi Jia Yap, and Sze Ter Lim. Tuning damping and magnetic anisotropy in ultrathin boron-engineered mgo/co–fe–b/mgo heterostructures. *Advanced Electronic Materials*, 7(9), July 2021.

[94] Yaroslav Tserkovnyak, Arne Brataas, and Gerrit E. W. Bauer. Enhanced gilbert damping in thin ferromagnetic films. *Physical Review Letters*, 88(11), February 2002.

[95] K. Pasanai and P. Pairor. Spin-flip scattering and dimensional effect on transport of charge and spin across metal/ferromagnet material interfaces. *Physical Review B*, 84(22), December 2011.

[96] Kaihua Lou, Tunan Xie, Qianwen Zhao, Baiqing Jiang, ChaoChao Xia, Hanying Zhang, Zhihong Yao, and Chong Bi. Perpendicular magnetic anisotropy in as-deposited cofeb/mgo thin films. *Applied Physics Letters*, 121(12), September 2022.

[97] Jeongmin Hong, Ali Hadjikhani, Mark Stone, Frances I. Allen, Vladimir Safonov, Ping Liang, Jeffrey Bokor, and Sakhrat Khizroev. The physics of spin-transfer torque switching in magnetic tunneling junctions in sub-10 nm size range. *IEEE Transactions on Magnetics*, 52(7):1–4, July 2016.

[98] S. Yuasa, A. Fukushima, K. Yakushiji, T. Nozaki, M. Konoto, H. Maehara, H. Kubota, T. Taniguchi, H. Arai, H. Imamura, K. Ando, Y. Shiota, F. Bonell, Y. Suzuki, N. Shimomura, E. Kitagawa, J. Ito, S. Fujita, K. Abe, K. Nomura, H. Noguchi, and H. Yoda. Future prospects of mram technologies. In *2013 IEEE International Electron Devices Meeting*, pages 3.1.1–3.1.4. IEEE, December 2013.

[99] Yanru Li, Bowen Shen, Meiyin Yang, Guoqiang Yu, Baoshan Cui, Peiyue Yu, Shuaiyu Gong, Jianfeng Gao, Jinbiao Liu, and Jun Luo. Field-free magnetization switching of synthetic antiferromagnets magnetic tunnel junction

induced by spatially gradient spin texture. *Applied Physics Letters*, 127(18), November 2025.

[100] Zhendong Zhu, Bingcheng Zhao, Weihua Zhu, Minghong Tang, Yang Ren, Q. Y. Jin, and Zongzhi Zhang. Annealing effect and interlayer modulation on magnetic damping of cofeb/interlayer/pt thin films. *Applied Physics Letters*, 113(22), November 2018.

[101] Nilamani Behera, M. Sanjoy Singh, Sujeet Chaudhary, Dinesh K. Pandya, and P. K. Muduli. Effect of ru thickness on spin pumping in ru/py bilayer. *Journal of Applied Physics*, 117(17), February 2015.

[102] A. Mouhoub, F. Millo, C. Chappert, J.-V. Kim, J. Létang, A. Solignac, and T. Devolder. Exchange energies in cofeb/ru/cofeb synthetic antiferromagnets. *Physical Review Materials*, 7(4), April 2023.

[103] Wayne Lack, Sarah Jenkins, Andrea Meo, Roy W Chantrell, Keith M McKenna, and Richard F L Evans. Thermodynamic properties and switching dynamics of perpendicular shape anisotropy mram. *Journal of Physics: Condensed Matter*, 36(14):145801, January 2024.

[104] Gustav Mörée and Mats Leijon. Review of hysteresis models for magnetic materials. *Energies*, 16(9):3908, May 2023.

[105] Jing Ju Lu, Huei Li Huang, and I. Klik. Field orientations and sweep rate effects on magnetic switching of stoner–wohlfarth particles. *Journal of Applied Physics*, 76(3):1726–1732, August 1994.

[106] I. Firastrau, L. D. Buda-Prejbeanu, B. Dieny, and U. Ebels. Spin-torque nano-oscillator based on a synthetic antiferromagnet free layer and perpendicular to plane polarizer. *Journal of Applied Physics*, 113(11), March 2013.

[107] I. Volvach, A.D. Kent, E.E. Fullerton, and V. Lomakin. Spin-transfer-torque oscillator with an antiferromagnetic exchange-coupled composite free layer. *Physical Review Applied*, 18(2), August 2022.

[108] Andreas Vogel, Sebastian Wintz, Judith Kimling, Markus Bolte, Thomas Strache, Monika Fritzsche, Mi-Young Im, Peter Fischer, Guido Meier, and Jürgen Fassbender. Domain-wall pinning and depinning at soft spots in magnetic nanowires. *IEEE Transactions on Magnetics*, 46(6):1708–1710, June 2010.

[109] M.P. Sharrock. Time-dependent magnetic phenomena and particle-size effects in recording media. *IEEE Transactions on Magnetics*, 26(1):193–197, 1990.

[110] M. Sharrock and J. McKinney. Kinetic effects in coercivity measurements. *IEEE Transactions on Magnetics*, 17(6):3020–3022, November 1981.

[111] Young-Wan Oh, Kyeong-Dong Lee, Jong-Ryul Jeong, and Byong-Guk Park. Interfacial perpendicular magnetic anisotropy in cofeb/mgo structure with various underlayers. *Journal of Applied Physics*, 115(17), February 2014.

[112] K. Barmak, J. Kim, L. H. Lewis, K. R. Coffey, M. F. Toney, A. J. Kellock, and J.-U. Thiele. On the relationship of magnetocrystalline anisotropy and stoichiometry in epitaxial l10 copt (001) and fept (001) thin films. *Journal of Applied Physics*, 98(3), August 2005.

[113]

[114] Sheng Jiang, Linrong Yao, Shun Wang, Di Wang, Long Liu, Akash Kumar, Ahmad A. Awad, Artem Litvinenko, Martina Ahlberg, Roman Khymyn, Sunjae Chung, Guozhong Xing, and Johan Åkerman. Spin-torque nano-oscillators and their applications. *Applied Physics Reviews*, 11(4), October 2024.

[115] Jan-Ulrich Thiele, Stefan Maat, and Eric E. Fullerton. Ferh/fept exchange spring films for thermally assisted magnetic recording media. *Applied Physics Letters*, 82(17):2859–2861, April 2003.